SHAPE-SELECTIVE GROWTH OF BIMETALLIC NANOSTRUCTURES

ZHANG WEIQING

(M.Sc., USTC, China)

A THESIS SUBMITTED

FOR THE DEGREE OF DOCTOR OF PHILOSOPHY

DEPARTMENT OF CHEMICAL AND BIOMOLECULAR ENGINEERING

NATIONAL UNIVERSITY OF SINGAPORE

2013

DECLARATION

I hereby declare that this thesis is my original work and it has been written by me in its entirety. I have duly acknowledged all the sources of information which have been used in the thesis.

This thesis has also not been submitted for any degree in any university previously.

23 April 2014

Acknowledgement

Firstly, I would like to express my sincere gratitude to my supervisor, Asst. Prof. Lu Xianmao, for his suggestions, invaluable guidance, patience and continuous support throughout the whole period of my PhD candidature. I would like to express my heartiest thanks and appreciation for his invaluable help and guidance given to me for writing scientific papers including this PhD thesis.

In the same, I would like to express my sincere thanks to the Department of Chemical and Biomolecular Engineering for offering me a NUS research scholarship, which helps me a lot to carry out my PhD studies without any financial burdens during my PhD candidature.

I would like to express my thanks to my lab mates Dr. Sun Zhipeng, Dr. Chen Ningping, Dr. Han Hui, Dr. Niu Wenxin, Mr. Shaik Firdoz Mr. Zhao Qipeng, Mr. Chen Shucheng for their valuable discussions and the good time we shared in the lab.

I would like to thank Mr. Chia Phai Ann, Mr. Liu Zhicheng, Mr. Mao Ning, Dr. Yuan Zeliang, Dr. Yang Liming, Mr. Tan Evan Stephen, Mr. Ang Wee Siong, Ms Li Fengmei, Ms Li Xiang, Ms LEE, Chai Keng, Mdm Fam Hwee Koong Samantha for their kind support and help during my PhD candidature.

Finally, I would like to express my deepest love to my beloved parents who have given everything to me to make my life happy and beautiful. Last

but not least, my sincere and special thanks given to my husband for his unconditional support and help during my study. It is not exaggeration to say that I could not able to complete my PhD work without their love, encouragement, and support.

Table of Contents

Summary

Noble metal nanomaterials have shown catalytic and optical properties strongly dependent on their shape and size. For bimetallic nanomaterials, these properties can be further tuned by varying their composition. Therefore, bimetallic nanostructures have become a new research focus in recent years. Shape-selective synthesis of bimetallic nanocrystals may allow scientists to achieve optimal properties for applications in diverse areas including electrochemical catalysis and sensing. For instance, platinum-based bimetallic nanostructures are promising candidates for electrochemical catalysts due to their enhanced catalytic activities. For sensing applications, particularly for techniques based on surface plasmon resonance and surface-enhanced Raman scattering (SERS), gold-silver (Au-Ag) bimetallic nanostructures are the hottest materials because of their superior plasmonic properties. To synthesize bimetallic nanostructures for various applications, control over the catalytic and optical properties via shape-selective growth is highly desirable. For instance, shape-controlled synthesis of porous and hollow Pt-based bimetallic electrocatalysts may allow enhanced electrocatalytic performance. This is because the porous and hollow structures of Pt-based catalysts exhibit large electrochemically activated surface areas. In addition, the preparation of Au-Ag bimetallic nanostructures with stable and repeatable hot spots is relatively unexplored. The hot spot, defined as a nanometer-scale distance between two metallic particles, can amplify the electromagnetic field to give highly

enhanced SERS intensity. The aims of this thesis are to investigate the synthesis of bimetallic nanostructures with controlled morphologies and to explore their applications in electrocatalysis and SERS.

To achieve these aims, we firstly tailored the galvanic replacement reaction (GRR) between Ag nanocubes (Ag NCs) and K_2PtCl_4 to form Pt/Ag porous and hollow bimetallic nanostructures. By varying the reaction kinetic factors, Pt/Ag bimetallic hollow nanostructures with controlled number of voids were prepared. In addition, by introducing additional reagents, the GRR method has been successfully extended to the preparation of complex hollow and porous nanostructures including dimers and popcorns. GRR was also employed with seed-mediated growth method to fabricate Au/Ag sandwich nanostructures with interior gaps, in which SERS probe molecules were embedded. Such sandwich nanostructures are promising SERS-active substrates. To further understand the shape-selective synthesis of Au/Ag bimetallic plasmonic nanostructures, seed-mediated growth method was also investigated to control the deposition of Ag on Au bipyramids. By tuning the reaction kinetics, Au@Ag core-shell nanorods fully terminated with {110} end facets were obtained for the first time. The above mentioned series of shape-controlled syntheses of Pt/Ag and Au/Ag bimetallic nanostructures should advance our current understanding on the growth mechanism of bimetallic nanostructures.

Nomenclature

Pt	Platinum
Au	Gold
Ag	Silver
$AgNO_3$	Silver nitrate
K_2PtCl_4	Potassium tetrachloroplatinate
$HAuCl_4 \cdot 3H_2O$	Gold(III) chloride trihydrate
$PdCl_2$	Palladium (II) chloride
CTAB	Cetyl-trimethylammonium bromide
CTAC	Cetyl-trimethylammonium chloride
PVP	Poly(vinylpyrrolidone)
DI H_2O	Deionized water
EG	Ethylene glycol
$HClO_4$	Perchloric acid
KOH	Potassium hydroxide
NaOH	Sodium hydroxide
NaCl	Sodium chloride
$Fe(NO_3)_3 \bullet 9H_2O$	Iron(III) nitrate nonahydrate
AA	L-ascorbic acid
HCl	Hydrochloride acid
4-ATP	4-Aminothiophenol
MOR	Methanol oxidation reaction
EM	Electromagnetic
ORR	Oxygen reduction reaction
EOR	Ethanol oxidation reaction
FOR	Formic acid oxidation reaction
LSPR	Localized surface plasmon resonance
SERS	Surface enhanced Raman scattering

GRR	Galvanic replacement reaction
EDX	Energy dispersive X-ray spectroscopy
FESEM	Field Emission Scanning Electron Microscopy
TEM	Transmission electron microscopy
HRTEM	High-Resolution Transmission Electron
UV-Vis	Ultraviolet-Visible
XPS	X-ray Photoelectron Spectroscopy
XRD	X-ray Diffraction
ECSAs	Electrochemically activated surface areas
BPs	Bipyramids
Fcc	Face-centered cubic crystal
Γ	Interfacial energy
FM	Frank—van der Merwe
VW	Volmer—Weber
SK	Stranski—Krastanov
M_A	Metal A
M_B	Metal B

List of Figures

List of Tables

Chapter 1. Introduction

1.1 Background

Noble metal nanocrystals exhibit unique properties, which can be utilized for different applications, such as catalysis, sensing, SERS and optoelectronics.[1-3] The physical and chemical properties of noble metal nanocrystals are strongly dependent on their size,[4-6] shape,[7-10] and composition.[11-13] For monometallic nanocrystals, size and shape control are effective strategies to tune their optical properties and catalytic activities.[14,15,16] For bimetallic noble metal nanocrystals, in addition to size and shape, composition control is another important parameter to tune their properties. Hence, bimetallic nanostructures have received tremendous attention in recent years. This is because nanocrystals composed of two metals, either in the form of homogeneous alloy or heterogeneous mixture, have shown distinct and advantageous properties compared with their monometallic counterparts.[17-19]

Controlling the shape of the metallic nanostructures has strong implication on their catalytic activities. This is because nanocrystals with different shape profiles may have different exposed facets. Since the number of neighboring atoms and dangling bonds on catalytic surface change with exposed facet, the catalytic activity of nanocrystals is highly facet-dependent. For instance, Pt nanocrystals terminated with high-index {730} facets have shown unusually high activity for electrooxidation of formic acid and ethanol.[9]

This facet-dependent effect on catalytic activity, which is also applicable to bimetallic nanostructures, is mainly caused by both the surface geometry and surface electronic structure that vary with facets. It should be noted that the catalytic activities for bimetallic surfaces of different facets might follow different order compared to that of their monometallic counterparts. For example, it has been well-established that for Pt surface, the ORR activity in perchloric acid increases following the order of Pt(100)<<Pt(111)<Pt(110). For Pt_3Ni alloy, however, it increases as $Pt_3Ni(100)<Pt_3Ni(110)<<<Pt_3Ni(111)$.[20] In addition to facet effect, lattice strain may also impact the electronic structure of the catalyst and contribute considerably on the ORR activity.[21] This can be attributed to either the compressed or stretched lattice at the crystal domain boundaries that exhibit different electronic structures. Therefore, shape-controlled synthesis of Pt-based bimetallic nanocrystals is an elegant strategy for enhancing catalytic reactivity.

Controlling the shape of metallic nanoparticles also has pivotal impact on their optical properties. For example, the LSPR properties of Au and Ag nanostructures are highly shape-dependent because highly localized charge polarizations at their corners and edges lead to unique optical scattering responses.[10,22,23] Shape-selective synthesis of bimetallic nanostructures results in different or new optical properties relative to Au or Ag component. For instance, the LSPR peaks of Au-Ag bimetallic hollow nanostructures can be readily tuned from visible to near-infrared region relative to Au or Ag

monometallic nanostructures.[24,25] In contrast to the two SPR modes typically observed for Au nanocrystals --longitudinal and transverse modes, Au@Ag bimetallic core-shell nanostructures show four plasmon peaks, which are ascribed to longitudinal, transverse, and two octupolar LSPR, respectively.[26] It is also worth noting that plasmonic focusing as a new feature has been found in Au@Ag core-shell bimetallic nanostructures.[27]

Some colloidal synthetic routes for bimetallic nanostructures have been developed based on the synthesis of monometallic nanostructures. So far, there are some important synthetic methods for synthesis of bimetallic nanostructures: (1) co-reduction, (2) seed-mediated growth, (3) galvanic replacement, (4) thermal decomposition, (5) radiolysis method, (6) sonochemical synthesis, and (7) biological method. Through these colloidal synthetic routes, bimetallic alloy, core-shell, and particle on particle nanostructures with different shapes have been obtained via controlling the thermodynamic and kinetic factors at the nucleation and growth stages.[28-30]

1.2 Problem definitions

Bimetallic nanocrystals with controlled morphologies and compositions have shown superior properties and broader applications compared to monometallic nanocrystals. In recent years, this research field has been developing rapidly and a variety of bimetallic nanocrystals with different shapes have been reported. Despite the fast progress in the shape-selective synthesis of bimetallic nanostructures, challenges still remain in the following

directions:

1. Pt-based bimetallic nanostructures can enhance electrocatalytic activities and decrease the loading of Pt. Shape-selective growth of Pt-based nanostructures is a promising direction to optimize the electrocatalytic performance of fuel cell catalysts. Recently, chemists have made great progress on controlling the shape of Pt-based bimetallic catalysts. However, only a limited number of studies were reported on shape-selective synthesis of porous and hollow Pt-based bimetallic nanostructures. It is widely accepted that porous and hollow nanostructures would give large electrochemically activated surface areas (ECSAs). Therefore, further investigation of the synthesis of Pt-based porous and hollow nanostructures is necessary.

2. An important application of Au and Ag nanomaterials is SERS. In SERS application, one of the most touted studies is to maximize the enhancement factors (EFs) of the probe molecules, which can be realized by generating the so-called “hot spots” between plasmonic particles. This is because the hot spots would produce much stronger electromagnetic field. Currently, inter-particle gaps existing among random aggregations of particles or metal-molecule-metal junctions are generally utilized as hot spots. However, inter-particle gaps as hot spots show some inevitable problems: i) EF is unreliable because the gaps are usually unstable and irreproducible; ii) EF may not be enhanced to its maximum because the particles around the hot spots

have inconsistent structure parameters. In contrast with the inter-particle gaps, gaps existing within a single particle are much more stable and repeatable. Therefore, the synthesis of Au-Ag bimetallic nanostructures with interior gaps is an attractive alternative method to achieve reliable and maximum EFs for SERS application.

3. Systematic and fundamental understanding of the growth process for bimetallic nanostructures has yet to be achieved. For monometallic nanocrystals, reasonable understanding has been gained about how various factors such as reaction kinetics, surfactants, and presence of anionic or cationic species may influence the final shape of the nanocrystals at nucleation and growth stages. The introduction of the second metal in such syntheses complicates the growth process. Both the thermodynamic and kinetic parameters identified for monometallic nanocrystals may not be applicable to bimetallic ones. All these factors need to be systematically studied in bimetallic nanocrystal systems for better understanding of their growth process.

1.3 Objectives and scope

The principal objective of this thesis is to investigate the shape-selective synthesis of bimetallic nanostructures and their applications in electrochemical catalysis and SERS. We focus on two bimetallic systems – Pt/Ag and Au/Ag. Through the study of the shape-controlled synthesis of Pt/Ag and Au/Ag bimetallic nanostructures, we hope i) to advance our current

understanding on the growth mechanism of bimetallic nanostructures; ii) to gain better control over the morphologies of bimetallic nanostructures with different growth methods including modified galvanic replacement reaction (GRR) and seeded growth; iii) to enhance the electrochemical catalytic (for Pt/Ag) and optical (for Au/Ag) properties of the resulting bimetallic nanostructures. The detailed research activities and scopes of this thesis work are as following:

- To synthesize Pt/Ag porous and hollow bimetallic nanostructures with controlled morphologies and investigate their electrochemical activities. Four different Pt/Ag bimetallic nanostructures with porous walls and hollow interiors, including hollow nanoboxes, dimers, multimers, and popcorn-shaped nanostructures, are synthesized via a tailored GRR between Ag NCs and Pt precursor. The GRR is tuned with the assistant of HCl and PVP. The roles of HCl and PVP in the formation of these Pt/Ag hollow structures are discussed. Furthermore, the electrochemical activities of these porous and hollow nanostructures towards MOR are investigated and compared with that of Pt/C commercial catalysts.

- To fabricate Au/Ag@ATP@Au/Ag sandwich structures with 4-ATP located within the interior gaps for the SERS study. Au/Ag@ATP@Au/Ag sandwich nanostructures with interior gaps are synthesized via GRR and seed-mediated growth method. Four interior gap sizes are obtained by controlling the thickness of Ag shell and the

reaction extent of GRR. 4-ATP is buried under the Ag shell first and then located in the interior gaps after GRR. The effect of the interior gaps of sandwich nanostructures on the SERS EFs is investigated. In addition, the SERS enhancement mechanism is discussed based on the experimental results.

- To synthesize Au@Ag core-shell nanorods with controlled shapes and explore important reaction factors for shape-selective synthesis of bimetallic nanostructures. Three types of Au@Ag nanorods, which are flat-tipped nanorods terminated with {110} facets, sharp-tipped nanorods bounded with {111} facets, and dumbbell-shaped nanorods, are grown via seed-mediated method through using Au BPs as seeds and tuning reaction kinetic parameters. The reaction kinetics including capping agents and pH values are manipulated for controlling the deposition of Ag on the Au BPs. The morphological evolution is monitored to study the growth mechanism. Furthermore, the possible growth mechanism is presented.

1.4 Organization of the Thesis

The thesis is composed of seven chapters. Chapter 1 introduces the general background of bimetallic nanostructures. Chapter 2 provides a literature review on the shape-controlled synthesis of bimetallic nanostructures. In Chapter 3, detailed experimental procedures and characterization techniques employed in this work are presented. Chapter 4 focuses on the

shape-controlled synthesis of Pt/Ag hollow and porous bimetallic nanostructures for the investigation of electrocatalytic activities. In Chapter 5, Au/Ag@ATP@Au/Ag sandwiched nanostructures with controlled interior gap sizes are prepared for the SERS study. Chapter 6 discusses the shape-selective synthesis of Au@Ag nanorods with tuning end facets and the proposed growth mechanism. Chapter 7 summarizes the principal findings in this thesis. Future work is also discussed.

Chapter 2. Literature Review

This chapter provides a review of the major topics relevant to the morphology control of bimetallic nanostructures. The review includes three sections. Section 2.1 introduces three basic synthetic routes of bimetallic nanostructures. In section 2.2, some principles and factors for morphology control of bimetallic nanostructures are discussed. The following two sections summarize the latest development in both shape control and applications of bimetallic nanostructures with well-defined morphologies, respectively.

2.1 Basic colloidal synthetic routes of bimetallic nanostructures

Typically, the preparation of bimetallic nanostructures with controlled shape is more complicated than monometallic ones. Although a variety of studies have been reported for the shape-selective growth of monometallic nanocrystals and reasonable understanding regarding the growth mechanisms has been obtained in recent years,[4,10] the rules that have been discovered for monometallic nanocrystals generally cannot be simply applied to bimetallic cases. This is because the involvement of the second metal in the reaction has significant effect on both the nucleation and growth stages of the nanostructures -- the reaction kinetics may be altered by introducing the precursor of the second metal to the reaction system, causing either slower or faster nucleation; the deposition mode of the second metal on the surface of the seeds will interfere with the further growth of the first metal due to the

change in surface energy and lattice strain of the nanocrystals; the interaction of surfactant with the surface of nanocrystals composed of single metal or two metals are also different due to the different binding strength of the functional groups with the two metal atoms. All the above factors will complicate the shape-controlled synthesis of bimetallic nanostructures. Over the past couple of decades, some design rules or synthetic protocols have been successfully developed for monometallic nanocrystals.[10] For bimetallic nanostructures, however, controlling their shape is still by large based on trial-and-error approaches, although a few generalized methods applicable for some particular bimetallic systems have started to emerge.[31-36]

2.1.1 Co-reduction method

To date, several synthetic methods have been developed for shape-selective growth of bimetallic nanostructures. The first method is co-reduction. This is a relatively simple method that involves the use of two metal precursors -- one for each metal, a suitable reducing agent or multiple reducing agents that may convert the metal ions into their atomic form, and surfactants that bind to the nanocrystal surface to mediate their size and shape. Depending on the reduction rate and the interaction of the two metals, either heterogeneous structures such as dendritic or smooth core-shell nanocrystals or homogeneous alloy nanocrystals may be formed. A large number of core-shell nanocrystals with a metallic core surrounded by a shell of the second metal have been synthesized *via* this approach.[37,38] The formation mechanisms of core-shell or dendritic structures in Pt-based bimetallic systems have been

discussed in details in a recent review of Yang and coworkers.[15] During the reaction, because of the different reduction rates or concentrations of the metal precursors, atoms of one metal may be generated first and nucleate to form seeds for the deposition of the second metal. Co-reduction may also lead to the formation of dendritic nanostructures. When the lattice mismatch of the two metals are large, or the sum of the surface energy of M_B and interfacial energy is larger than the surface energy of M_A, a so-called Volmer-Webber (VW) growth mode takes place, causing the formation of "islands" of M_B on the M_A nanocrystal surface. If continuous growth of M_B on the "islands" is allowed, these "islands" will eventually develop to form dendritic structure. Co-reduction method is also one of the most common approaches to prepare homogenous bimetallic alloy nanocrystals. Different morphologies of bimetallic alloys can be synthesized by this method. This can be achieved by manipulating the reaction kinetics to allow proper reduction and growth rates of the two metals. In addition, capping agents with specific facet binding properties are mainly employed to tune the shape of bimetallic alloys. Specifically, tetrahedron, octahedron, icosahedrons, cubes and rods like morphologies of bimetallic alloys are mainly synthesized by using different capping agents.

2.1.2 Galvanic replacement reaction (GRR)

GRR is a powerful method to form bimetallic hollow structures. Typically, GRR-based synthesis involves the use of metal nanostructures as sacrificial templates to react with ions of a more noble metal. Due to the difference in

electrode potentials of the two metals, the nanostructured metal templates will be dissolved and the more noble metal ions will be reduced to their elemental form, which subsequently deposits onto the surface of the templates. Depending on a number of factors such as similarity in crystal structures, degree of lattice mismatch, and difference in metallic bonding strengths, a conformal or a non-conformal growth of the second metal may take place on the surface of the template to form a shell while the first metal is continuously consumed from the core. In the end, a structure with a hollow interior and a shell composed of either just the second metal or the alloy of both metals can be formed. To date, a wide variety of bimetallic hollow nanostructures have been prepared via GRR,[14,39] Depending on the composition and reaction conditions, these nanostructures may exhibit either smooth or rough surfaces.

2.1.3 Seed-mediated growth

Seed-mediated growth is another important synthetic method for the formation of bimetallic nanostructures. This type of growth may be achieved under the following conditions: 1) the reduction potential of the second metal is more negative relative to the first metal, so the template composed of the first metal will not react with the precursor of the second metal but mainly serves as the substrate for the deposition of the second metal; or 2) even though the first metal is more reactive than the second metal, when a relatively strong reducing agent is present in the reaction, the second metal ions tend to be reduced by the reducing agent instead of the nanostructured template of the first metal. In this case, the reaction kinetics directs the reduction pathway of

the second metal so that a galvanic replacement reaction will not occur. The template of the first metal is preserved for the deposition of the second metal. The deposition of the second metal on the nanocrystal surface of the first metal follows three types of growth mode. Depending on the rate of the deposition, the amount of the precursor, the physical properties of the two metals including lattice constants and metal-metal bond strength, the growth mode of the second metal may lead to the formation of a conformal monolayer/multiple-layer coating, clustered nanoparticles that give rough and porous surfaces, or thick coating that changes the geometry of the nanocrystals.

2.1.4 Thermal decomposition of precursor metal complexes

This method is mainly used for the synthesis of small bimetallic nanostructures from organic metallic complexes.[40,41] These complexes may be a mixture of two individual monometallic complexes or a single bimetallic complex. The organic complexes are heated slowly to remove organic ligands and eventually a very small bimetallic nanostructure is produced. By using this strategy, Sun et.al have synthesized Fe-Pt nanoalloys by heating a mixture of monometallic $Pt(acac)_2$ and $Fe(Co)_5$ complexes.[42] The composition of Fe-Pt in the nanoalloy can be tuned by varying the concentration of respective precursor before thermolysis.[43] However, this method is limited by the generation of irregular nanostructures with varied nanoalloy compositions due to heterogeneous decomposition of metallic organic complexes.

2.1.5 Radiolysis method

In this method, a solution containing a mixture of two monometallic precursors along with stabilizing agent is irradiated under gamma rays. The gamma rays are absorbed by the solution and solvated electrons are generated which can act as reducing agents for the metallic ions and respective bimetallic nanostructures can be produced. The final morphology of the bimetallic nanostructures can be tuned by varying the intensity of gamma radiation. Irradiation with higher intensity normally gives a homogenous nanoalloy composition whereas with lower intensity produces core-shell morphology. Several bimetallic nanostructures such as Ag–Au, Cu–Ag, Pd–Ag, Pt–Ag, Pd–Au, Pt–Au, Cu–Pd and Ni–Pt are produced. [44]

2.1.6 Sonochemical synthesis

In this method, a mixture of monometallic precursors in appropriate solvent is treated with high power ultra sound. The high power ultra sound can act as reducing agent for the reduction of metallic ions to form bimetallic nanostructures.[45,46] Several factors such as stirring rate, micro-jet stream velocity and shock waves intensity may influence the final morphology of the bimetallic nanostructures.[47] Kan et.al synthesized Au core with palladium shell (Au-Pd) core-shell morphology in ethylene glycol solvent by using sonochemistry.[48] This method can be extended for the synthesis of Au-Ag core-shell structures and Pt-Ph nanoalloy supported on carbon nanotubes. [49,50]

2.1.7 Biological method

Bimetallic nanoparticles can also be produced with help of biomolecules and microbes. Till date several biomimetic synthetic methods are developed for the synthetic of bimetallic nanostructures. For example, Rotello and co-workers have constructed the nanocomposite of Fe-Pt nanoparticles on the DNA.[51] The assemblies of pre-synthesized nanoparticles are directed with the help of DNA. These hybrid nanostructures exhibit different magnetic properties of the nanoparticles. In addition to the biomimetic synthetic methods, several microbes are used for the synthesis of bimetallic nanostructures. Through this strategy, Liu et al. synthesized the Ni-Ti nanoclusters by mixing the Ni and Ti ions with powdered milled alfalfa.[52]

2.2 Basic principles for morphological control of bimetallic nanostructures

In bimetallic system, the grow methods can be adopted due to different reaction conditions. The reaction can follow galvanic replacement reaction when the electrode potentials difference of the two metals drives the reaction reduction. It also can proceed via seed-mediated pathway once a reducing agent is introduced into reaction. Furthermore, in seed-mediated method, low reduction rate is mainly employed for the synthesis of core-shell bimetallic nanocrystals, whereas, fast reduction rate favours the formation of bimetallic dendrites. Co-reduction approach is usually happened with fast reduction rate for the synthesis of bimetallic alloy. The basic key factors for the shape-

selective synthesis of bimetallic nanostructures can be mainly classified into five types: redox potential of two metal precursors, interfacial energy of two metals, reduction rate, facet-specific capping agents, and reaction temperature and time.

2.2.1 Redox potential of two metal precursors

The reduction of a metal precursor mainly depends on its standard reduction potential (SRP). A metal precursor with high positive SRP can be reduced more easily as compared with one with low SRP. According to equation 2.1, the SRP of a metal precursor can be tuned by using different capping agents.[53,54]

$$\varphi^{\circ}([ML_x]^{n-mx}/M) = \varphi^{\circ}(M^{n+}/M) - \frac{0.059}{n}\log K \qquad (2.1)$$

Here, M^{n+} and L^{m-} are metal ions and ligands, respectively. $[ML_x]^{n-mx}$ is the coordinated complex of metal cations and ligands. φ° (M^{n+}/M) and φ° ($[ML_x]^{n-mx}$ /M) represent the SRP of free M^{n+} ions and the complex form, respectively. K is called the stability constant of the complex, which shows the strength of coordinate bonds between metal ions and capping ligands. Clearly, stronger coordinate bond gives larger K value, which leads to the decrease of SPR relative to that of free metal ions. In a reduction reaction, at equilibrium, the metal precursor with high reduction potential will be reduced first as compared with other metal precursors. The redox potential of a metal precursor can be reduced by using halide ions, since they show high affinity

towards noble metal cations. Generally, the reduction potential of noble metals is higher than non-noble ones. Hence, in order to control the bimetallic nanostructures, the reduction potentials of the metal cations are crucial from a thermodynamic perspective. When co-reduction route is used to synthesize bimetallic alloys containing noble metal and non-noble metal, the reduction potential of the noble metal precursor should be decreased with the help of capping ligands. In addition to the reduction potential of the metal precursors, the amount of heat evolved during the mixing of the two metal precursors is also play key factor in the formation of bimetallic alloy nanostructures. The reaction with higher negative values of heat of mixing can easily lead to the formation of alloy nanocrystals. Au-Pt alloy nanostructures are very difficult to synthesize due to positive values of heat of mixing in the reaction. According to the reduction potential of two metals, the formation of the bimetallic nanostructures can follow either galvanic replacement reaction or seed-mediated deposition pathway. For the galvanic replacement, the redox potential difference of the metals is the driving force for the reaction. In some modified galvanic replacement reactions, ligands are added into reactions in order to change the reduction potential of the metal precursor to help the oxidation of the metal core. For instance, the galvanic replacement between the Pd seeds and Pt^{2+} ions can occur only in the presence of Br^- ions.[53] In the absence of Br^- ions, seeded growth synthetic route occurs instead of galvanic replacement reaction.

2.2.2 Interfacial energy of two metals

When metal A and B form bimetallic nanostructures except bimetallic alloys, interfacial energy γ_i is generated due to the formation of new interface. The interfacial energy is determined by the lattice mismatch and the atomic bonds between the two metals at the interface. It determines the types of growth modes bimetallic nanostructures based on the following equation (equation 2.2):

$$\Delta\gamma = \gamma_A + \gamma_i + \gamma_{strain} - \gamma_B \qquad (2.2)$$

Where γ_A and γ_B are the surface energy of metal A and B; γ_{strain} is the strain energy resulted from lattice mismatch of the two metals; $\Delta\gamma$ is the overall surface energy. According to the $\Delta\gamma$, there are three types of growth modes (Figure 2.1). As shown in Figure 2.1a, the first growth mode is the Frank—van der Merwe (FM) at negative $\Delta\gamma$, which can lead to the formation of core-shell structures. In this case, certain prerequisites should be met in order to keep the value of $\Delta\gamma$ negative. First, the lattice mismatch between the two metals should be small enough so that little lattice strain γ_{strain} is introduced when metal A (M_A) is growing on the surface of metal B (M_B). In addition, the surface energy change, which is determined by sum of γ_A and γ_i, should be smaller than the γ_B. If there is a large lattice mismatch and/or larger sum of γ_A *and* γ_i, $\Delta\gamma$ would be a positive value. In this case, M_A forms islands instead of shell on M_B. This growth mode is known as Volmer—Weber (VW) (Figure 2.1c). If the lattice mismatch is large, but the value of $\Delta\gamma$ is negative initially,

several layers of M_A are formed on the surface of M_B. After deposition of a critical layer of M_A, $\Delta\gamma$ increases quickly and finally become positive. Then the islands of M_A atoms are grown on the wetting layer. This growth mode with layer-by layer growth followed by island growth is named as the Stranski-Krastanov (SK) (Figure 2.1b).

2.2.3 Reduction rate

Many factors play a role in controlling the reduction rate of the metal precursors. With fixed redox potentials of the metal precursors, the reduction rate is mainly affected by the reducing agent, pH value, and reaction temperature. Typically, mild reducing agents such as polyol,[55,56] ascorbic acid,[57-59] citric acid,[60] and PVP[61-63] are used to synthesize bimetallic nanostructures with controlled morphologies. This is because the shape of the bimetallic nanocrystals is relatively easy to control in a mild reaction rate. The pH of the solution can also be used to modulate the reduction rate for some reducing agents.[64-67] For example, at high pH, the reducing power of ascorbic acid is significantly larger than that at low pH, causing much faster reduction rate of metal precursors.[68] Different reduction rates at the nucleation and growth stages would produce totally different bimetallic nanostructures.

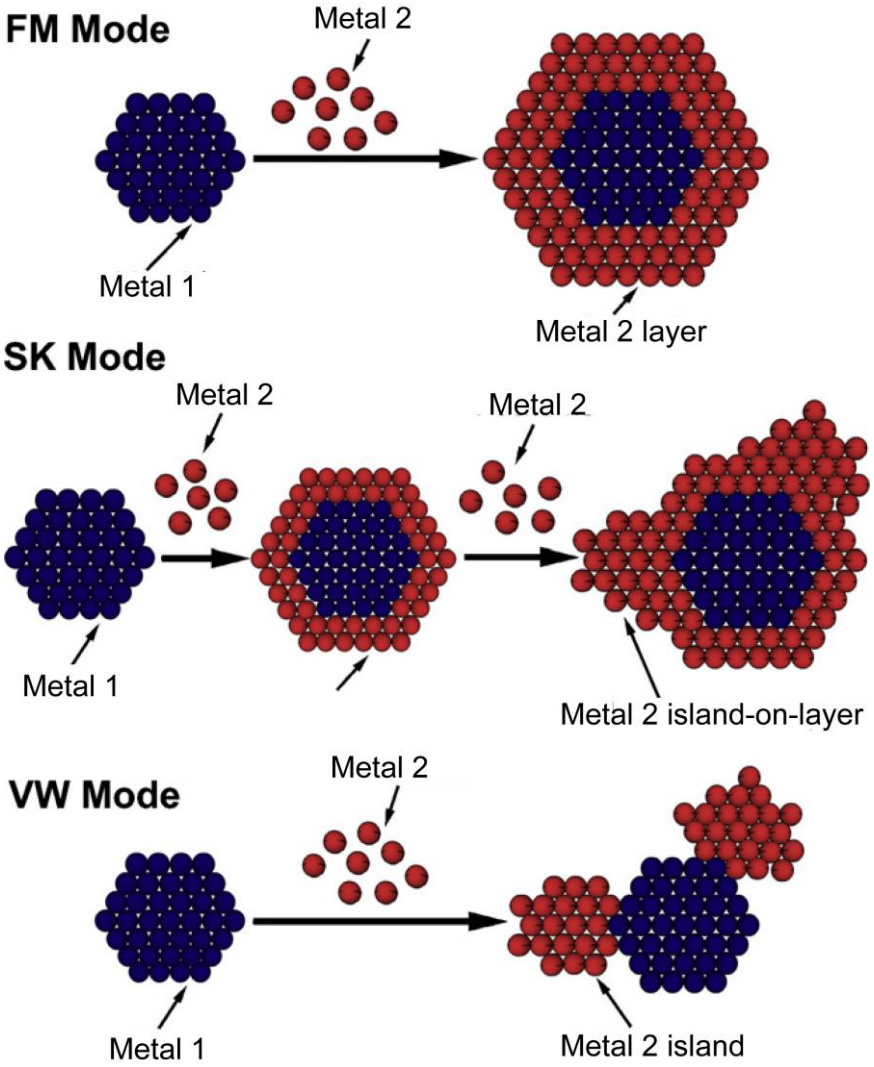

Figure 2.1 Schematic illustration of three different growth modes.[15]

2.2.4 Effect of facet-specific capping agent

Capping agents with specific facet-binding properties are required to control the shape of bimetallic NCs with well-defined shapes. Typical capping agents are surfactants, polymers, ions, or some small molecules. The addition of capping agents in the reaction solution can change the order of energies for different crystallographic planes by interaction of capping agents with the surface of nanoparticle. PVP has been widely used as stabilizer in the

synthesis of metal nanocrystals such as Ag and Pd nanocubes.[69-71] The oxygen atoms in the PVP molecules have the affinity to preferentially bind the {100} facets of Ag and Pd. [10,56,72,73] As the single crystal seeds of Ag and Pd are terminated only with {111} and {100} facets, during the growth of crystal seeds, the atoms are preferentially added to the poorly passivized {111} facets. Similar to PVP the halide ions like Br^- and I^- ions have similar effect that these halides preferentially bind on the {100} facets of Au, Ag, Pt and Pd.[74] Owing to their smaller size, nanocubes, rectangle nanobars and octagonal nanorods with smaller size edge lengths <25 nm can be obtained. Different with the role of PVP and Br-, the citrate ion preferentially binds to the {111} planes of Pd, leading to the formation of octahedrons, icosahedrons and decahedrons.[75,76]. Other small molecules like NO_2 and $C_2O_4^-$ can also serve as capping agents for {111} facets in the syntheses of Pt and Pd based bimetallic nanocrystals.[77,78] These capping agents may lower the surface energy of certain facets to guide the growth of nanocrystals. For examples, cubes are mainly obtained in the reactions using {100} specific capping agents; whereas octahedrons, tetrahedrons and icosahedrons are more likely obtained with {111}-specific capping agents. In addition, the growth rate of facets with higher coverage of capping agents is hindered as compared with facets of less coverage of capping agents. Capping agents may also influence the dissolution of surface atoms of bimetallic NCs and promote the oxidative etching. The final morphology of the bimetallic nanocrystals depends on the relative growth rates of different facets. As a result, the facets with faster growth rates will diminish and the final product contains mainly nanocrystals with facets of

lower growth rates. Though several capping agents are used for the shape controlled synthesis of bimetallic nanostructures, but till date the explicit role of capping agents and mechanism are poorly understood due to lack of experimental techniques to understand the molecular structure of polymeric capping ligands on the surface of nanoparticles. Though a lot of spectroscopic techniques are available such as XPS, EDS, FT-IR and Raman to confirm the presence of capping ligands on the nanoparticles, but none of techniques are capable to resolve the configuration and packing of capping ligands on the nanoparticles.[10]

2.2.5 Temperature and reaction time

Reaction temperature and time are another two important factors for the shape control of bimetallic nanocrystals. Generally, high temperature causes high reduction rate and facilitates the decomposition of the metal precursors. Therefore, reactions at high temperature produce more nuclei and give bimetallic nanocrystals with smaller sizes. The growth and fusion of nuclei in the reaction can be also tuned with the change of reaction temperature. An isotropic growth will take place at high temperature and thermodynamically stable products like spheres or concave polyhedrons are obtained.[79] Conversely, anisotropic growth is preferred at low reaction temperature and bimetallic nanocrystals like nanowires and concave shaped structures are more preferentially synthesized.[80-82] For the synthesis of noble metal bimetallic alloy nanocrystals, higher temperature is generally required. In addition, reaction time also shows a considerable impact on the final morphology of the

bimetallic nanocrystals. In the synthesis of bimetallic nanocrystals, different growth stages of bimetallic nanostructures can be obtained at different reaction time.[54] Generally, in a short period of reaction time, the reaction is at nucleation stage or early growth stage. Bimetallic nanocrystals possess poorly defined shapes. As the reaction time proceeds, bimetallic nanocrystals gradually exhibit well-defined shapes. At later stages, the shape reconstruction and Ostwald ripening take place. Finally, bimetallic nanocrystals with well-defined shapes are formed.

2.3. Morphological Control of Pt-based Bimetallic Nanostructures

2.3.1 Bimetallic dendritic or particle-on-particle structures

Bimetallic dendritic nanostructures have attracted significant attention for electrocatalytic applications. This is because these dendritic (or branched/particle-on-particle) structures with rough surface may provide much improved surface area and/or a high density of defects compared with nanocrystals with smooth surface. Typically, dendritic bimetallic nanostructures can be prepared with metal seeds as the template followed by the growth of nanoparticles of another metal on their surface. The metal seeds can be either pre-prepared as in template-directed synthesis or formed *in situ* as in co-reduction method. Sometimes, a soft template can be employed to guide the growth of the dendritic or branched structures. Pt-based dendritic nanostructures have been mostly studied due to their excellent catalytic

property. In general, the metal seeds are composed of either noble or more active transition metals such as Pd, Au, Cu, Co, or Ni. The formation of Pt dendrites can be either through a simple reduction pathway or *via* a galvanic replacement reaction mechanism, depending on the relative redox potentials of these metals and the presence of reducing agents such as ascorbic acid and trisodium citrate. As mentioned earlier, the growth mode of Pt on the metal seeds is determined by a few factors including lattice mismatch, change in surface energy, and nucleation rate. Briefly, in the case when there is large lattice mismatch between the two metals, which leads to high surface energy excess, the growth will follow the so-called Volmer-Weber (VW) mode to give particle-on-particle morphology. Due to the facile synthesis, there have been a large number of Pt-based bimetallic dendritic structures with various compositions and morphologies (Table 2.1).

Table 2.1 List of dendritic Pt-bimetallic nanostructures, their synthetic methods, and catalytic reactions.

Metal 1	**Metal 2**	**Morphology**	**Synthetic method**	**Reference and catalytic reactions**
Au	Pt	dendrites	seed-mediated growth	ORR[83]; ORR[84]
Au	Pt	dendrites	block copolymer-	No catalytic reaction [85,86]

			assisted method	
Au	Pt	dendrites	block copolymer-assisted method	MOR[87]
Pd	Pt	dendrites	seed-mediated growth	ORR[88]; ORR, FOR[89]
Pd	Pt	dendrites	one-pot sequential synthetic method	ORR[90]
Pd	Pt	dendrites	block copolymer-assisted method	MOR[91]
Ni	Pt	nanobundles	seed-based diffusion route	MOR[92]
Co	Pt	dendrites	co-reduction	ORR[93]
Cu	Pt	dendrites	co-reduction	MOR[94]

Pt-Pd nanodendrites

Pt-Pd bimetallic dendritic nanostructures have been intensively studied due to the superior catalytic properties of both Pt and Pd metals in various reactions such as oxygen reduction, methanol oxidation, and formic acid oxidation. Xia *et al.* obtained Pt-on-Pd bimetallic dendritic structures by reducing K_2PtCl_4 on cuboctahedral Pd nanocrystals (Figure 2.2a-b).[88] The Pt branches grown on Pd core are bounded with {111}, {110}, and high-index {311} facets. These nanostructures were tested for ORR and showed mass activities 2.1 and 4.4 times higher than Pt/C and Pt black reference catalysts, respectively (Figure 2.2c). The enhanced electrocatalytic activity for ORR was attributed to the large surface area and rich active facets of the branched Pt structures. The growth mechanism of the Pt-Pd dendrites was also investigated in a later study of the same group.[89] It was found that at the very beginning of the reaction, Pt homogeneous nucleation took place with heterogeneous nucleation – while homogeneous nucleation led to the formation of tiny Pt nanoparticles, heterogeneous nucleation of the tiny particles via oriented attachment gave Pt branches. Similar Pt-on-Pd bimetallic dendritic nanostructures were also obtained *via* a sequential synthetic method reported by Yang and coworkers (Figure 2.2d-e).[90] In their synthesis, Pd nanoparticles were prepared first by decomposing palladium acetylacetonate. The resultant 5-nm Pd nanoparticles were then employed as seeds for the growth of 3-nm Pt nanoparticles to give Pt-on-Pd dendritic heteronanostructures. They studied the electrocatalytic activity and stability of the Pt-on-Pd dendritic

nanostructures supported on carbon black for ORR. The area-specific activity of Pt-on-Pd dendritic structures was almost twice that of Pt black reference catalyst (Figure 2.2f).[90] Meanwhile, the Pt-on-Pd dendritic structures showed an unusually high long-term stability – when cycled between 0.6 to 1.0 V for 30000 times, the Pt-on-Pd dendrites showed an ECSA loss of only 12%, which is in stark contrast to a loss of 39% for Pt black. Both methods developed by Xia group and Yang group for the preparation of Pt-Pd dendritic nanoparticles are based on seeded growth – in which Pd nanoparticles are formed before they are used as seeds to direct the growth of Pt nanoparticles on their surfaces. In a later work, Yamauchi and co-workers discovered a simple and mild co-reduction pathway for the preparation of Pt-on-Pd nanodendrites.[91] In their synthesis, Pluronic P123 was used to assist the reduction of K_2PtCl_4 and Na_2PdCl_4 simultaneously at room temperature. It was found that Na_2PdCl_4 can be reduced faster than K_2PtCl_4, therefore Pd nanocrystals were formed first and acted as *in situ*-generated seeds for the deposition of Pt. The resultant Pt-Pd bimetallic nanodendrites were composed of Pd cores and Pt dendritic shells (Figure 2.2g). It was found that the copolymer Pluronic P123 also acted as template for the formation of Pt branches. The Pt braches grown on Pd core mainly showed {111} facets are highly active for electrocatalytic oxidation of methanol. Comparison of MOR activities of Pt-on-Pd dendrites with different compositions indicated that nanocrystals obtained at larger Pt/Pd ratios have better electrocatalytic performance (Figure 2.2h).[91]

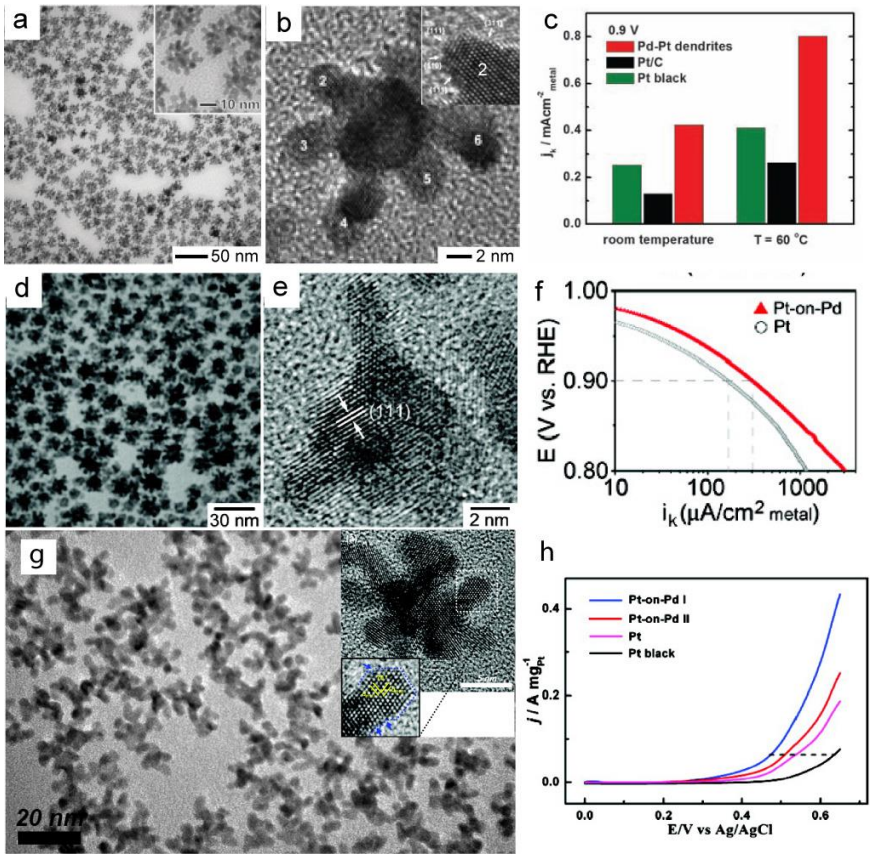

Figure 2.2 (a-c) Pd-Pt bimetallic nanodendrites and specific activities for ORR.[88] (d-f) Pt-on-Pd bimetallic nanopsrticles and specific kinetic current density of ORR.[90] (g-h) Pt-on-Pd bimetallic nanodendrites and current densities for MOR.[91]

Pt-Au nanodendrites

Although Au alone is not an active catalyst for fuel cell applications, Adzic *et al*. found that when small Au clusters were decorated onto Pt nanocrystals, the resulting bimetallic structure exhibited extremely high durability towards ORR.[95] In the meantime, various studies have also shown that Au nanostructures decorated with Pt nanoparticles can show good activity and durability for electrocatalytic reactions. To this end, a number of Au nanostructures have been employed as seeds to grow Pt-Au bimetallic

dendritic structures. Since Au is nobler than Pt, reducing agent has to be used to induce the formation of Pt on Au template. For example, Han *et al.* synthesized Au@Pt dendritic core-shell heterostructures using Au nanoparticles with shapes including cube, rod, and octahedron as seeds (Figure 2.3a-c).[84] While all dendritic Pt shells formed on Au cores with different shapes exhibited larger electrochemical surface area (ECSA) than that of Pt dendrites prepared without Au, those grown on Au octahedron showed the largest ECSA. The mass activities of ORR for the dendritic Pt shells on different Au templates decreased following the order of Au octahedron>rod>cube. These results indicate that the electrocatalytic performance of the Au@Pt bimetallic nanostructures is dependent on the core morphology. Furthermore, the Au@Pt core-shell nanostructures also exhibited better durability compared to monometallic Pt dendrites. The improved durability of the Au@Pt bimetallic heterostructures was attributed to the incorporation of Au core to the dendritic structures.

Similar Au@Pt dendritic core-shell nanostructures were also prepared by Yamauchi *et al.* with a one-step co-reduction method with Pluronic F127 block copolymer as the surfactant.[85] In a nearly parallel work, Wang *et al.* used Pluronic F127 to synthesize noncompact Pt-on-Au dendritic nanoparticles.[87] Later, Yamauchi and coworkers improved this surfactant-assisted method by applying ultrasonic treatment to decrease the Au@Pt particle size and narrow the size distribution.[86] The resultant Au@Pt dendritic nanoparticles showed a Brunauer-Emmett-Teller (BET) specific area twice as

large as that of Pt dendritic nanoparticles when normalized to Pt mass loading. They also found that the electrocatalytic activity of the Au@Pt dendritic core-shells for MOR can be tuned by changing the ratio of Au:Pt -- when the molar ratio Pt:Au was 1:1, the Au@Pt dendrites showed an optimum peak current density approximately 4 times higher than that of monometallic Pt dendritic nanoparticles.[86]

In addition to Au nanoparticles, one-dimensional Au nanowires have also been used as template to form Au@Pt dendritic structures. Zheng *et al.* obtained 1-D Au@Pt core-shell dendrites with dense and tiny Pt dendrites decorated on Au nanowires *via* a seed-mediated method (Figure 2.3d-f).[83] This self-supported Au@Pt dendritic structure exhibited much enhanced electrocatalytic activity and better stability for ORR compared to Pt/C. Compared to nanoparticle-based templates, 1-D Au nanowires as support for Pt catalyst can form nanowire network which allow efficient electron transfer.

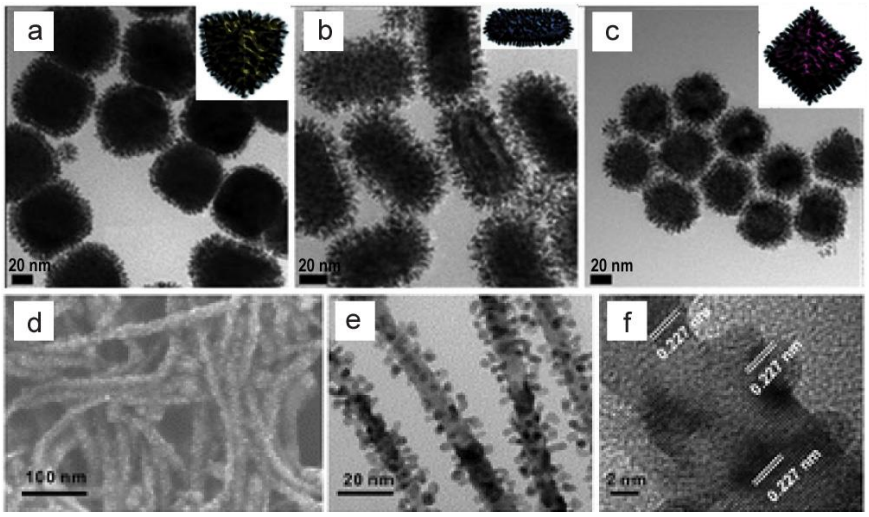

Figure 2.3 (a-c) Au@Pt dendritic core-shell structures using Au nanocubes, nanorods, and octahedra as seeds, respectively.[84] (d-f) Au/Pt nanowires with dendritic Pt shell on Au nanowires.[83]

Pt-M nanodendrites (M= Ni, Co, Cu, etc)

To lower the loading of precious noble metals in electrocatalysts, considerable efforts have been made by various groups to prepare Pt-M (M = transition metals such as Cu, Co, Ni, etc.) bimetallic nanostructures. The replacement of noble metals with earth-abundant transition metals may significantly lower the cost of electrocatalysts. In addition, the more active transition metals may also serve as oxophilic element in the catalysts. This approach has strong impact for the preparation of electrocatalysts resistive to CO poisoning since the presence of an oxophilic element in Pt-based catalysts can facilitate the formation of oxygen species on the catalyst surface. To date, a number of Pt-M dendritic structures have been synthesized *via* co-reduction or seeded growth method. For example, Zhao *et al.* obtained Pt-Cu bimetallic nanodendrites by co-reduction of H_2PtCl_4 and $CuCl_2$ in the presence of

Pluronic F127 block copolymer and formic acid (Figure 2.4a-b).[94] The resultant Pt-Cu nanodendrites exhibited higher electrocatalytic activity for MOR than commercial Pt/C catalyst. Also based on a co-reduction approach, Gu *et al.* synthesized Pt-Co dendritic alloy nanoparticles that showed an ORR activity 4.5 times higher than that of Pt/C catalyst (Figure 2.4c-f).[93] Seeded-growth has also been employed to form Pt-transition metal nanodendrites. For example, Li *et al.* reported the preparation of highly branched Pt–Ni bimetallic nanobundles *via* a seed-based diffusion synthetic route.[92] In their synthesis, branched Pt nanostructures were formed by reducing H_2PtCl_6 in octadecylamine. These pre-formed Pt structures were then used as seeds to allow the diffusion of Ni species that were generated by reducing $Ni(NO_3)_2$. The resultant Pt-Ni bimetallic nanobundles were found rich of step surface and showed an MOR activity 3.6 times higher than that of Pt nanoparticles. The enhanced activity was attributed to both the high-density surface active sites and the incorporation of Ni in the structure. In addition, the Pt-Ni nanobundles also exhibited better stability than Pt nanoparticles – 55% of initial peak current density was retained after 4000 cycles for Pt-Ni, while only 10% was obtained for Pt nanoparticles after the same number of cycles (Figure 2.4g-j). More importantly, tolerance to CO poisoning was also significantly improved – CO stripping experiments confirmed that the oxidation potential of CO on Pt-Ni nanobundles shifted negatively by 0.06 V relative to that of Pt nanoparticles, indicating that CO species on the Pt-Ni surface can be removed more efficiently.[92]

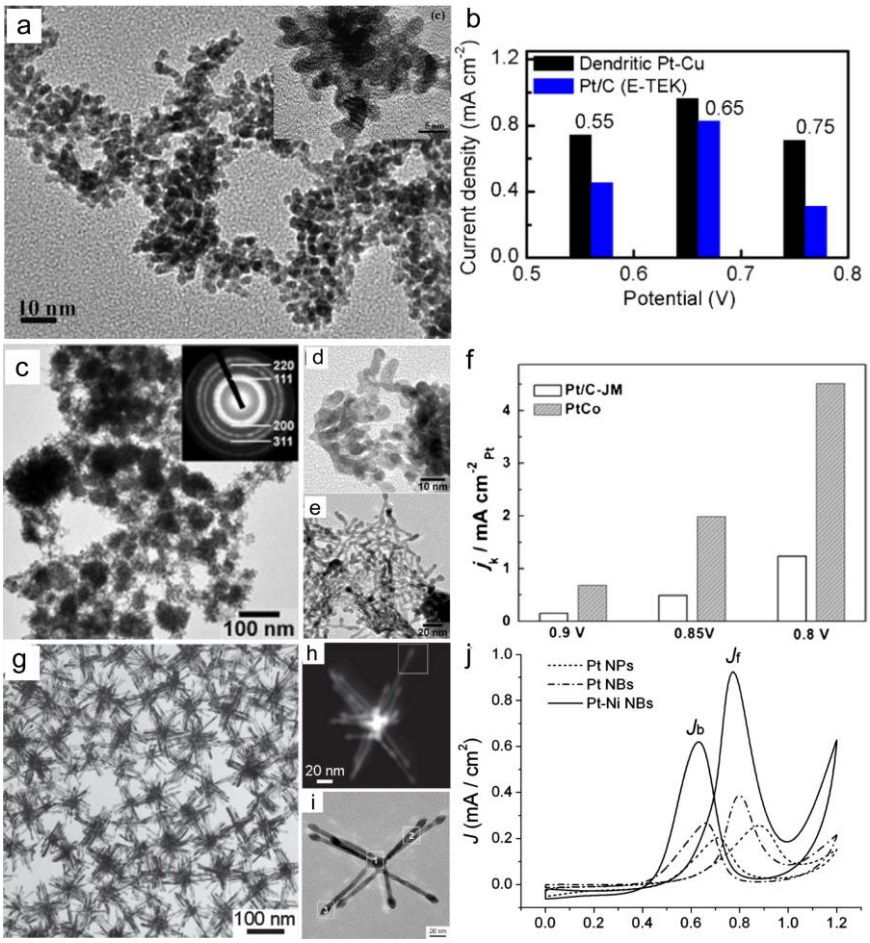

Figure 2.4 (a,b) Pt-Cu nanodendrites and area-specific activities for MOR.[94] (c-e) Pt-Co nanodendrites, (f) area-specific activities.[93] (h-j) Pt-Ni nanobundles and their CVs for MOR.[92]

2.3.2 Bimetallic alloy nanocrystals with polyhedral shapes

Shape-selective growth of bimetallic alloy nanocrystals with well-defined facets has emerged dramatically in recent years. To date, Pt-M bimetallic nanocrystals with various polyhedral shapes such as cube, octahedron, and icosahedron have been prepared by a number of research groups. Some general methods in tuning the shapes have been developed. Thanks to the availability of a broad range of bimetallic nanocrystals with controlled shapes,

uniform sizes, and well-defined facets, advances in understanding both the growth mechanisms and the effect of different facets on catalytic activities have evolved rapidly (Table 2.2).

Table 2.2 List of Pt-based bimetallic alloy nanostructures with polyhedral shapes, their synthetic methods, and catalytic reactions.

Metal 1	**Metal 2**	**Morphology**	**Synthetic method**	**Reference and catalytic reactions**
Fe	Pt	NCs	co-reduction	[28]; MOR, FOR[96]
Co	Pt	NCs	co-reduction	[28]; MOR[97]; ORR[12]
Ni	Pt	NCs	co-reduction	[28]; ORR[98]
Cu	Pt	NCs	co-reduction	MOR[99]; FOR[100]
Cu	Pt	NCs, concave NCs	co-reduction and GRR	MOR[101]
Mn	Pt	NCs	co-reduction	ORR, MOR, FOR[102]
Pd	Pt	NCs	co-reduction	FOR[103]
Pd	Pt	concave NCs	co-reduction	ORR[53]
Pd	Pt	NCs	co-reduction	MOR[104]
Zn	Pt	NCs	co-reduction	MOR[105]

Pd	Pt	NCs	co-reduction	[106]
Ni	Pt	octahedra, truncated octahedra	co-reduction	ORR[98,107,108]
Ni	Pt	octahedra	solvothermal method	ORR[109]
Pd	Pt	tetrahedra	co-reduction	MOR[104]
Pd	Pt	octahedra	co-reduction	MOR[110]; ORR[111]
Pd	Pt	icosahedra	gas reducing agent in liquid solution (GRAILS) method	ORR[21]

2.3.2.1 Bimetallic alloy nanocrystals with cubic shape

Pt-Pd nanocubes

Wang *et al.* synthesized PdPt bimetallic alloy nanocubes with monodisperse size and tunable composition *via* co-reduction method in an aqueous medium (Figure 2.5a-c).[103] These PdPt nanocubes exhibited enhanced electrocatalytic activity towards FOR compared with Pd sub-10 nm nanocubes and commercial Pd black. The maximum peak current of the PdPt nanocubes was obtained at a Pt content of 25.6 at.%. In addition to co-reduction method,

galvanic replacement reaction as a synthetic approach can also be used to give Pd-Pt bimetallic cubic nanostructures. Xia *et al.* synthesized Pd-Pt concave nancubes via Br^--assisted galvanic replacement reaction using Pd nanocubes as template to react with $PtCl_6^{2-}$.[53] It was found that because Br^- ions preferentially adsorb on the {100} facets of Pd nanocrystals, they could facilitate the galvanic replacement reaction on {100} facets of the Pd template. The Pd-Pt concave structures with different Pt contents were obtained and those with 3.4 wt% Pt showed 4-times ORR activity as that of commercial Pt/C catalyst.

Yan *et al*. also took the advantage of the preferential adsorption of small ions such as Br^- or I^- as facet-selective agent to prepare sub-10 nm Pt-Pd nanocubes.[104] The Pt-Pd nanocubes were tested for MOR and showed an activity 1.3 and 2.9 times higher than that of Pt-Pd nanotetrahedra and commercial Pt/C catalyst, respectively. The enhanced electrocatalytic activity of Pt-Pd nanocubes relative to tetrahedra was attributed to the different reaction pathways of MOR on {100} and {111} facets.[104] Again with the assistance of different halides ions such as Cl^- and I^- as the shape-directing agent, Huang *et al.* obtained Pt-Pd nanocubes. The composition of the Pt-Pd nanocubes can be controlled by changing the molar ratio of the starting precursors (Figure 2.5d-f).[106] It was found that the catalytic performance is highly dependent on the shape of the Pt-Pd structure -- the optimum activity was achieved when the Pt-Pd nanocrystals were bounded with {100} rather than {111} facets.[106]

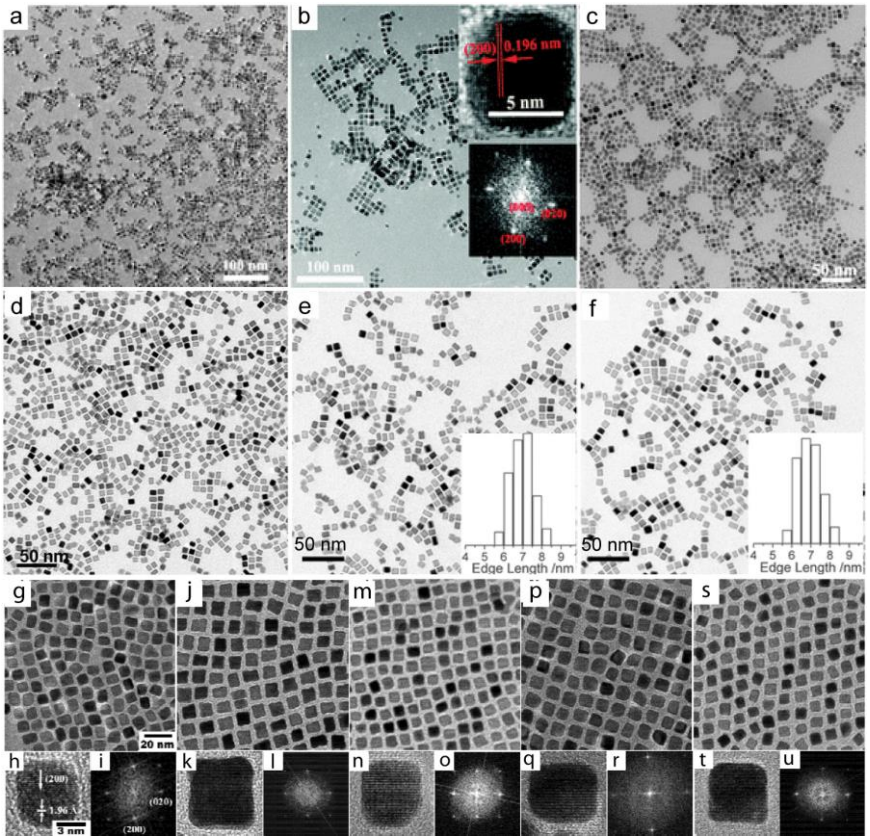

Figure 2.5 (a) $Pd_{80.8}Pt_{19.2}$, (b) $Pd_{74.4}Pt_{25.6}$, and (c) $Pd_{66.0}Pt_{34.0}$ bimetallic nanocubes[103]. (d) $Pt_{51}Pd_{49}$, (e) $Pt_{34}Pd_{66}$, and (f) $Pt_{67}Pd_{33}$ bimetallic nanocubes.[106] (g–i) Pt_9Co, (j–l) Pt_7Co, (m–o) Pt_5Co, (p–r) Pt_3Co, and (s–u) Pt_2Co bimetallic nanocubes.[12]

Pt-M nanocubes (M=Co, Ni, Cu, Fe, Mn, Zn)

In addition to Pd, many transition metals such as Co, Ni, Cu, Fe, Mn and Zn have also been intensively studied to form cubic alloy with Pt. For instance, Choi *et al.* synthesized composition-tunable Pt_xCo (x = 2, 3, 5, 7, and 9) alloy nanocubes in a co-reduction approach *via* changing the amounts of Co precursor and found that the electrocatalytic performance on ORR highly depended on Co composition (Figure 2.5g-u).[12] Also *via* a co-reduction approach, Xu *et al.* synthesized uniform Pt-Cu nanocubes (Figure 2.6a-c).[99] It

was found that the use of multiple capping agents, including tetraoctylammonium bromide (TOAB) and oleylamine, played a key role on controlling both the shape and the size of the nanocubes. The formation of the cubic shape was attributed to stabilization of Br^- ions that preferentially adsorb on {100} facets of the Pt-Cu nanocubes. Meanwhile, oleylamine was important in stabilizing the Pt and Cu clusters at nucleation stage. At growth stage, oleylamine synergistically controlled the cubic shape with TOAB. The electrocatalytic activity of the Pt-Cu nanocubes for MOR was evaluated in comparison with spherical Pt-Cu and Pt nanocrystals with similar sizes. It was found that the current density of Pt-Cu nanocubes was 1.4 and 5.3 times higher than those of Pt-Cu nanospheres and Pt nanocrystals, respectively, indicating that the electrocatalytic activity of Pt-Cu nanostructures is highly dependent on their facets.[99] In a later work of the same group, they further tuned the composition of the bimetallic Pt_xCu_{100-x} nanocubes (x = 54-80 atom%) and investigated the electrocatalytic activity and long-term stability for FOR.[100] It was found that $Pt_{80}Cu_{20}$ nanocubes exhibited the best electrocatalytic performance compared to the nanocubes containing less Pt. Using a one-pot hydrothermal process, Yan *et al*. also prepared Pt-Cu nanocubes and concave nanocubes via a galvanic replacement reaction approach assisted by Br^- ions.[101] The Pt-Cu concave nanocubes were bounded with multiple {hk0} high-index steps and facets. The Pt-Cu concave nanocubes exhibited a higher specific activity for MOR than the Pt-Cu nanocubes, Pt nanocubes and Pt/C catalyst.

Fang *et al*. conducted a series of work to investigate the preparation of Pt_3M nanocubes (M = 3d-transition metals including Co, Fe, and Ni) (Figure 2.6d-l).[28,96,97] In their syntheses, tungsten hexacarbonyl [$W(CO)_6$] was used to control the nucleation and growth. Meanwhile, oleylamine and oleic acid with different ratios were used as both the solvent and surface stabilizer to obtain cubic shape. $W(CO)_6$ was found to play critical role in morphological control for the formation of cubic shape. This is because the introduction of $W(CO)_6$ mediates the reduction of Pt^{2+} ions at the nucleation and growth stages *via* the reaction of $Pt^{2+} + W^0 \leftrightarrow W^{n+} + Pt^0$. Therefore, the reduction of Pt^{2+} is slowed down to facilitate a steady crystal growth with sustained feedstock of Pt.[96] The resultant Pt_3M nanocubes exhibited better electrocatalytic activity for MOR and FOR relative to spherical Pt_3M or Pt nanocubes.[96,97] This is because of slow CO adsorption and facile CO desorption on the surface of nanocubes.[97]

Also as an effort to reduce the Pt loading and to improve CO poisoning tolerance, Murray *et al.* synthesized Pt-Mn nanocubes with uniform size *via* a co-reduction method (Figure 2.6m).[102] The Pt-Mn nanocubes were obtained *via* hot injection of $Mn_2(CO)_{10}$ into a solution containing $Pt(acac)_2$, oleic acid and oleylamine. However, when $Mn_2(CO)_{10}$ was added into the reaction solution instead of hot injection, Pt-Mn nanoparticles instead of nanocubes were formed. The Pt-Mn nanocubes exhibited enhanced ORR activity three times higher than commercial catalyst. It was also found that the ORR activity of Pt-Mn was both shape- and electrolyte-dependent -- the {111} facets of Pt-Mn showed higher ORR activity than {100} facets in $HClO_4$, while the

opposite was observed in H_2SO_4.[102] In another work, the same group also investigated the growth of monodisperse PtZn nanocubes and nanospheres (Figure 2.6n).[105] The Pt-Zn nanocrystals exhibited much improved tolerance of CO poisoning in MOR compared to other Pt-M bimetallic nanocrystals.

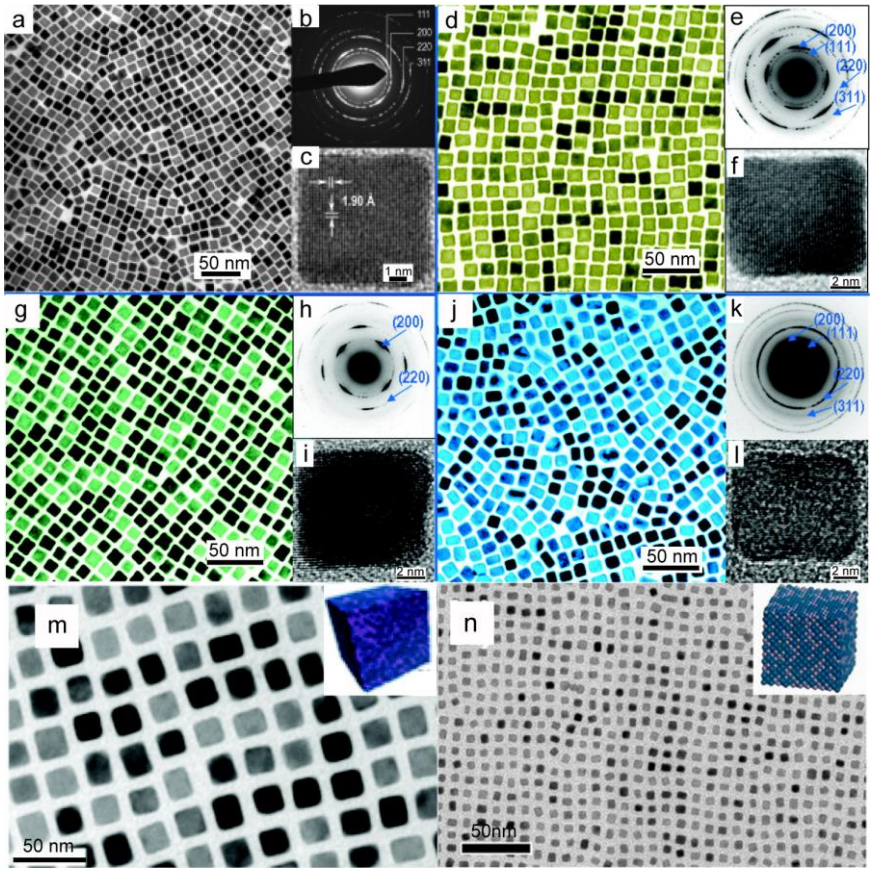

Figure 2.6 (a-c) Pt-Cu bimetallic nanocubes.[99] (d-f) Pt_3Co bimetallic and (g-i) Pt_3Fe bimetallic nanocubes; (j-l) Pt_3Ni bimetallic nanocubes.[28] (m) Pt-Mn bimetallic nanocubes.[102] (n) Pt-Zn bimetallic nanocubes.[105]

2.3.2.2 Bimetallic alloy nanocrystals with other polyhedral shapes

Pt-Pd alloy polyhedra

Pt-Pd bimetallic nanocrystals with tetrahedral and octahedral shapes bounded by {111} facets have also been prepared by various researchers. For instance, Yan *et al.* obtained sub-10 nm Pt-Pd tetrahedra using $Na_2C_2O_4$ to stabilize {111} facets of Pt-Pd tetrahedra (Figure 2.7a-b).[104] The resultant Pt-Pd tetrahedra showed better stability towards MOR than that of Pt-Pd nanocubes and commercial Pt/C catalyst. Huang *et al.* also obtained Pt-Pd octahedra and tetrahedra instead of nanocubes by switching the shape-directing agent from I^- to Cl^- ions (Figure 2.7c-d).[106] Park *et al.* reported a polyol process to grow octahedral Pt–Pd nanoparticles in aqueous solution.[110] The octahedral Pt-Pd nanoparticles are well-defined alloy nanostructures with dominant {111} facets. They further tuned the composition of the Pt-Pd alloy nanoparticles to form Pt_3Pd_1, Pt_1Pd_1, and Pt_1Pd_3 octahedra.[111] Among the alloy nanocrystals with different compositions, octahedral Pt_3Pd_1 exhibited much enhanced electrochemical performance for ORR relative to Pt_1Pd_1, and Pt_1Pd_3.

Pt-M (M=Ni, Cu, Au) alloy polyhedra

Following a similar synthetic approach of Pt_3Ni nanocubes, Fang *et al.* also prepared Pt_3Ni nanoctahedra by changing the injection rate of Ni precursor (Figure 2.8a-b).[98] It was found that while slow injection of Ni precursor facilitates the growth of nanocubes, fast addition causes the formation of octahedra. The Pt_3Ni octahedra bounded by {111} facets showed much-enhanced electrocatalytic activity for ORR compared to Pt_3Ni nanocubes and Pt nanocubes. Yang *et al.* also employed a facile co-reduction approach to prepare Pt_3Ni truncated-octahedra (Figure 2.8c-d).[107] In their

synthesis, adamantanecarboxylic acid (ACA) or adamantaneacetic acid was added to mediate the reaction kinetics. They studied the effect of alkane-chain length of amines on the shape control of Pt_3Ni. It was found that three different amines including octadecylamine, hexadecylamine and dodecylamine resulted in truncated-octahedra with yields of 70%, 90%, and 100%, respectively. This trend indicates that short-alkane-chain amine favors the formation of truncated-octahedra. In a subsequent work, Yang *et al.* systematically studied the effect of reaction parameters including capping agent, reducing agent, and reaction time on controlling the shape of the Pt_3Ni nanocrystals.[108] They further investigated the electrocatalytic performance of Pt_3Ni nanocrystals with 70%, 90%, and 100% of truncated octahedra for ORR in alkaline medium. It was confirmed that the Pt_3Ni (111) surface has much higher ORR activity than (100) surface.

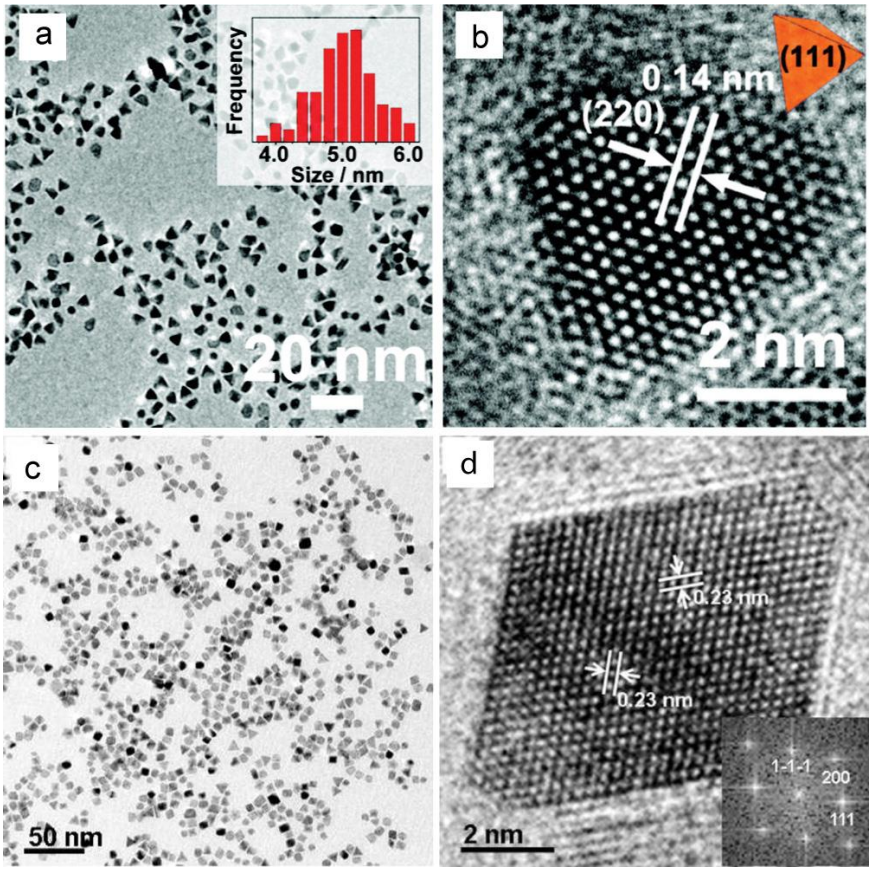

Figure 2.7 (a-b) Pt-Pd tetrahedra.[104] (c-d) $Pt_{52}Pd_{48}$ octahedra/tetrahedra.[106]

In addition to octahedra, multiple-twinned icosahedral nanocrystals are also bounded by {111} facets. Yang *et al.* reported several types of Pt-M (M=Au, Ni, and Pd) alloy icosahedral nanocrystals synthesized in solution by using carbon monoxide gas as both the reducing agent and the capping agent to stabilize {111} facets (Figure 2.8e).[21] It is interesting that although both icosahedron and octahedron are bounded by {111} facets, the ORR activity of Pt_3Ni icosahedra was found to be higher than that of the octahedra. To understand the difference in ORR activity of Pt_3Ni with different shapes but same facets, they conducted density function theory (DFT) calculations and molecular dynamics (MD) simulations which suggested that the diffuse elastic

strain present at the twin boundaries within icosahedral nanocrystals should be the main reason of the difference in ORR activity between Pt_3Ni icosahedra and octahedra.[21]

In addition to the abovementioned cubic, octahedral and icosahedral nanocrystals, other polyhedral shapes of Pt-M alloy nanocrystals have also been reported. For example, based on a one-pot strategy, Li *et al.* synthesized bimetallic Pt-Cu hexapod nanostructure with high-index {112} facets (Figure 2.8f-g).[112] A growth mechanism for the formation of Pt-Cu hexapods was proposed. It is believed that Pt-Cu nanocrystals with rhombic dodecahedral shape were generated first at the beginning of the reaction. Following etching of the apexes and facets led to the concave hexapod nanostructure. The bimetallic Pt-Cu hexapod concave nanocrystals exhibited an electrocatalytic MOR activity 2.5 times higher than that of commercial Pt black.[112]

2.3.3 Porous/hollow Pt-based bimetallic nanostructures

Bimetallic nanoparticles with porous or hollow structure possess large surface area and have shown great promise as electrochemical catalyst. Typically, porous bimetallic nanostructures can be generated *via* galvanic replacement reaction or dealloying method. In a typical galvanic replacement reaction approach, nanotemplates composed of a more active metal are reacted with the precursor of the second metal. Based on the different reduction potentials, the second metal is reduced and deposited onto the templates at the expense of the first metal to form hollow structures. Another method is based

on dealloying of bimetallic nanostructures. The bimetallic alloy nanostructures can be prepared first *via* methods such as co-reduction of two metal precursors. Afterwards, dealloying will be performed using methods such as electrochemical etching or chemical leaching by adding an etchant that can dissolve the more active metal from the alloy. With the dissolution of the more active metal, a porous structure can be generated (Table 2.3).

Table 2.3 List of porous/hollow Pt- and Pd-based bimetallic nanostructures, their synthetic methods, and catalytic reactions.

Metal 1	**Metal 2**	**Morphology**	**Synthetic method**	**Reference and catalytic reactions**
Pd	Pt	porous dendrites	GRR	MOR[113]; ORR[114]
Ag	Pt	hollow boxes	GRR	MOR[115]
Ag	Pt	hollow dimers	GRR	MOR[115]
Ag	Pt	popcorns	GRR	MOR[115]
Pd	Pt	porous	co-reduction and seed-mediated method	FOR[116]
Pd	Pt	nanocages	GRR	CO oxidation[117];

				FOR[118]
Ni	Pt	nanoporous alloy	dealloying	No catalytic reaction [32]
Co	Pt	nanoporous alloy	dealloying	No catalytic reaction[32]
Cu	Pt	nanoporous alloy	dealloying	ORR[119]
Cu	Pt	nanotubes	GRR	No catalytic reaction[120]

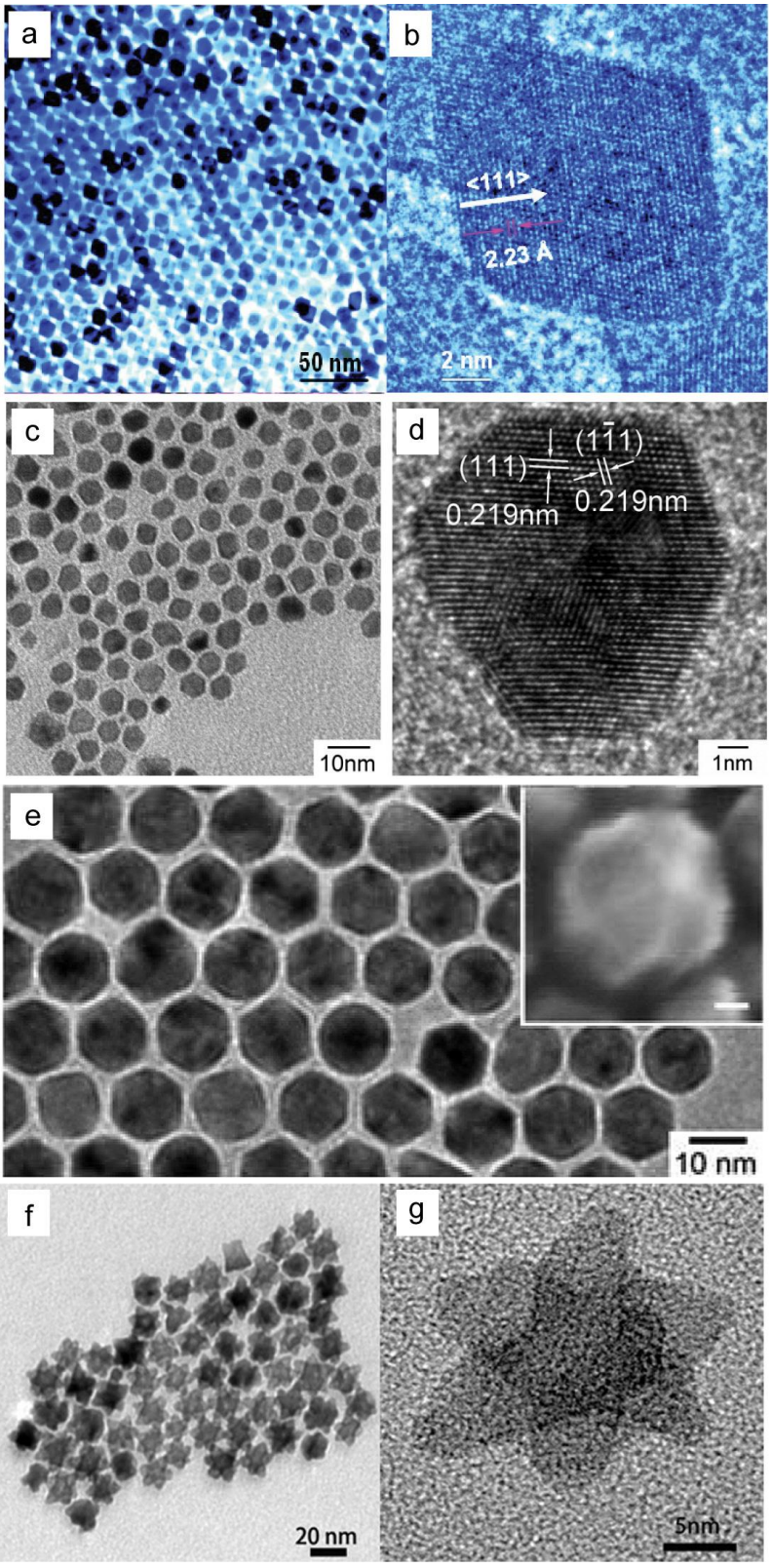

Figure 2.8 (a-b) Pt_3Ni octahedra.[98] (c-d) Pt_3Ni truncated octahedra.[107] (e) Pt3Ni icosahedra.[21] (f-g) Pt-Cu hexapods.[112]

Based on galvanic replacement reaction approach, Wang *et al*. synthesized ultra-long Pt-on-Pd nanowires consisting of small Pt nanobranches supported on Pd nanowire. In their work, Te nanowires were firstly obtained and used as sacrificial template for the synthesis of Pd nanowires *via* the replacement reaction between Te and H_2PdCl_4. Subsequently, the preformed Pd nanowires were used as seeds to direct the growth of Pt nanobranches *via* the reduction of K_2PtCl_4 by ascorbic acid. Due to the branched structure, the Pt-on-Pd nanowires showed a high ESCA (90.7 m^2/g) and much enhanced electrocatalytic activities for MOR relative to commercial Pt/C catalyst (Figure 2.9a-c).[113] Porous Pt-Pd bimetallic nanostructures have also been obtained *via* the replacement reaction between Pd nanocrystals and Pt precursors. In a recent work, Han *et al.* applied Pd octahedra and nanocubes as template to synthesize Pd-Pt bimetallic octahedral and cubic nanocages *via* the reaction between Pd and K_2PtCl_4 in the absence of other reducing agent.[114] They also found that if small amount of ascorbic acid was added as reducing agent to facilitate the reduction of Pt precursor, dendritic hollow nanocrystals instead of nanocages were obtained. Once large amount of ascorbic acid was introduced, the final structures were octahedral and cubic core-shell dendrites. They further employed the Pd-Pt nanostructures with different morphologies as electrocatalysts for ORR. The results showed that the Pd-Pt nanocages have better performance than Pd-Pt dendritic hollow or core-shell structures. It is also interesting to note that all the structures obtained from octahedral templates showed better

electrochemical performance than those obtained from nanocubes (Figure 2.9d-e).[114]

Li *et al*. developed a general dealloying approach to form nanoporous Pt-Ni and Pt-Co nanoparticles.[32] In their work, bimetallic nanocrystals were prepared first using a so-called noble-metal-induced-reduction method. Subsequently, the less noble component (Ni or Co) of the nanocrystals was selectively dissolved with nitric acid to create a porous structure. The resultant nanoporous particles exhibited relatively high BET surface areas (~60 m^2/g) and ECSA (~85 m^2/g), indicating that these bimetallic nanostructures are promising electrochemical catalysts.

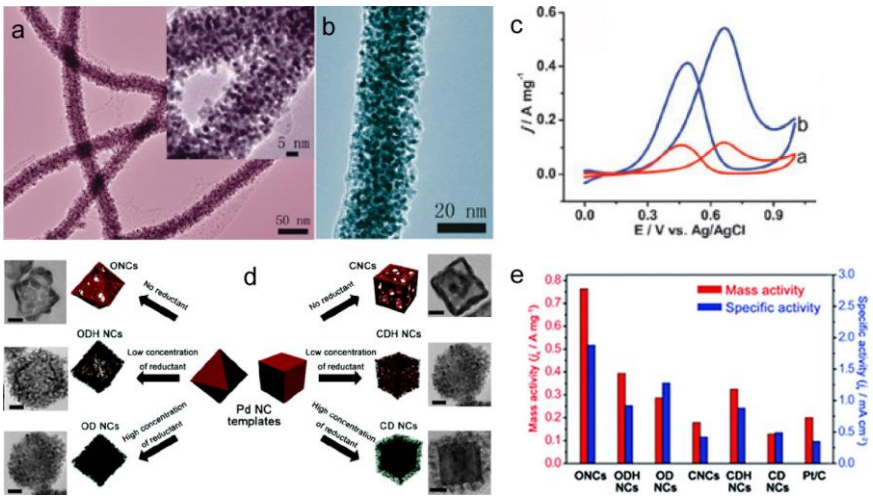

Figure 2.9 (a-c) Pd-Pt dendritic nanowires and CVs for MOR.[113] (d,e) Pd-Pt dendritic nanocrystals and mass- and area-specific activities for ORR.[114]

2.3.4 One-dimensional bimetallic alloy nanorods or nanowires

One-dimensional bimetallic nanostructures including nanorods and nanowires may exhibit superior electrocatalytic activities compared to

nanoparticles. This is because this type of structures may allow efficient electron transfer due to the interconnected conductive pathways. Similar to monometallic nanowires/nanorods, one-dimensional bimetallic nanostructures can be formed based on either template-directed growth or oriented attachment mechanisms (Table 2.4). For template-based methods, the template can be either soft templates such as micelles formed from surfactant within certain solvents, or inorganic templates such as nanowires of an active metal (e.g., Te). Oriented attachment of nanoparticles is another approach for the formation of 1-D bimetallic nanostructures. In this approach, small metallic nanoparticles collide in solution and fuse together along one direction by forming metallic bonds at the interfacial sites to grow into nanowires.

Table 2.4 List of one-dimensional Pt- and Pd-based bimetallic nanostructures, their synthetic methods, and catalytic reactions.

Metal 1	**Metal 2**	**Morphology**	**Synthetic method**	**Reference and catalytic reactions**
Fe	Pt	nanorods/nanowires	co-reduction	No catalytic reaction[31]
Pd	Pt	nanowire networks	soft template	No catalytic reaction[121]
Ru	Pt	nanowire networks	soft template	No catalytic reaction[121]
Au	Pt	nanowire	soft template	No catalytic

		networks		reaction[121]
Fe	Pt	nanowire networks	soft template	No catalytic reaction[121]
Cu	Pt	nanorods	co-reduction	CO oxidation[122]
Cu	Pt	nanotubes	GRR	No catalytic reaction[120]
Ag	Pt	nanowires	oriented attachment	No catalytic reaction[123]

Sun *et al.* reported a synthesis of ultrathin FePt and CoPt nanorods/nanowires in hot organic solution containing oleylamine and octadecene (Figure 2.10a-c).[31] The length of the nanorods/nanowires can be tuned by varying the volume ratio of oleylamine and octadecene. It was believed that oleylamine self-organized into a micelle-like structure within octadecene solvent and directed the growth of FePt or CoPt nanowires as soft template. Also with octadecene as the solvent, Schaak *et al*. synthesized CuPt nanorods with tunable lengths and aspect ratios in the presence of oleylamine and oleic acid (Figure 2.10d-g).[122] It was found that the activity of CuPt nanorods for CO oxidation was much higher than that of commercial Pt/Al_2O_3 catalyst. Yang *et al.* also developed a general soft template method for the preparation of ultrathin Pt-M (M = Pd, Ru, Au, Fe) alloy nanowire networks.[121] In their method, the nanowires were grown within the micelles

formed in a two-phase (water-chloroform) system with CTAB as a soft template.

Nanowires composed of two metals have also been prepared using hard templates such as Te nanowires. Based on this method, Dong *et al*. obtained ultrathin PdPt and PdAu nanowires.[124] In this work, Te nanowires were employed as both sacrificial template and reducing agent to react with precursors of Pd, Pt or Au. The electrocatalytic performances of PdPt nanowires with different ratios of Pd to Pt were tested for ethanol and methanol oxidation reactions. It was found that $Pd_{45}Pt_{55}$ has much higher activity than that of $Pd_{80}Pt_{20}$ and $Pd_{93}Pt_7$ nanowires as well as Pd nanowires, Pt nanotubes and Pd/C catalysts.[124]

An oriented attachment mechanism has been exploited for the growth of bimetallic nanowires. It was found that for bimetallic systems, the attachment of nanoparticles to form one-dimensional nanowires only takes place at certain ratios of the two metals. For example, Yang *et al*. studied the formation of PtAg worms *via* oriented attachment of small PtAg nanoparticles.[123] It was concluded that the formation of nanowires only happened when the molar ratio between Pt and Ag approached to one. When either Pt or Ag became the dominant component in the alloyed nanostructures, sphere-like or faceted nanoparticles instead of wires were obtained under the same reaction conditions. They also investigated the growth mechanism of PtAg wormlike nanowires through DFT calculation and MD simulation. Based on both experimental results and simulation calculations, it was determined

that the oriented attachment of PtAg nanoparticles to form nanowire was caused by the interplay of thermodynamic and kinetic factors.[123]

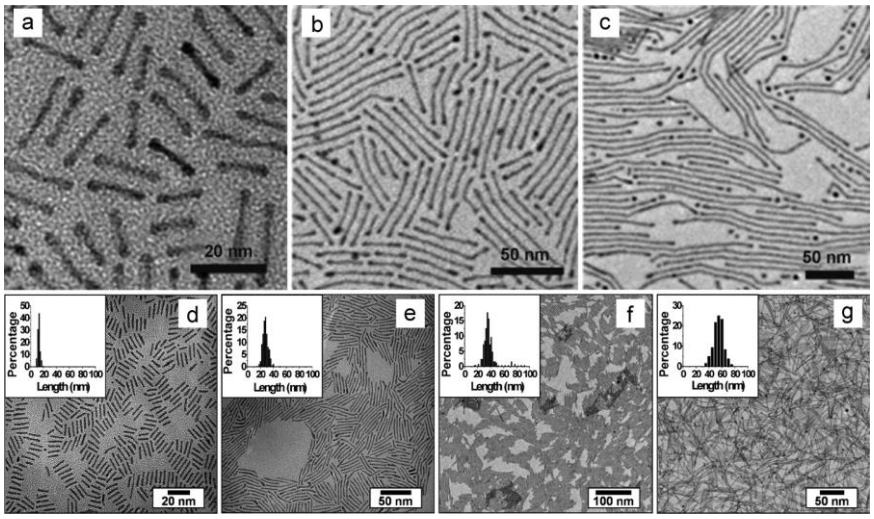

Figure 2.10 $Fe_{55}Pt_{45}$ NRs and NWs with a length of (a) 20 nm, (b) 50 nm, and (c) 200 nm.[31] CuPt nanorods with average lengths of (d) 12.6, (e) 27.8, (f) 37.1, and (g) 55.5 nm.[122]

2.4 Morphological Control of Au-Ag Bimetallic Nanostructures

Au and Ag nanostructures are excellent plasmonic materials with strong and tunable surface plasmon resonance (SPR) in visible range. For Au/Ag bimetallic nanostructures, their optical properties become more complex. This is because the optical properties of bimetallic nanoparticle may present in three possible forms: 1) the sum of the optical properties of Au and Ag components; 2) the average of the optical properties of Au and Ag components; 3) new properties. The possible outcomes are dependent on the morphologies of the Au-Ag bimetallic nanostructures.

2.4.1 Au-Ag porous/hollow bimetallic nanostructures

The Au-Ag hollow nanostructures with Au-Ag alloy walls can be obtained via GRR. These hollow structures have some advantages because their SPR peaks can be easily tuned over a very large range relative to the non-hollow nanostructures. In addition, hollow nanostructures possess lower density than their solid counterparts, which benefits some applications such as drug delivery. Therefore, various bimetallic Au-Ag hollow nanostructures have been obtained via GRR.

Xia's group has developed the GRR method to synthesize noble metal hollow structures by using noble metal precursors and Ag nanocrystals. The shapes of Au-Ag hollow structures usually remain that of Ag template. Using this approach, Au-Ag hollow structures with various morphologies can be made by simply varying the shapes of Ag template. Based on Ag nanocrystals with different shapes such as nanocubes, spherical nanoparticles, triangular plates, and nanowires, the corresponding single-walled Au-Ag alloy hollow nanostructures with similar shapes have been synthesized via GRR.[39,125] For example, with Ag nanocubes as the template, Xia et al. obtained nanoboxes and nanocages with hollow interiors by controlling the truncation degree of the Ag NCs.[126] They found a series of different morphological changes in these two cases (Figure 2.11). Specifically, for sharp cube, there were six equivalent faces and each face should have equal opportunity to start the etching reaction (Figure 2.11a). This was confirmed by the fact that the pitting site randomly appeared on one-sixth of the side facets (Figure 2.11b-c).

During the replacement reaction, Au atoms were reduced and deposited on the surface of template. Once completing the consumption of Ag, hollow boxes were obtained (Figure 2.11d). For truncated Ag NCs, they were bounded by {111} facets at each corner. These {111} facets have relatively weak interaction with PVP compared with the {100} facets (Figure 2.11e). The unprotected corner regions acted as the pitting sites for GRR (Figure 2.11f-g), and eventually hollow nanocages can be formed (Figure 2.11h).

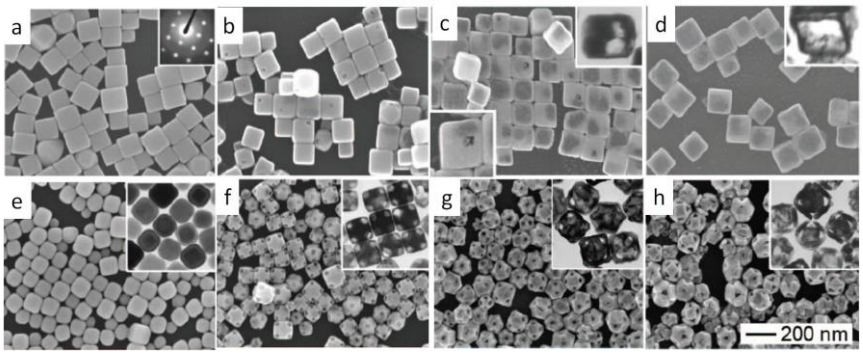

Figure 2.11 (a-d) Morphological evolution from sharp cubes to hollow nanoboxes; (e-h) morphological evolution from truncated nanocubes to hollow nanocages.[126]

Once a subsequent and conformal layer of Ag is deposited onto the surface of the single-walled hollow nanostructures, double-walled hollow nanostructures can be obtained via another round of GRR. Similarly, multiple-walled hollow nanostructures can be prepared by alternative deposition and replacement reactions.[127] In addition, hollow nanostructures with solid cores can also be obtained after GRR. For example, Sun, et al. synthesized nanorattles by using Ag-Au alloy coated with Ag as templates for GRR.[24] Song et al. obtained structures with hollow interiors on either one or both ends

of the rods via GRR by employing Ag-Au-Ag nanorods as templates and carefully changing the amount of gold precursor.[128] Double-shelled and multiple-shelled hollow nanostructures are traditionally synthesized by a consecutive reaction of galvanic replacement reaction (GRR) and electro-less plating.[127] However, Puntes et al. synthesized Au-Ag double-walled nanoboxes with an opening on one facet by one-pot reaction of $HAuCl_4$ and Ag NCs at room temperature.[129] It was found that a pitting site was formed when the GRR initiated by adding the $HAuCl_4$ solution into the reaction solution containing Ag nanocubes and surfactants. Along with the replacement reaction of Ag with Au^{3+}, both pitting site and void became large. Once the void became large enough, a Au layer was deposited on the inner surface of boxes. Afterwards, double-walled hollow boxes were formed due to the combined effect of GRR and Kirkendall effect. The pitting sites were still kept open upon the completion of the reaction. (Figure 2.12a).[129]

Generally, the production of metallic hollow nanoparticles requires high temperatures to ensure structures with smooth surfaces and distinct morphology.[130] However, Park et al. reported a modified GRR to synthesize hollow Au-Ag nanospheres at room temperature. They applied a mixture of $HAuCl_4$ and CTAB to react with Ag nanospheres in aqueous solution. In the UV-vis spectra, they found a quadrupole peak which was separated from dipole peaks when the size of Au-Ag hollow nanospheres was over 100 nm. Furthermore, when the Au content was increased by adding more Au precursor, both dipole and quadrupole peaks shifted to the red end of the

spectrum.[131]

Template nanostructures are usually synthesized prior to the GRR. Recently, Li et al. obtained octahedral Au-Ag nanoframes via a one-pot modified GRR (Figure 2.12b). In this work, they sequentially added $AgNO_3$, CuCl, and $HAuCl_4$ into solution in the present of octadecylamine. It was found that truncated Ag polyhedrons were obtained through reducing $AgNO_3$ by both CuCl and octadecylamine. Once the Ag template formed, the GRR between $HAuCl_4$ and Ag template started immediately on {111} facets of Ag polyhedrons. During the GRR, the Au atoms deposited on the {110} facets of template rather than the whole surface of Ag templates, leading to the formation of Au-Ag octahedral nanoframes.[132]

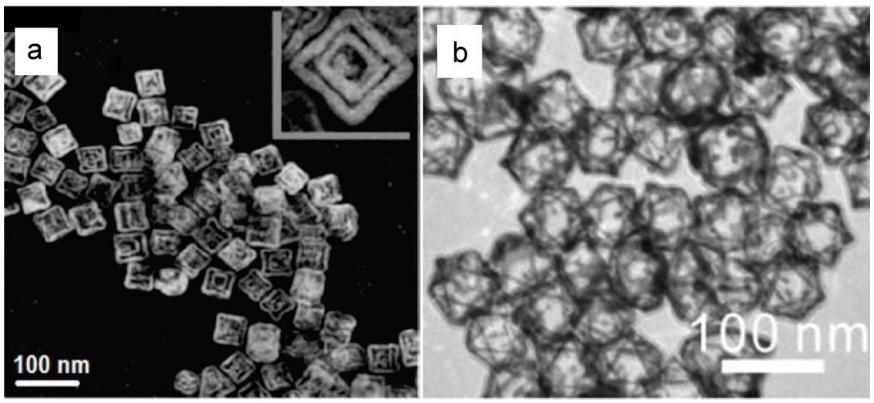

Figure 2.12 (a) Au-Ag double-walled hollow boxes;[129] (b) octahedral Au-Ag nanoframes.[132]

2.4.2 Au-Ag core-shell bimetallic nanostructures

For the study of core-shell nanostructures, the Au-Ag bimetallic system serves an excellent candidate. This is because Au and Ag have a small lattice

mismatch, the same face-centered cubic crystal (fcc) nanostructure, and similar electronic structures. Moreover, various morphologies of Au-Ag core-shell nanostructures can be obtained via seed-mediated method. The shapes of Au or Ag templates can be easily obtained, which can guide the growth of Ag shell on the surface of seeds.

2.4.2.1 Au@Ag core-shell nanorods

There has been a particular focus on the synthesis of Au@Ag bimetallic core-shell nanorods because they exhibit anisotropic optical properties. Niidome et al. synthesized rectangular Au@Ag core-shell nanorods via seed-mediated method. They studied the role of different kind of Ag precursors on the shape control by using either AgCl or $AgNO_3$ as precursor at low pH. Meanwhile, they found four extinction peaks in UV-Vis spectra when the thick Ag shell formed on Au nanorods.[133] Wang et al studied the role of seed on the shape-controlled synthesis of Au@Ag core-shell nanostructures. They used three different types of Au seeds for the deposition of Ag shell, including single-crystalline Au nanorods, multiply twinned Au nanorods and penta-twinned Au bipyramids.[134] It was found that when enough Ag precursor was introduced in the reaction, Ag atoms preferred to deposit on the side facets of single-crystalline Au nanorods to form Au@Ag nanocubes (Figure 2.13a), while preferential growth of Ag taking place at the end facets of multiply twinned Au nanorods led to the formation of long Au@Ag nanorods (Figure 2.13b). For the penta-twined bipyramids, the Ag deposited on the high-index side facets first and then at the end surface (Figure 2.13c-d). Wang and co-

workers further studied the LSPR evolution of Au@Ag bimetallic nanorods as the Ag shell grew thicker. They found that the extinction spectra of the Au@Ag core-shell nanostructure consisting of Au nanorod core and relatively thick Ag shell showed four plasmon modes -- longitudinal dipolar, transverse dipolar, and two octapolar modes (Figure 2.13e-k).[26]

Vaia et al. obtained Au-Ag core-shell nanorods with four categories of cross-sectional shape, including conformal, asymmetrical boat, rectangular and dumbbell shapes by tuning the kinetic reaction factors, such as the Ag precursor complex, the concentration of capping agent, pH value and reaction temperature.[135] Very recently, Huang and co-workers reported a facile synthetic route for controlling the growth pattern of Ag on Au cores by simply tuning the reaction kinetics via the amount of aqueous ammonia. Specifically, at slow reduction of Ag^+ ions, Au-tipped Ag nanorods were synthesized. At moderate reduction rate of Ag^+ ions by increasing the amount of ammonia, asymmetrical Ag-Au-Ag nanorods were obtained. Symmetrical Ag-Au-Ag nanorods were the final structure at high kinetic reaction rate by introducing a large amount of ammonia (Figure 2.14).[136]

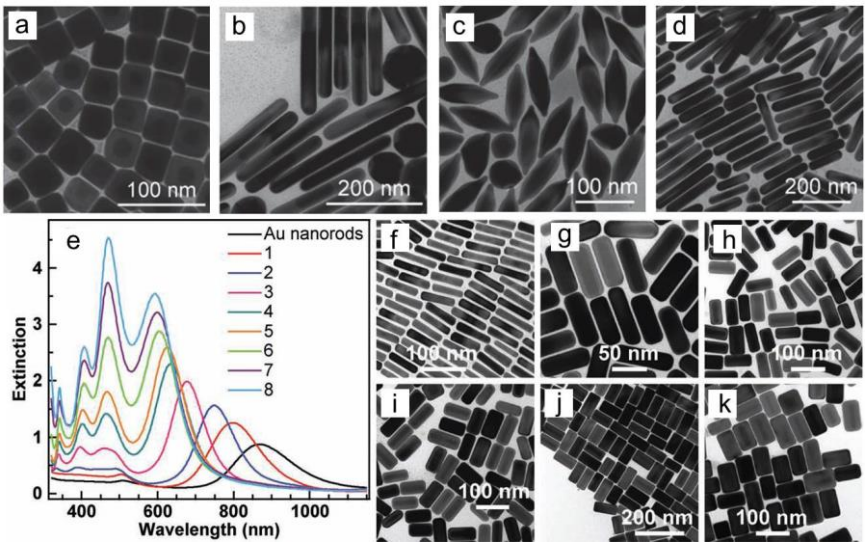

Figure 2.13 (a) Au@Ag nanocubes obtained using single-crystalline Au nanorods as seeds, (b) Au@Ag nanorods obtained using multiple twinned Au nanorods as seeds, and (c-d) Au@Ag nanostructures obtained using penta-twinned Au bipymides as seeds.[134] (e) Extinction spectra, (f) Au nanorod sample and (g-k) Au@Ag nanorods with different thickness of Ag shell, corresponding to the samples 3, 5, 6, 7, and 8 in Figure e.[26]

Core-shell nanostructures are usually obtained with seed-mediated method. The important feature of this method is that there are two distinct steps: the seed growth and the shell deposition on the surface of the seeds. To simplify the synthesis, one-pot growth method is desired. Very recently, Li and Teranishi reported a facile one-pot synthesis of Au@Ag core-shell nanorods by co-reducing Au and Ag precursors. The aspect ratio of the resultant Au@Ag nanorods can be controlled by changing the concentration of either $AgNO_3$ or PDDA. It was found that O^2/Cl^- oxidative etching pair was the key factor for formation of Au@Ag nanorods. The LSPRs of the Au@Ag nanorods with different aspect ratios were systematically studied.[137] Through tuning the specific ratio of Au@Ag nanorods, their longitudinal LSPR was red-shifted from 500 nm to 1000 nm.

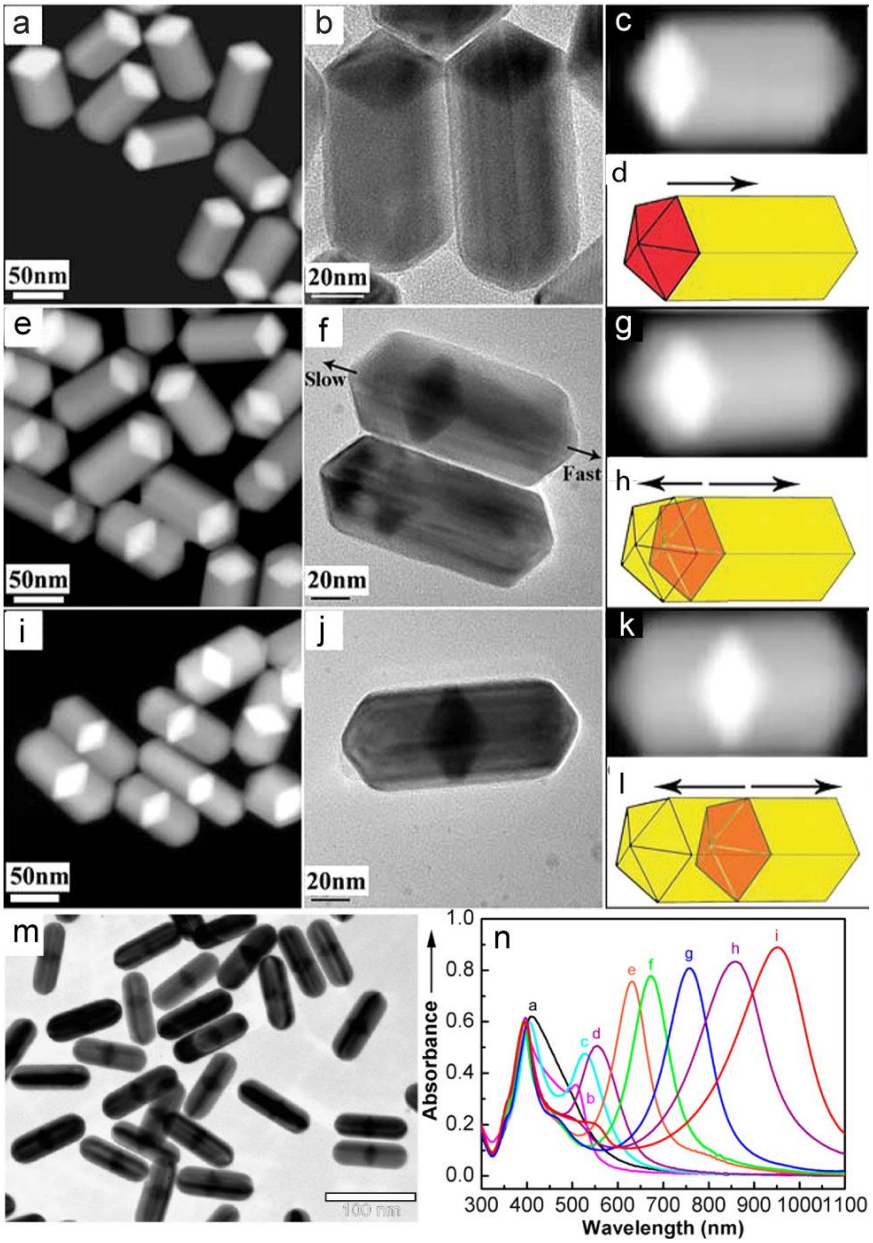

Figure 2.14 (a-d) Au-tipped Ag nanorods which were obtained by adding 15 μL aqueous ammonia, (e-h) asymmetrical Ag-Au-Ag nanorods obtained 30 μL aqueous ammonia, and (i-l) symmetrical Ag-Au-Ag nanorods obtained by adding 45 μL aqueous ammonia.[136] (m) Au@Ag core-shell nanorods synthesized in one-pot reaction, and (n) UV-vis spectra of Au@Ag nanorods with different specific ratio.[137]

2.4.2.2 Au@Ag core-shell cubes

In addition to Au@Ag nanorods, cubic core-shell nanostructures have also been well studied. Au@Ag core-shell nanocubes can be synthesized via seed-mediated approach by using different shapes of Ag nanoparticles. For example, Song et al. synthesized Au@Ag core-shell nanocubes by using Au nanospheres as seeds.[138] It was found that there is a series of shape evolution with the addition of $AgNO_3$: Au nanospheres, Au@Ag nanospheres, Au@Ag cuboctahedrons, and Au@Ag cubes. Xia's group used small Au nanospheres to grow Au@Ag nanocubes with controlled thickness of Ag shells.[139] The main LSPR peaks of Au@Ag were red-shifted with the thickness of Ag shells increased from 12 to 20 nm. By using three different shapes of Au seeds including rhombic dodecahedra, cubes, and octahedra, Tang et al. obtained Au@Ag core-shell nanocubes via a modified seed-mediated method (Figure 15a-c).[140] They used Br^- ions to intervene the growth of Ag shell. It was found that Br^- ions facilitated the formation of cubic Au@Ag core-shell nanostructures even though the Au seeds were bonded with different facets. It was also found that the LSPR of these Au@Ag core-shell nanocubes depended on the core-shape and size (Figure 2.15d).

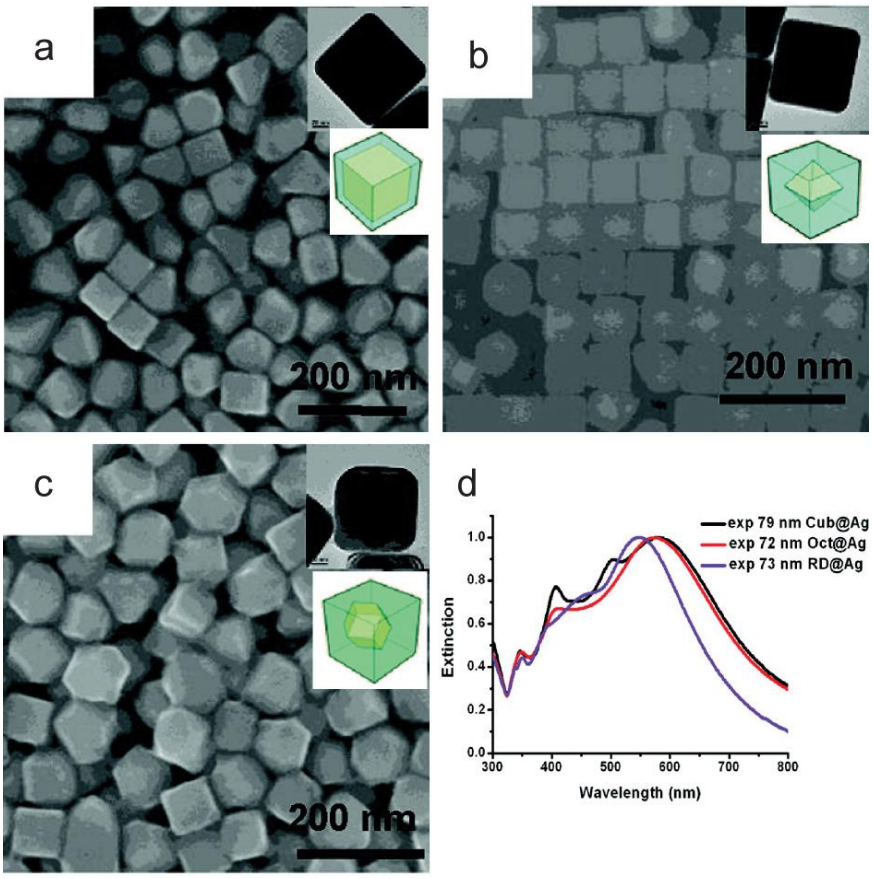

Figure 2.15 Au@Ag nanocubes obtained using different Au seeds: (a) cubes, (b) octahedral, and (c) rhombic dodecahedra; (d) Extinction spectra of the Au@Ag nanocubes shown in a-b.[140]

2.4.2.3 Au@Ag core-shell structures with other shapes

Au@Ag core-shell nanostructures with other shapes such as prisms, hexagonal plates and polyhedral nanocrystals have also been obtained. Mirkin et al. synthesized Au@Ag core-shell prisms by using plasmon-mediated synthetic strategies (Figure 2.16a-b).[141] In this work, the mixture of Au and Ag nanoparticles was irradiated with 520-nm light. The roles of Au and Ag nanoparticles were as seed to induce and label the Ag growth and as feedstock for the Ag^{+} ions, respectively. It was the Au seeds rather than extinction

wavelength that determined the average thickness of these Au@Ag nanoprisms. Based on the SPR of the seeds, a light with an appropriate excitation wavelength was used to start the Ag coating. In a later study of same group, Au@Ag triangular bifrustums were synthesized via a seed-mediated method in aqueous solution (Figure 2.16c). It was found that core-shell nanostructures exhibited tunable dipole and quadrupole SPR peaks which were ascribed to the geometry of these core-shell triangular bifrustums (Figure 2.16d).[142]

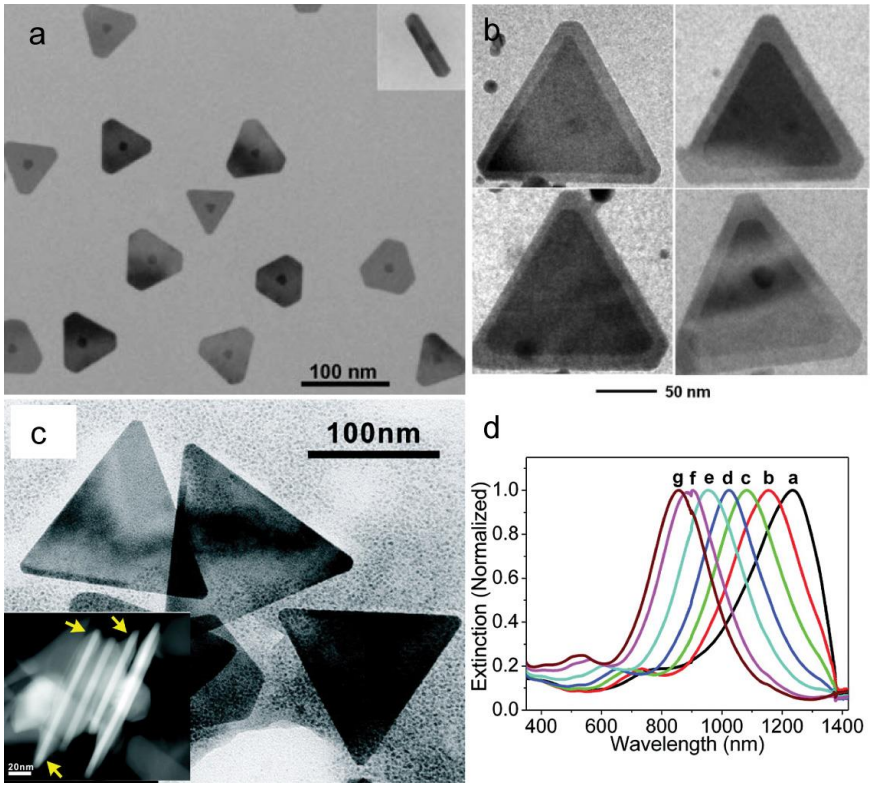

Figure 2.16 Au@Ag core-shell prisms obtained using different Au seeds: (a) nanoparticles and (b) nanoprisms.[141] (c-d) Au@Ag triangular bifrustums and their extinction spectra.[142]

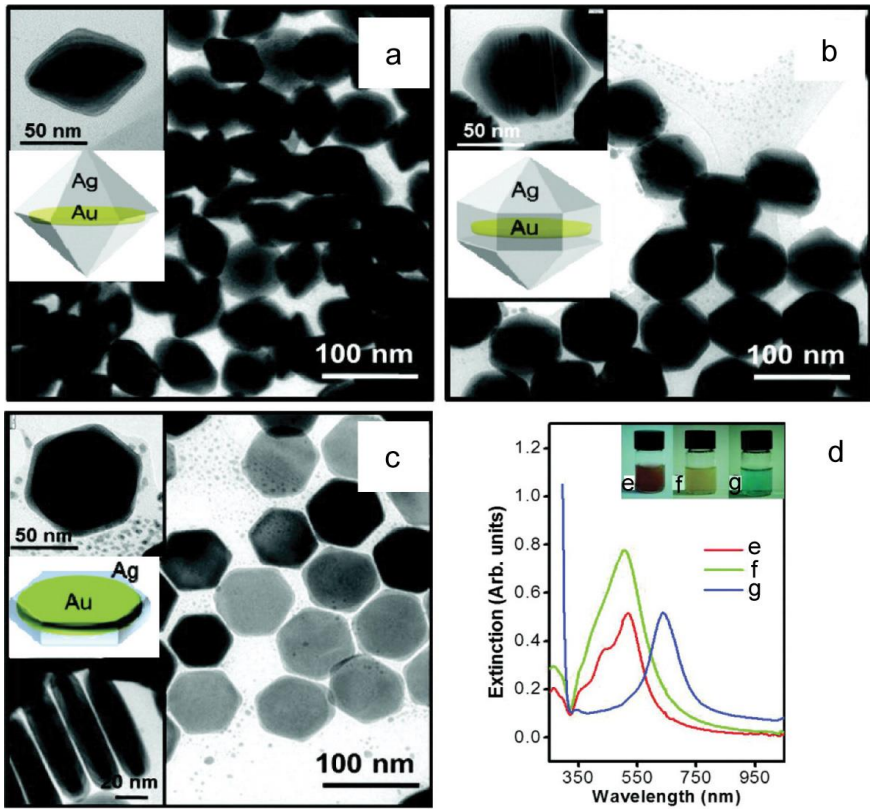

Figure 2.17 (a) Au@Ag core-shell dodecahedra, (b) Au@Ag core-shell elongated polyhedra and (c) Au@Ag core-shell hexagon nanoplates; (d) Extinction spectra of Au@Ag core-shell nanostructures shown in Figure e-g.[143]

Tsuji et al. also obtained a series Au@Ag core-shell nanostructures via seed-mediated method in N,N-dimethylformamide solution in presence of PVP.[144] The Au@Ag core-shell nanostructures were Au@Ag triangular plates, hexagonal plates, octahedra, and decahedra when Au nanocrystals with the corresponding shapes are as seeds, respectively. It was found that Cl^- ions played an important role on facet selective growth and oxidative etching of specific facets. In a later report, through the same method, Tsuji and co-workers synthesized Au@Ag icosahedra using Au icosahedra as seeds.[145] Similarly, with the assistance of another halide as the shape-directing agent, Park et al. synthesized Au@Ag core-shell dodecahedra and elongated polyhedra by using Au nanodisk as seeds in the presence of I^- ions (Figure 2.17a-b).[143] When I^- ions were absent, a homogeneous Ag shell grew on the Au nanodisk to

form hexagon Au@Ag nanoplate (Figure 2.17c). The UV-Vis spectra of these resulting Au@Ag core-shell nanostructures showed different LSPR properties due to the different morphologies (Figure 2.17d).

2.4.3 Au-Ag particle-on-particle bimetallic nanostructures

Due to the small interfacial surface energy between Au and Ag, core−shell structure is the most favorable type when Ag deposits on the surface of Au seeds. However, by tuning some reaction conditions, Au-Ag particle-on-particle structures can also be formed via the SK or VW growth mode. For example, Xu et al. reported Au-Ag heterodimers obtained by confining limited active site area of Au seed with Ag^+ ions at water-oil interface (Figure 2.18a-b).[146] This approach changed the Ag growth mode from FM mode to VW mode. Recently, Chen et al. tuned Au-Ag bimetallic nanostructures from concentric core-shell structure to dimer by changing the incubation conditions of Au seed in ligand solution.[147] The resulting Au-Ag bimetallic nanostructures were concentric core-shell, eccentric core-shell, acorn, and dimers after Ag deposition (Figure 2.18d-g). The UV-vis spectra showed three extinction peaks for eccentric, acorn and dimer nanostructures, attributing to the transverse absorption of Ag and Au and the longitudinal absorption of Au-Ag bimetallic nanostructures, respectively (Figure 2.18c).

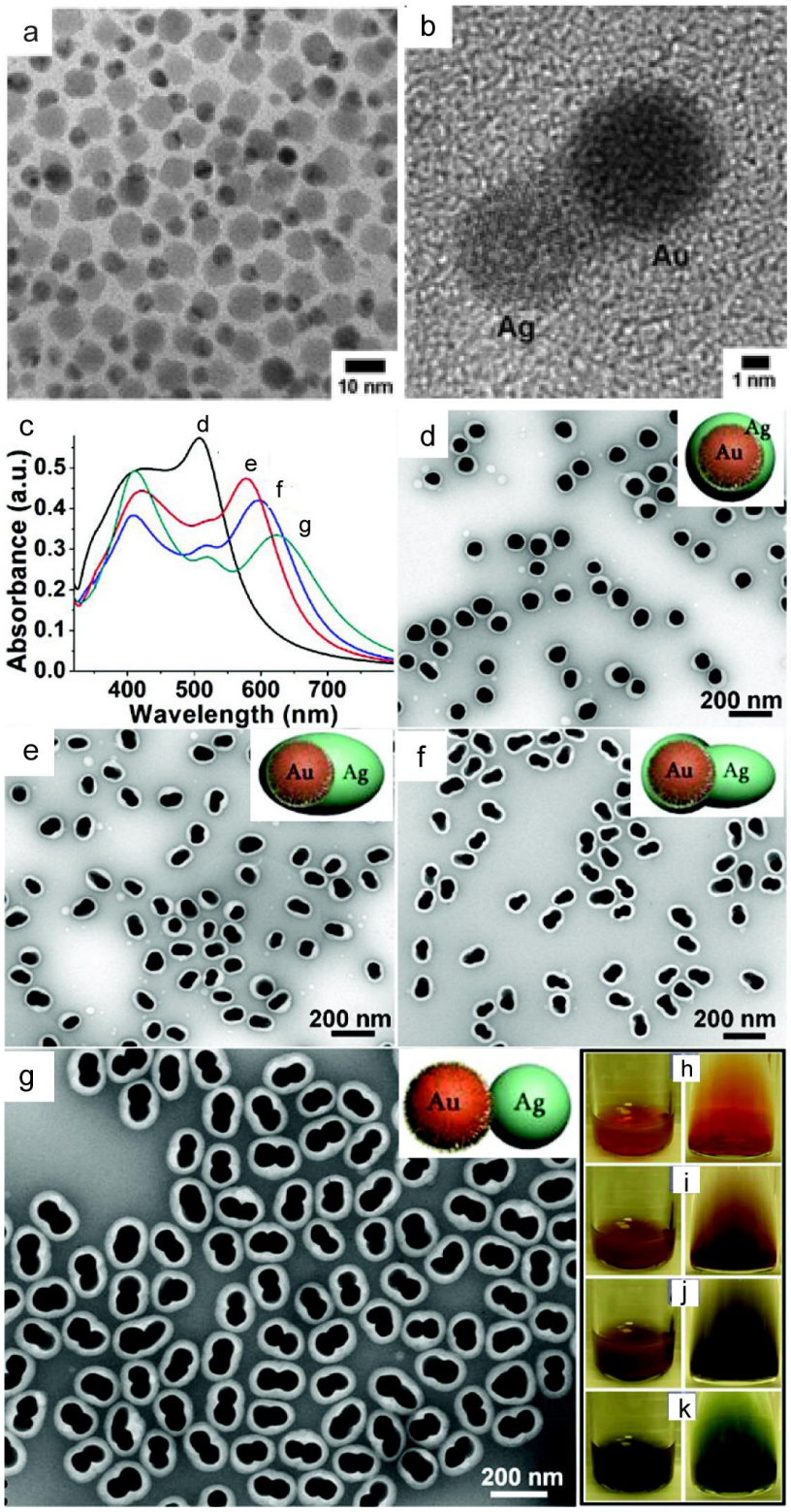

Figure 2.18 (a-b) Au-Ag heterodimers.[146] (c) UV-vis of the Au-Ag bimetallic structures in (d) concentric core-shell, (e) eccentric core-shell, (f) acorn, and (g) dimers.[147]

Chapter 3. Experimental Section

3.1 Chemicals and materials

All reagents were used as received without further purification. The information of the chemicals and materials used in this thesis is given in Table 3.1.

Table 3.1 Chemicals and materials

Chemicals	Purity	Supplier
Deionized (DI) water	18.2 MΩ·cm	
Iso-propanol	Reagent grade	Merck
Ethanol	Reagent grade	Fisher
Methanol	analysis grade	Merck
Ethylene glycol (EG)	Baker analysis agent	J.B. Baker
Ethylene glycol (EG)	99.0%	Sigma-Aldrich
Silver nitrate ($AgNO_3$)	99.0%	Sigma-Aldrich
Potassium tetrachloroplatinate (K_2PtCl_4)	98.0%	Aldrich
Gold(III) chloride trihydrate	99.9%	Alfa Aesar

($HAuCl_4 \cdot 3H_2O$)		
Palladium (II) chloride ($PdCl_2$)	99.9%	Alfa Aesar
Polyvinylpyrrolidone (PVP, Mw≈55,000)		Aldrich
Poly(diallyldimethylammonium chloride) (PDDA, Mw = 200000-350000)	20 wt%	Sigma-Aldrich
Cetyl-trimethylammonium bromide (CTAB)	99.0%	Sigma-Aldrich
Cetyl-trimethylammonium chloride (CTAC)	≥98.0%	Sigma-Aldrich
L-ascorbic acid (AA)	99.0%	Sigma-Aldrich
Hydrochloric acid (HCl)	37.5%	Fisher
Hydrochloric acid (HCl)	37%	Merck
Perchloric acid ($HClO_4$)	70.0%	Sigma-Aldrich
Potassium hydroxide (KOH)	90.0%	Sigma-Aldrich
Sodium hydroxide (NaOH)	≥98.0%	Merck
Sodium chloride (NaCl)	99.5%	Sigma-Aldrich

Iron(III) nitrate nonahydrate ($Fe(NO_3)_3$ $9H_2O$,)	98.0%	Alfa Aesar
Nafion	5% in a mixture of lower aliphatic alcohols and water	Sigma-Aldrich
4-Aminothiophenol (ATP)	97.0%	Aldrich

3.2 Solution preparation

5 mM K_2PtCl_4 solution was prepared and aged at least for 24 h before use. 10 mM H_2PdCl_4 solution was prepared by dissolving $PdCl_2$ in 20 mM HCl at 100 ℃. Other solutions were prepared by dissolving chemicals into specific solvent before use.

3.3 Synthesis of monometallic nanostructures templates

3.3.1 Synthesis of Ag nanocubes (NCs)

Silver NCs (50-70 nm in edge length) were synthesized by a modified polyol process[55]. In a typical synthesis, 10 ml EG was added into a 50 mL flask and heated under magnetic stirring at 140 ℃ for 1 hour. HCl (2.1 mL, 3.016 mM in EG) was quickly injected into the heated EG using pipette and continued heating for 10 minutes. $AgNO_3$ (6mL, 94 mM in EG) and PVP (6mL, 147 mM in EG) were simultaneously injected into the reaction mixture

using a two-channel syringe pump at a rate of 0.6 mL/min. This reaction mixture was allowed to react for around 24-36 hours at a temperature of 140 ℃ with constant stirring. Subsequently, the reaction was removed from the oil bath and quenched in an ice-water bath. The product was mixed with equal-volume acetone and centrifuged, following by washing with water for five times to remove the excess PVP. The resultant NCs were dispersed in 20 mL of water in a reaction vial that was wrapped with aluminum foil and stored on a dark cabinet for further use.

3.3.2 Synthesis of gold bipyramid seeds

In a typical synthesis of gold bipyramids,[148] 0.2 mL PDDA and 10 ml EG were added into a 20 mL vial and mixed under magnetic stirring at room temperature for 5 mins. To this solution, 18.8 μL of 0.5 M $HAuCl_4$, 10 μL of 500 mM $AgNO_3$, 62.5 μL of 10 mM H_2PdCl_4, and 430 μL of deionized (DI) water were added subsequently. After 10 mins, this mixture was capped tightly and heated in an oil bath at 140 ℃ for 12 hours under constant stirring. The resulting Au BPs were washed with acetone and DI water, respectively.

3.4 Synthesis of hollow and porous bimetallic nanostructures via GRR

3.4.1 Synthesis of Pt/Ag heterodimers

In a typical synthesis of Pt/Ag heterodimers, 0.1 mL dispersion of Ag nanocubes (the concentration of Ag is 8.0 mM based on ICP-MS

measurement) was added to 4.9 mL of ultrapure deionized water. 0.23 mL of 10 mM HCl was added to the reaction mixture (molar ratio HCl:Ag = 2.75:1). The vial was then heated in an oil bath at 100 ℃ for 5 minutes. 0.5 mL of 5 mM K_2PtCl_4 solution was injected into the reaction mixture using a syringe pump at a rate of 1 mL/min. The reaction mixture was continually stirred and heated at 100 ℃ until no further color change (about 5 min). The reaction mixture was centrifuged and washed using saturated NaCl, 50 mM $Fe(NO_3)_3$, and water to remove AgCl, Ag, and residual ions, respectively. The final product was dispersed in 1.0 mL of DI water.

3.4.2 Synthesis of Au/Ag heterodimers

For Au/Ag dimers, the procedure was identical to that of Pt/Ag dimers (described in section 3.2.3.1), except that 0.4 mL of 0.5 mM $HAuCl_4$ solution was injected into the dispersion of Ag NCs in the presence of HCl.

3.4.3 Synthesis of Pt/Ag nanoboxes

A synthetic approach similar to Pt/Ag dimers was followed for Pt/Ag hollow nanoboxes, except that 0.5 ml PVP solution (100 mM) was added to the mixture of HCl and Ag NCs prior to the injection of K_2PtCl_4 solution.

3.4.4 Synthesis of Au/Pt/Ag structures

1.0 mL of Pt/Ag heterodimers (without washing with $Fe(NO_3)_3$ solution) was dispersed in 4.0 mL DI H_2O. The vial was then heated at 100 ℃ for 5 minutes. 0.1 mL of $HAuCl_4$ solution (0.5 mM) was injected into the reaction

mixture using a syringe pump at a rate of 0.2 mL/min. The reaction mixture was continually stirred and heated at 100 ℃ for another 5 mins. After washing, the product was dispersed in 0.5 mL DI water.

3.4.5 Synthesis of Pt/Ag popcorn-shaped nanostructures

0.5 mL of 10 mM HCl was mixed with 0.5 mL of 5 mM K_2PtCl_4 for 2 hours. 0.5 ml of 100 mM PVP was added to the dispersion of Ag NCs and the solution was heated for 5 minutes in the oil bath before the injection of the solution containing K_2PtCl_4 and HCl at a rate of 2 mL/min. The reaction mixture was centrifuged and washed using saturated NaCl, 50 mM $Fe(NO_3)_3$, and water to remove AgCl, Ag, and residual ions, respectively. The final product was dispersed in 1.0 mL of DI water.

3.5 Synthesis of bimetallic AuAg@ATP@AuAg sandwiched structures nanostructures

3.5.1 Synthesis of Au/Ag hollow boxes

Au/Ag hollow boxes were synthesized via galvanic replacement reaction.[130] Typically, 0.5 mL aqueous dispersion of Ag nanocubes (the concentration of Ag is 13.8 mM based on ICP-MS measurement) was added to 14.5 mL of 20 mM PVP solution in a 50 mL flask. The flask was then heated in an oil bath at 100 ℃ for 10 minutes. 2.3 mL of 0.5 mM $HAuCl_4$ solution was injected into the reaction mixture using a syringe pump at a rate of 0.3 mL/min. The reaction mixture was continually stirred and heated at 100 ℃ for

another 10 mins. The reaction was then stopped and cooled down to room temperature. The reaction solution was transferred into 20 mL vial and its volume was topped up to 15 mL by adding DI H_2O.

3.5.2 Preparation of Au/Ag hollow boxes functionalized with ATP (AuAg@ATP)

98.4 mg CTAB and 118 mg PVP were added to the 15 mL AuAg hollow boxes solution obtained in the previous step. The final concentrations of PVP and CTAB in the AuAg hollow boxes solution were 1wt% and 18 mM, respectively. Thereafter, 0.6 mL of 10 mM 4-ATP in ethanol was added into the AuAg hollow boxes solution. The mixture was then incubated overnight at room temperature.

3.5.3 Synthesis of AuAg@ATP@Ag sandwiched structures

After incubation, 5 mL of AuAg@ATP solution was heated at 70 ℃ for 20 minutes with stirring. Specific volumes of 4 mM $AgNO_3$, 0.1 M AA, and 0.1 M NaOH were added in sequence using pipette at a ratio of 1:2:0.8 (v:v:v). The resulting mixture was kept at 70 ℃ for 20 minutes under moderate stirring. The product was then washed 3 times with DI H_2O and 3 times with ethanol, respectively. The washed product was re-dispersed in 2.55 ml of 20 mM PVP solution.

3.5.4 Synthesis of AuAg@ATP@AuAg sandwiched structures

For the synthesis of the AuAg@ATP@AuAg sandwiched structures, another round of modified GRR was carried out as follows. 2.55 mL of AuAg@ATP@Ag solution with 20 mM PVP was transferred to a 20 mL flask. To this solution, 0.25 mL of 10 mM HCl was added. After the mixture was heated with stirring at 100 ℃ for 5 min, specific volume of 0.2 mM $HAuCl_4$ was injected at a rate of 0.2 ml/min. The resultant mixture was heated for another 5 min before it was stopped and cooled down to room temperature. The final product was washed with saturated NaCl once and with DI H_2O for 5 times before it was re-dispersed in water.

3.6 Synthesis of Au@Ag bimetallic nanorods

3.6.1 Synthesis of Au@Ag bimetallic nanorods with flat tips

The Au@Ag bimetallic nanorods with flat {110} end facets were obtained as follows: 25 μL of as-grown Au BPs were added to 2.5 mL solution containing 1wt% PVP and 18mM CTAB. The resulting mixture was heated in an oil bath with stirring at 70℃ for 20 minutes. Thereafter, 4 mM $AgNO_3$, 0.1 M AA and 0.1 M NaOH were added by pipetting sequentially at a ratio of 1:2:2 (v:v:v), the reaction was allowed to proceed at the same temperature for another 20 minutes. The measured pH was 4.9. The final product was then washed 5 times with DI water and stored in 0.1ml DI water.

3.6.2 Synthesis of Au@Ag bimetallic nanorods with sharp tips

For the synthesis of Au@Ag bimetallic nanorods with sharp tips, the procedure was the same as described in section 3.2.5.1, except that CTAB was replaced with CTAC at the same concentration.

3.6.3 Synthesis of Au@Ag bimetallic nanorods with dumbbelled-shape

For the synthesis of Au@Ag nanorods with dumbbell-shape, a similar synthetic approach was conducted, except that 0.1 mL of 0.1 M AA and 0.21 mL of 0.1 M NaOH were added with different amounts of 4 mM $AgNO_3$ to maintain the pH at 10.

3.7 Electrochemical analysis

Electrochemical measurements for the Pt/Ag nanoparticles were carried out by cyclic voltammetry using a potentiostat (BioLogic Science Instruments, VSP Modular 5 Channels). The cell was assembled as a three-electrode setup consisting of a glass carbon electrode (GCE) as the working electrode, Pt wire as the counter electrode, and saturated calomel electrode as the reference electrode. Pt/Ag catalyst ink was prepared by dispersing the nanoparticles into 200 μL of 20% iso-propanol in water solution. From ICP-MS measurements, the concentrations of Pt for Pt/Ag popcorns, dimers, and hollow nanoboxes were 960 ppm, 609 ppm, 778 ppm, respectively. The molar ratios of Pt to Ag for the three samples are listed in Table 3-2. Specific volume of these catalysts was then dropped on the GC electrode (3 mm diameter, 0.071 cm^2).

Commercial E-Tek Pt/C catalyst (Pt loading: 20 wt%) was used as the reference. For all catalysts, the loading of Pt was 5 μg. After drying, 5 μL of 0.1 wt% nafion solution (diluted from 5% Nafion with ethanol) was dropped onto the electrode and dried in air. Electrochemical surface area (ECSA) for the nanoparticles was measured in 1 M $HClO_4$ solution. Methanol oxidation catalytic activity of the nanoparticles was measured in a solution containing 1 M KOH and 1 M CH_3OH. The sweep rate of all measurements was 50 mVs^{-1}. Chronoamperometry experiments were conducted by monitoring current at the potential constant at -0.4 V versus SCE in a solution containing 1 M KOH and 1 M CH_3OH.

Table 3.2 The molar ratio of Pt to Ag of popcorns, dimers and hollow boxes measured by ICP-MS

	Pt/Ag ratio (ICP-MS)
Popcorn	5.48
Dimers	3.91
Hollow boxes	5.33

3.8 Raman measurement

The samples were measured using two Raman systems with 514.5 nm and 637 nm laser light source, respectively. When a 514.5 nm Argon ion laser operating at room temperature was applied as an excitation source, Raman

spectra were collected from with a micro-Raman spectroscope (Renishaw 2000) equipped with an integral microscope (Olympus BH2 microscope). Measurement was established via 20× objective in the backscattering configuration. The laser power used was kept constant around 10 mW. The incident polarized laser light and scattering propagation were perpendicular to the sample surface. Before measurement, the system was calibrated with Si (100) peak at 520 cm^{-1} as reference. Measurement of each liquid sample was acquired with 4 times accumulation, while each round was set to 30 seconds. When a stabilized 637 nm laser diode was the excitation light source, the Raman spectra were acquired from a Raman spectrometer equipped with equipped with a high sensitivity deep cooled CCD detector (shamrock-163). The laser power used was about 150 mW. The resolution of the Raman instrument was 4 cm^{-1}.

3.9 Other Characterization Methods

3.9.1 Ultraviolet-visible spectrophotometer (UV-Vis)

UV-vis spectra were recorded using a Shimadzu UV-1601 spectrometer with plastic cuvettes of 1 cm path length at room temperature.

3.9.2 X-ray diffraction (XRD)

The XRD spectra were acquired using a Bruker D8 Advance diffractometer equipped with a Cu KR radiation source (λ =1.5418 Å) from samples deposited onto glass substrates.

3.9.3 X-ray photoelectron spectroscopy (XPS)

The XPS spectra were obtained using AXIS HIS (Kratos Analytical Ltd., U.K.) with an Al-Kα X-ray source (1486.71 eV protons), operated at 15 kV and 10 mA.

3.9.4 Inductively coupled plasma mass spectrometry (ICP-MS)

The atomic concentrations of samples were obtained based on ICP-MS measurements on an Agilent 7500A. Samples were prepared by dissolving the nanoparticles using fresh aqua regia. The resultant solution was diluted using DI water.

3.9.5 Number concentration of nanoparticles

For SERS enhancement comparison among samples, the concentrations of all samples were fixed at same value in order to make sure the amount of probe molecules was similar. The concentrations of dispersed nanoparticles were confirmed by Nanoparticle Tracking Analysis (NTA, Nanosight LM10-HS with laser output of 60mW at 405 nm). NTA utilizes the both light scattering and Brownian motion to obtain particle size distributions of particles in liquid. Estimation of the concentration of the particles is based on the assumed scattering volume calculated from the dimensions of the field of view (at a given magnification) and the depth of the laser beam. By counting the number of particles tracked at any instant, the average concentration per scattering volume can be estimated.

3.9.6 Scanning electron microscopy (SEM)

Scanning electron microscopy (SEM) images and scanning transmission electron microscopy (STEM) images were taken using a JEOL JSM-6700F field emission scanning electron microscope (FESEM) operating at 10kV and 25kV, respectively. For the SEM measurement, the resultant nanostructures solutions were dropped on clean silicon substrates. For the STEM samples, diluted samples were dropped on TEM copper grids.

3.9.7 Transmission electron microscopy (TEM)

Transmission electron microscopy (TEM) images, high-resolution TEM (HRTEM) images, and energy dispersive X-ray spectroscopy (EDX) spectra were acquired using JEOL 2010 and JEOL 2100F operating at 200 kV. The TEM copper grids were prepared by dropping diluted aqueous solutions of the synthesized nanoparticles.

Chapter 4. Tailoring Galvanic Replacement Reaction for the Preparation of Pt/Ag Bimetallic Hollow Nanostructures with Controlled Number of Voids

4.1 Introduction

Galvanic replacement reaction (GRR) has emerged as a powerful synthetic approach for converting solid metal nanostructures into hollow ones that are advantageous in optical and catalytic properties[149-152]. Typically, GRR-based synthesis involves the use of metal nanostructures as sacrificial templates to react with ions of a more noble metal. Due to the difference in electrode potentials of the two metals, the nanostructured metal templates will be dissolved and the more noble metal ions will be reduced to elemental form, which subsequently deposits onto the surface of the templates[153-155]. Depending on a number of factors such as similarity in crystal structures, degree of lattice mismatch, and difference in metallic bonding strengths, a conformal or a non-conformal growth of the second metal may take place on the surface of the template to form a shell while the first metal is continuously consumed from the core. In the end, a structure with a hollow interior and a shell composed of either just the second metal or the alloy of both metals can be formed.

To date, a wide variety of hollow nanostructures including spherical nanoshells[156], cubic nanoboxes[157,158], nanocages[153,159], hollow nanorods[154],

nanotubes[160], nano-rattles[161], nanoframes[162], and nano-dendrites[163,164] composed of Au,[153,165] Pd,[166-168] and/or Pt[53,168,169] have been prepared *via* GRR using nanotemplates of Ag,[153,165] Cu,[167,168] or more reactive metals (*e.g.* Zn or Mg[169,170]). These hollow nanostructures have found applications in areas including biomedical imaging[171], photothermal cancer treatment[150,172], drug delivery[173], surface enhanced Raman scattering[174,175], and electrochemical catalysis[176-178]. In most cases, the shape of the hollow nanostructures obtained *via* GRR resembles that of the sacrificial templates. For instances, when Ag nanocubes (NCs) are used as the template to react with $HAuCl_4$, hollow Au/Ag nanoboxes can be prepared[153]. Novel structures such as nanobowls[179] or multiple-walled nanoshells[161] have also been synthesized, although complex templates are necessary for generating such structures. Here we show that by tuning the GRR between Ag NCs and K_2PtCl_4, Pt/Ag bimetallic hollow nanostructures with distinct shapes and tailored number of void zones can be readily obtained. Figure 4.1 illustrates the hollow nanostructures and their corresponding reaction conditions (see experimental methods in Chapter 3.4 for details). In the first case, both HCl and PVP are introduced into the dispersion of Ag NCs. After injecting K_2PtCl_4 solution, Pt/Ag nanoboxes with smooth and continuous walls are obtained (Figure 4.1a). However, if only HCl is added into the dispersion of Ag NCs before the injection of K_2PtCl_4, the reaction gives Pt/Ag heterodimers, a structure consisting of a hollow box with an attached particle (Figure 4.1b). At higher concentration of HCl, the number of attached particles on each hollow nanobox increases, leading to the formation of multimeric nanostructures (Figure 4.1c). If HCl is mixed with

K_2PtCl_4 solution before it is reacted with Ag NCs, Pt/Ag hollow nanostructures consisting of multiple attached particles, namely popcorn-shaped particles, are formed (Figure 4.1d). Subsequent washing with NaCl and $Fe(NO_3)_3$ solutions can further convert the attached solid particles into hollow ones. Compared with nanoboxes with single void interior, the dimeric, multimeric, and popcorn-shaped nanostructures consisting of two or more hollow domains within one particle show much-increased surface area and should be beneficial to their catalytic applications.

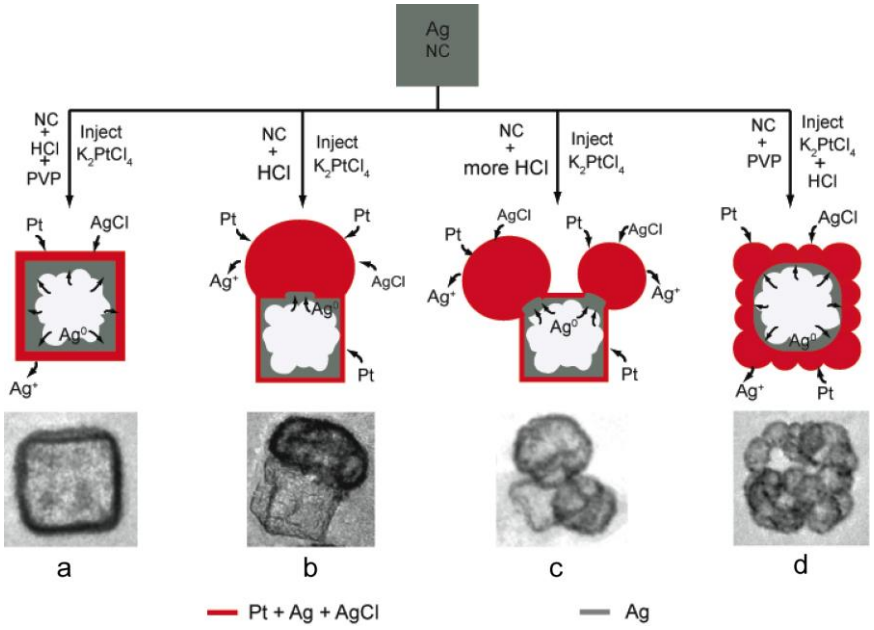

Figure 4.1 Illustration of the formation of Pt/Ag (a) nanobox, (b) heterodimer, (c) multimer, and (d) popcorn-shaped nanoparticle from the GRR between Ag NCs and K_2PtCl_4 in the presence of HCl.

4.2 Results and discussion

4.2.1 Pt/Ag hollow boxes

Ag nanocubes with average length of 70 nm (Figure 4.2) were selected as the sacrificial templates due to its standard reduction potential of the $PtCl_4^{2-}$/Pt pair (0.74V vs. SHE) is higher than that of Ag^+/AgCl (0.222 V vs. SHE). Figure 4.3a shows the Pt/Ag nanoboxes with smooth and continuous walls prepared by adding 0.23 mL HCl (10 mM) and 0.5 mL PVP (100 mM) to the dispersion of 70-nm Ag NCs, followed by the injection of 0.5 mL K_2PtCl_4 (5 mM) at 100 ℃. The nanoboxes display a well-defined cubic shape with an average edge length of 75 nm and a wall thickness of ~10 nm. High-resolution transmission electron microscopy (HRTEM) image of the nanoboxes reveals porous but single-crystalline walls with lattice fringes corresponding to the (100) plane of Pt/Ag alloy (Figure 4.3c). The GRR between Ag nanostructures and Pt ions has been widely investigated for the preparation of Pt/Ag bimetallic structures, although hollow nanoboxes with continuous and smooth walls have been scarcely observed[155,176,180-182]. For instance, Xia *et al*. employed Ag NCs to react with Na_2PtCl_4 to form nanoboxes[166]. In contrast to Au/Ag system, where the reaction between Ag NCs and $HAuCl_4$ gives Au/Ag alloy nanoboxes with smooth surface[153], the Pt/Ag hollow nanostructures in their work displayed a rough surface decorated with Pt nanoparticles. The difficulty in forming Pt/Ag hollow nanostructures with smooth walls has been attributed to a number of reasons, including 1) the large lattice mismatch between Pt and Ag (4.3%, for Au and Ag it is 0.2%); 2) the difficulty in

forming alloys between Pt and Ag -- it has been shown that even melted together, Pt and Ag would not be able to form alloy with Pt>5%[166]; and 3) the slower reaction rate between Pt ions and Ag atoms than that for the reaction between Au ions and Ag[183]. Interestingly, in our work, by adding HCl and PVP to the dispersion of Ag NCs before they were reacted with K_2PtCl_4, hollow Pt/Ag nanoboxes with smooth walls were readily obtained.

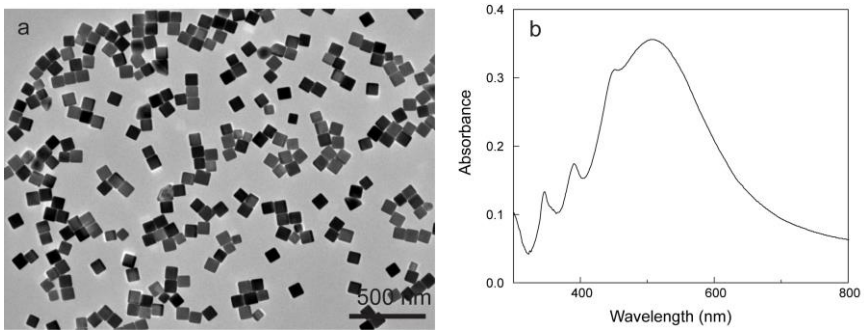

Figure 4.2 (a) TEM of Ag nanocube templates, (b) UV-Vis spectrum.

The reaction between Ag and K_2PtCl_4 is as follows: $2Ag + K_2PtCl_4 \rightarrow Pt + 2AgCl + 2KCl$. With the reduction of K_2PtCl_4, Pt is formed and deposited onto the surface of the Ag templates. As a by-product of the reaction, AgCl is also generated. As mentioned earlier, due to the low solubility of AgCl in water (1.33×10^{-5} mol/L at 25 ℃)[184], AgCl may precipitate out and interfere unfavorably with the deposition of Pt. To avoid the precipitation of AgCl, one may raise the reaction temperature to increase the solubility of AgCl (10 times higher at 100 ℃). This method has proven to be effective for the reaction between $HAuCl_4$ and Ag nanostructures to form hollow Au/Ag nanostructures with smooth walls[153]. Another approach is to add chemicals that react with

AgCl to form soluble species. For example, Xu *et al*. used highly concentrated HCl (3 M) in the GRR between H_2PtCl_6 and porous Ag so that AgCl can be converted to soluble complex $AgCl_2^-$[155]. However, when HCl at low concentration (0.44 mM in our work) was used during the galvanic replacement reaction, one would expect that the precipitation of AgCl will occur at even lower concentration of Ag^+; and it is counterintuitive to obtain nanoboxes with smooth and continuous walls. Therefore, in our case where both HCl and PVP were added to the dispersion of Ag NCs, the deposition of AgCl might take place evenly on the surface of Ag NCs. The presence of AgCl on the whole surface of the NCs facilitated the growth of a uniform layer of Pt. Although the reason is not clear yet, the use of AgCl for the growth of uniform Pt layer on Ag has been previously reported. For instance, Ye *et al*.[185] found that while the GRR between Ag nanowires and H_2PtCl_6 led to the formation of aggregated Pt nanoparticles on Ag surface, hetero-epitaxial growth of a continuous Pt layer was achieved if Ag nanowires were treated with $FeCl_3$ solution to form a AgCl layer before the GRR. In another work, Lee *et al*. also employed AgCl nanocubes as removable templates for the growth of Pt which eventually evolved into smooth Pt hollow nanoboxes[157]. In our work, the existence of AgCl in the walls of the resultant nanoboxes was confirmed from energy dispersive X-ray spectroscopy (EDX). EDX line profile of the Pt/Ag nanoboxes shows that, in addition to Pt and Ag, strong signal from Cl is also revealed (Figure 4.3d). Since the samples were washing carefully before the EDX measurements, the existence of Cl cannot be solely attributed to surface-adsorbed species. Therefore, appreciable amount of AgCl

is expected in the walls of the hollow nanoboxes. It should be noted that when the hollow nanoboxes were washed by saturated NaCl and $Fe(NO_3)_3$ solutions, the wall thickness decreased because of the removal of AgCl and Ag, respectively (Figure 4.3b). This is because saturated NaCl solution can form soluble complex with AgCl[153], while $Fe(NO_3)_3$ oxidizes Ag[162]. In addition to the effect of AgCl, suitable reaction kinetics may also contribute to the deposition of smooth Pt layer on the Ag NCs. Recently, El-Sayed *et al*. reported that Pt/Ag nanoboxes with porous continuous walls can be synthesized based on the GRR between Ag NCs and K_2PtCl_4[183]. In their study, K_2PtCl_4 at high concentration was used to achieve fast reaction at the initial stage, while a subsequent low reaction rate was attained by switching to K_2PtCl_4 at low concentration. The success of this strategy in facilitating the formation of Pt/Ag nanoboxes with smooth walls indicates the importance of the right reaction kinetics. Comparing to the GRR between K_2PtCl_4 and Ag NCs without HCl, we found that the color change of the reaction from yellow to gray occurred much faster when HCl was added to the Ag NCs (20 *vs*. 4 sec), indicating higher reaction rate in the presence of HCl. The use of halide ions to promote GRR kinetics can be attributed to the enhanced surface diffusivity of Ag due to the strong coordination of halide ions to Ag^{+}[186]. Similar effect has been observed for the case of Pd. For instances, Zheng *et al*. found that for the GRR between Pd nanocubes and $Pt(acac)_2$, the use of I^- may facilitate the out-diffusion of Pd for creating hollow Pt/Pd nanoboxes[158]. Xia *et al*. also employed Br^- for the preparation of Pt/Pd concave nanostructures[53].

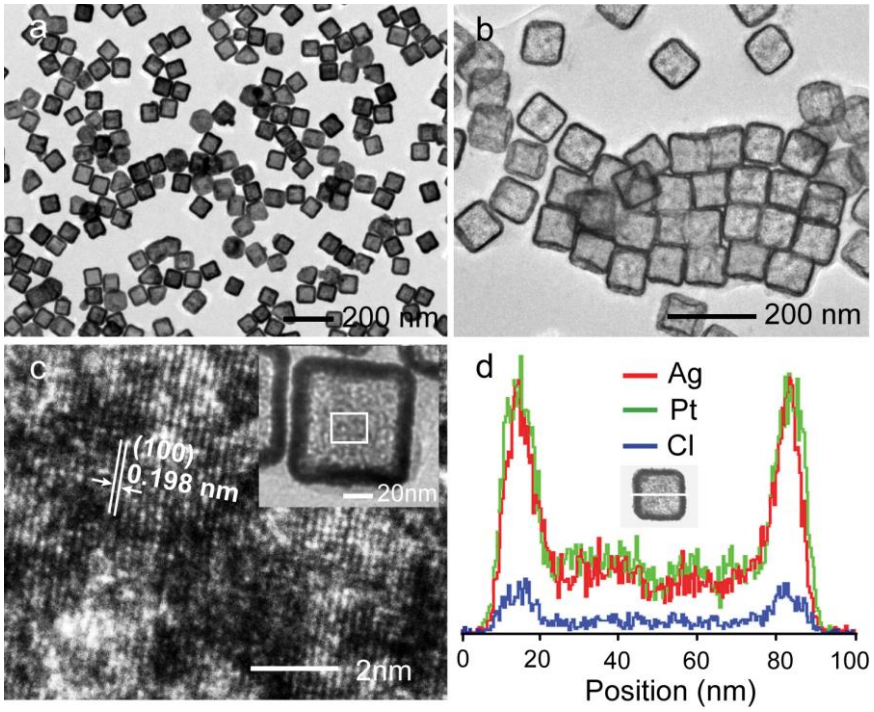

Figure 4.3 TEM images of (a) Pt/Ag nanoboxes, (b) Pt/Ag nanoboxes after washing with 50 mM $Fe(NO_3)_3$ solution. (c) HRTEM and (d) EDX line profile of Pt/Ag hollow nanoboxes. The measured d-spacing of 0.198 nm can be indexed as (100) planes of Pt/Ag alloy since it is between Pt(100) (0.196 nm) and Ag(100) (0.204 nm).

4.2.2 Pt/Ag dimers

In addition to HCl, PVP also plays an important role in defining the morphology of the Pt/Ag nanostructures. PVP is often used as a shape and size control agent in nanostructure synthesis. When reactions similar to the synthesis of Pt/Ag nanoboxes were carried out without adding PVP (*i.e.*, following the reaction route in Figure 4.1b), heterodimers instead of nanoboxes were obtained. Figure 4.4 and Figure 4.5a show the dimeric nanoparticles prepared by adding 0.23 mL of 10 mM HCl into the dispersion of 50-nm Ag NCs (molar ratio of HCl:Ag = 2.75:1), followed by injecting 0.5 mL of K_2PtCl_4 solution (5 mM) at 100 ℃. TEM of the as-prepared samples

shows that each heterodimer is composed of two domains -- a hollow nanobox with an attached solid particle. For most dimers, the solid particle is located at the corner of the nanoboxes, although some along the side have also been observed. The nanoboxes have an average edge length of 50 nm with a wall thickness of ~5 nm. The average size of the attached particles is 53 nm, close to that of the nanoboxes. We also found that the number of attached particles on each nanobox can be tailored by controlling the molar ratio of HCl to Ag. After washing with NaCl and $Fe(NO_3)_3$ solutions, the attached solid particles on each nanobox became hollow – the original heterodimers were converted to nanostructures with two hollow domains, while the wall thickness of the cubic part reduced to 2 nm (Figure 4.5b).

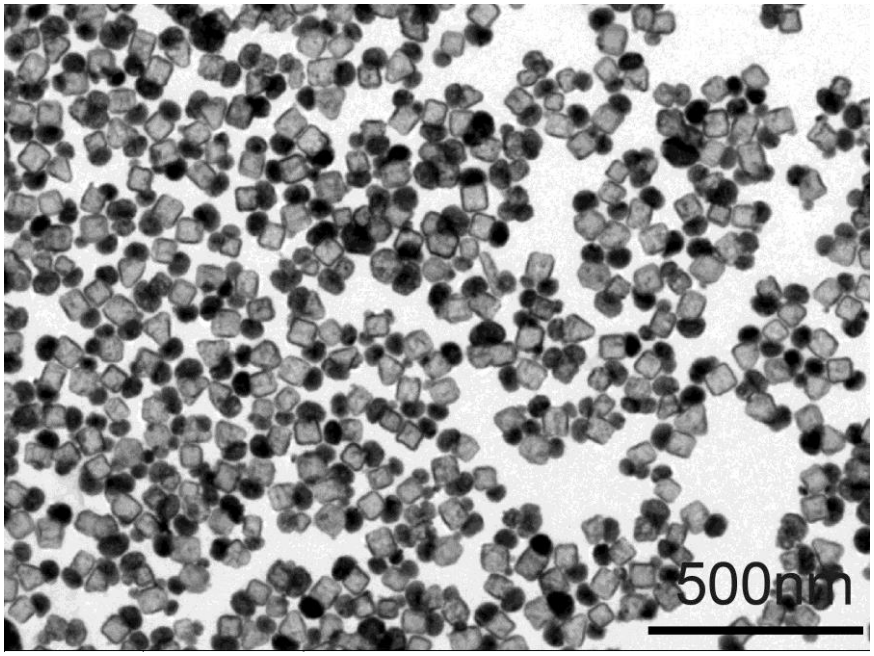

Figure 4.4 Low magnification TEM image of Pt/Ag heterodimers

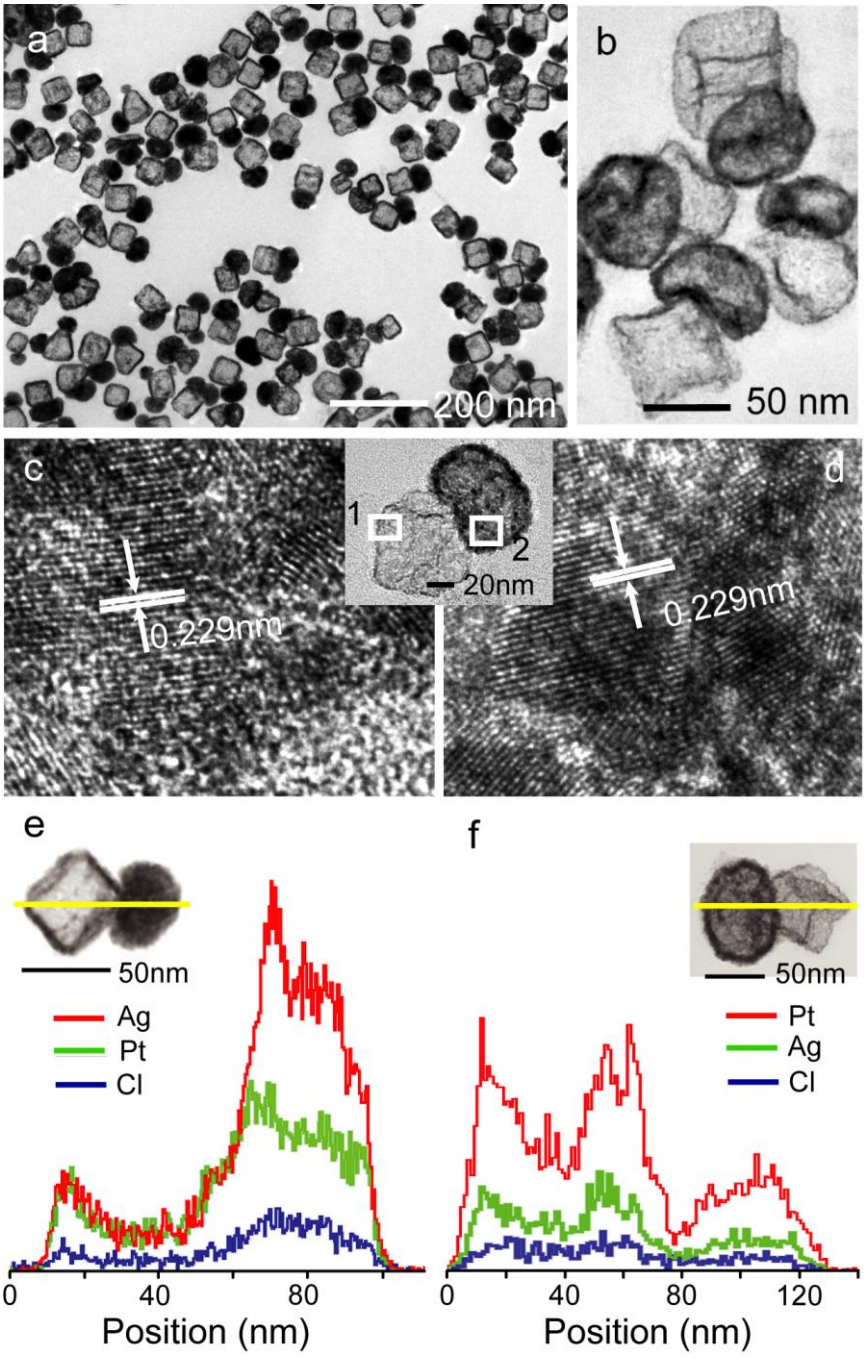

Figure 4.5 TEM images of (a) Pt/Ag heterodimers, (b) Pt/Ag heterodimers with two hollow domains after washing with solutions of saturated NaCl and 50 mM $Fe(NO_3)_3$. (c, d) HRTEM images of the two hollow domains (indicated by 1 and 2, respectively) of a Pt/Ag dimer after washing. (e, f) EDX line profiles of the Pt/Ag heterodimers before and after washing with NaCl and $Fe(NO_3)_3$ solutions, respectively.

To understand the formation of attached particles on nanoboxes, we carefully analyzed the composition of the dimers. X-ray diffraction (XRD) pattern of the as-prepared heterodimers revealed two sets of reflection peaks -- one set correspond to AgCl, and the other set are located between the reflections of Pt and Ag, corresponding to Pt/Ag alloy (Figure 4.6a). The presence of both Pt/Ag alloy and AgCl in the heterodimers was also confirmed from EDX line scan. Figure 4.5e shows the composition line profile of an as-prepared dimer. Both Pt and Ag were found in the hollow box and its attached solid particle. However, while the hollow box has similar amount of Pt and Ag, the attached solid particle shows more Ag than Pt. In addition to Pt and Ag, Cl is also present in the solid particle. These results indicate that for each heterodimer, the hollow box is mainly composed of Pt/Ag alloy,while the attached solid particle contains both Pt/Ag alloy and AgCl. After washing with saturated NaCl solution, XRD peaks of AgCl disappeared completely (Figure 4.6b). Further washing with $Fe(NO_3)_3$ caused the XRD peaks to shift toward Pt due to the dealloying and partial removal of Ag (Figure 4.6c). At this stage, both hollow domains of the heterodimers are mainly composed of Pt/Ag alloy (Figure 4.5f). Figure 4.5c-d show the lattice fringes of the two hollow domains after washing. Since the d-spacings of Pt and Ag (111) planes are 0.226 nm and 0.236 nm, respectively, the 0.229-nm d-spacing measured for the dimer can be indexed as (111) planes of Pt/Ag alloy.

The presence of Pt/Ag alloy and AgCl in the as-synthesized Pt/Ag dimers was also confirmed from X-ray photoelectron spectroscopy (XPS) analysis as

shown in Figure 4.7. For Cl $2p_{3/2}$, typical binding energies are 197.7 eV for AgCl and 198.2 eV for $PtCl_4^{2-}$, respectively. For our sample, the Cl $2p_{3/2}$ peak is located at 197.8 eV, meaning that Cl exists in the form of AgCl. For Pt $4f_{7/2}$, typical binding energies are 73-74.2 eV for K_2PtCl_4, 71.1 eV for Pt, and 70.9-70.2 eV for Pt/Ag alloys, respectively. For our sample, the Pt $4f_{7/2}$ peak is located at 70.7 eV, meaning that Pt mainly exits in alloy form. For Ag $3d_{5/2}$, typical binding energies are 367.4 eV for Ag/Pt alloy, 368.1 eV for AgCl, and 368.3 eV for Ag, respectively. For our sample, the Ag $3d_{5/2}$ peak is located at 367.5 eV, meaning that Ag may exist in the forms of both Ag/Pt alloy and AgCl. The XPS results indicate the presence of Pt/Ag alloy and AgCl in the sample.

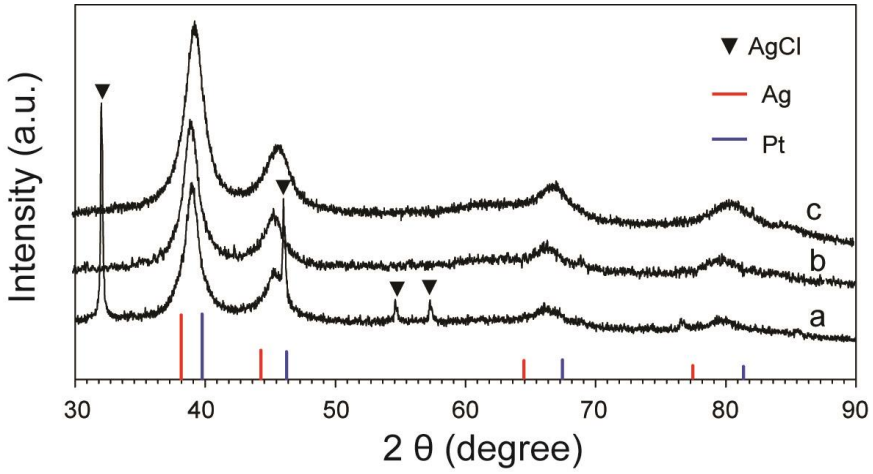

Figure 4.6 XRD patterns of Pt/Ag dimers after washing with (a) H_2O, (b) saturated NaCl solution, and (c) saturated NaCl and $Fe(NO_3)_3$ solutions, respectively.

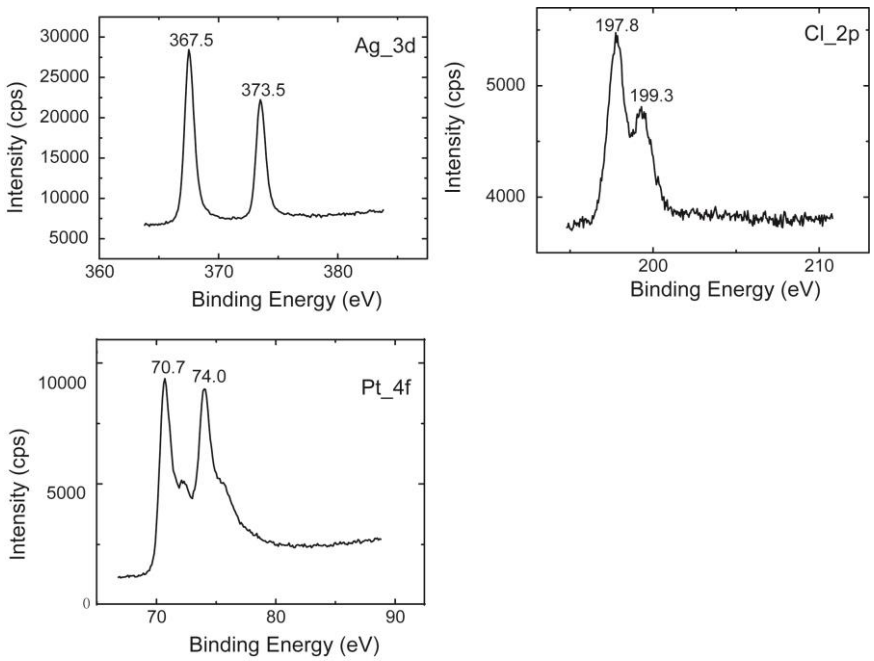

Figure 4.7 XPS of the as-synthesized Pt/Ag dimers. The Pt 4f, Ag 3d and Cl 2p peaks were analyzed based on literature values available from the database provide by NIST (http://srdata.nist.gov/xps/).

It is worth mentioning that due to the presence of Ag in the attached particles before washing with $Fe(NO_3)_3$, one can expect that by reacting the dimers or multimers with another noble metal ions such as $AuCl_4^-$, Ag can be further dissolved from the dimers to form higher-order hybrid nanostructures. Figure 4.8a-b show that after the GRR between heterodimers and $HAuCl_4$, Au particles were formed on the surface of the attached solid particles. Figure 4.8c shows the lattice fringe of 0.236 nm, which is corresponding to (111) planes of Au. The UV-vis spectra show a new LSPR pearks at around 540 nm after heterodimers react with $HAuCl_4$ compared with that of heterodimers (Figure 4.9), which may be ascribed to the typical LSPR peak of Au nanoparticles. Small Au nanoparticles on Pt have proven to be effective on improving the stability and activity of catalytic oxygen reduction reaction[187]. This type of

hybrid structures should be interesting for the study of electrochemical catalysis.

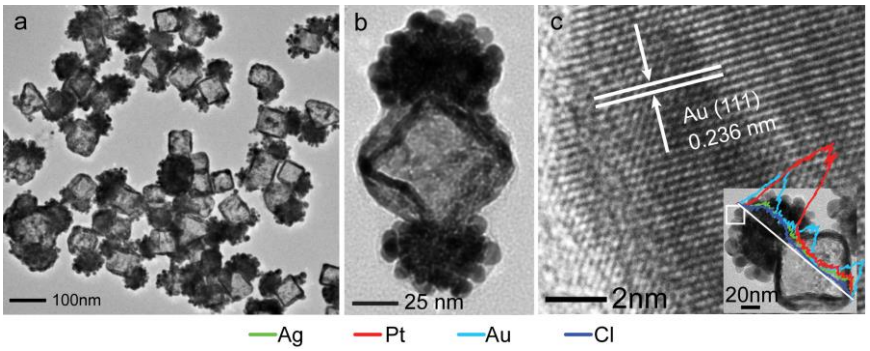

Figure 4.8 (a, b) TEM images of Au/Pt/Ag hybrid structures obtained via reacting the remaining Ag in Pt/Ag dimers with $HAuCl_4$. (c) HRTEM and EDX line profile of a Au/Pt/Ag dimer showing the presence of Au.

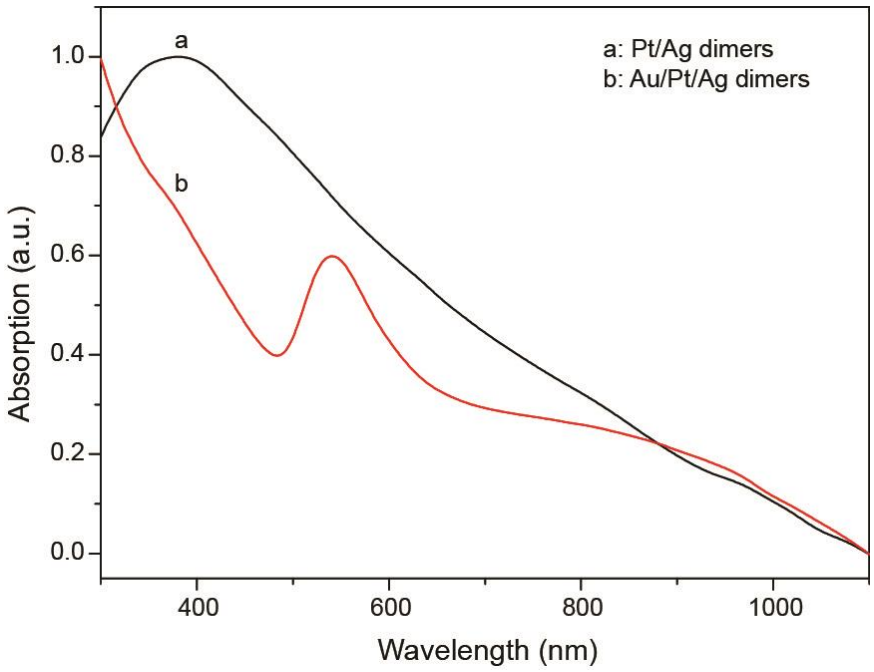

Figure 4.9 UV-visible adsorption spectra of Pt/Ag heterodimers (a) before and (b) after the reaction with $HAuCl_4$.

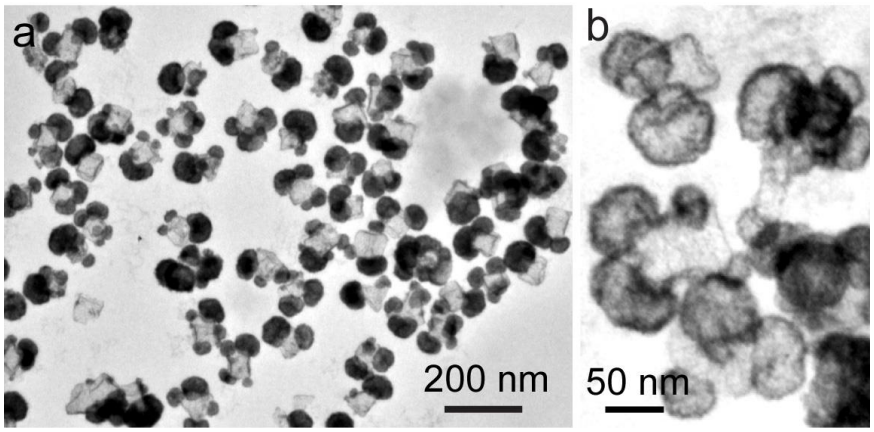

Figure 4.10 TEM images of (a) Pt/Ag multimers, (b) Pt/Ag multimers with two hollow domains after washing with solutions of saturated NaCl and 50 mM $Fe(NO_3)_3$.

4.2.3 Pt/Ag multimers

Figure 4.10a shows the structure with multiple attached solid particles on each hollow nanobox prepared from the GRR at a ratio of HCl:Ag = 4:1. After washing with NaCl and $Fe(NO_3)_3$ solutions, the original multimers with solid attachments were converted to nanostructures with multiple hollow domains (Figure 4.10b). In order to investigate the role of HCl, a series of reactions were conducted by adding different volume of 10 mM HCl solution. By carefully surveying more than 500 nanoparticles for each sample, we plotted the average number of attached particles on each nanobox as a function of the molar ratio of HCl to Ag (Figure 4.11f). A clear trend was observed -- with the increase of the ratio of HCl to Ag, the number of attached particles increases (Figure 4.11a-e).

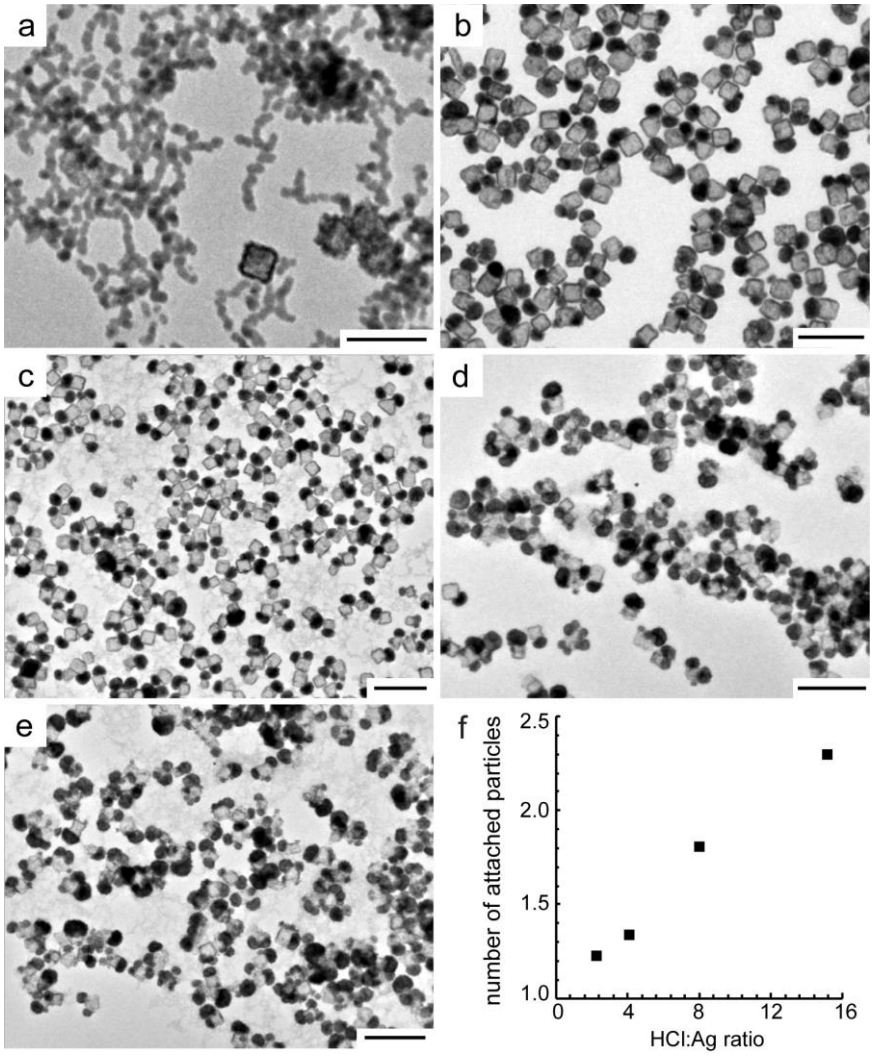

Figure 4.11 TEM images of Pt/Ag nanostructures prepared from a series of GRR between 5 mM K_2PtCl_4 and dispersions of Ag NCs at different HCl to Ag ratios: (a) 0, (b) 2.75, (c) 4, (d) 8, and (e) 15. All samples were washed by saturated NaCl after GRR. (f) The average number of attached particles on each nanobox for the sample prepared at different molar ratio of HCl to Ag. The scale bar is 200 nm.

4.2.4 Pt/Ag popcorns

As discussed earlier, the effect of HCl in the synthesis of dimeric or multimeric nanostructures is twofold: i) to provide a template composed of AgCl for the growth of Pt; and ii) to regulate the reaction kinetic and thus the

number of deposition sites. Therefore, if HCl is added to the reaction gradually, a different deposition pattern of AgCl, and thus a different morphology of the resulting Pt/Ag structures, is expected. Indeed, when the reaction was carried out by injecting a mixed solution of HCl and K_2PtCl_4 to the dispersion of Ag NCs, we obtained popcorn-shaped nanoparticles (following reaction route in Figure 4.1d). Figure 4.12a-b show the nanopopcorns formed using 50-nm Ag nanocubes after washing with NaCl and $Fe(NO_3)_3$ solutions. The average size of the popcorns is 90 nm. Each nanopopcorn is composed of a number of connected hollow particles (average number = 14) with an average wall thickness of 1.7 nm. HRTEM image (Figure 4.12d) and EDX line profile (Figure 4.12e) indicate that the popcorn-shaped nanostructures are mainly composed of Pt/Ag alloy.

4.2.5 Au/Ag dimers

Au/Ag dimers can also be obtained by using similar reaction conditions when molar ratio of HCl:Ag was 2.75 and $HAuCl_4$ was the noble metal precursor instead of K_2PtCl_4 (Figure 4.13). TEM shows most of resultant particles were heterodimers which was composed of a hollow nanobox and an attached solid particle.

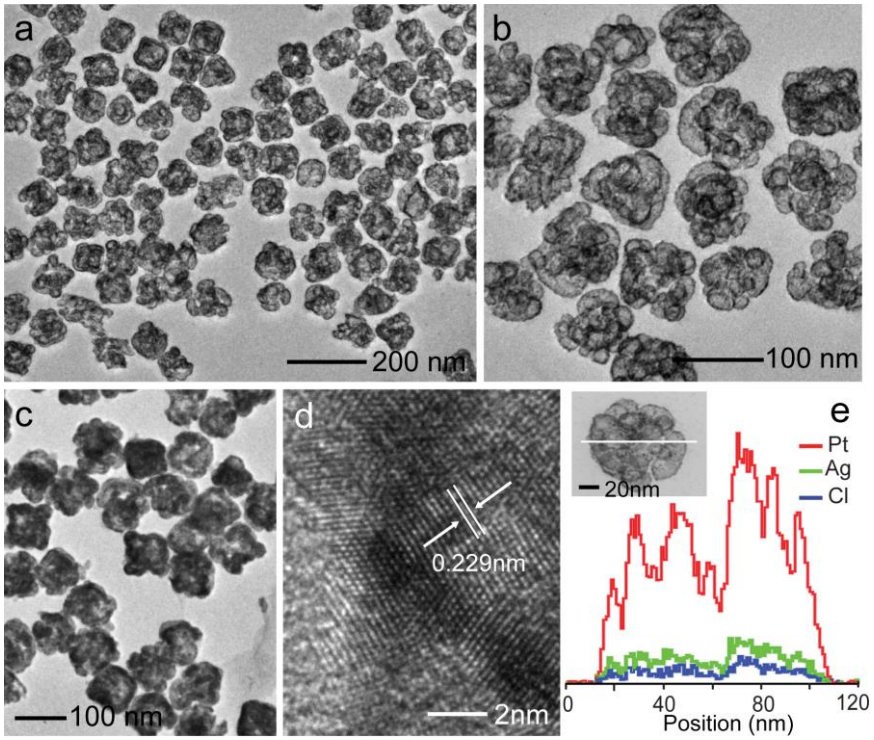

Figure 4.12 (a) TEM images of Pt/Ag popcorn-shaped nanostructures (a, b) after and (c) before washing with solutions of saturated NaCl and 50 mM $Fe(NO_3)_3$. (d) HRTEM image and (e) EDX line profile of a Pt/Ag nanopopcorn.

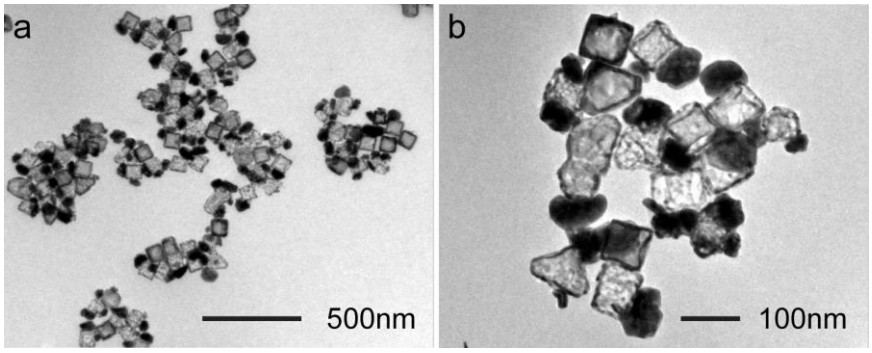

Figure 4.13 TEM images of Au/Ag heterodimers prepared from the GRR between Ag NCs and $HAuCl_4$ in the presence of HCl.

4.2.6 Proposed growth mechanism

Based on the above structural and compositional analyses, we propose the following mechanism for the growth of the attached particles on Pt/Ag nanoboxes. At the initial stage of the reaction between Ag NCs and Pt precursor, due to the presence of excess amount of Cl^-, AgCl is generated instantaneously once K_2PtCl_4 is introduced in the reaction (as shown in Figure 4.14). AgCl grows and form islands on the surface of the Ag NCs. Therefore, Pt atoms formed from the reduction by Ag deposit not only onto the surface of Ag NCs, but also on the attached AgCl islands. With the consumption of Ag, more Ag atoms migrate from the core to the surface of the nanocube to react with Pt precursor. Ag atoms can also diffuse through the AgCl islands and reach their surface to either form alloy with Pt or react with K_2PtCl_4 to give AgCl. Therefore, the islands swell quickly because of the accumulation of both Pt/Ag alloy and AgCl. The corners and edges of the Ag NCs are specially favored for the nucleation of AgCl due to the surface roughness and more defects of these sites[188]. At relatively low concentration of HCl, AgCl tends to nucleate and grow at one defect site. When HCl at high concentration is added to the reaction, the nucleation of AgCl may occur at multiple defect sites since AgCl is generated at higher rate. It is worth noting that, in addition to the templating effect, other factors such as surface adsorbed species may also play a role. Recently, Tao *et al*. showed that positive and negative polyelectrolyte layers on the Ag nanoparticles controlled the GRR with $HAuCl_4$ to obtain different morphologies[189]. When both PVP and HCl are added to the

dispersion of Ag NCs, the surface energy of the Ag NCs is changed due to the adsorbed PVP. Therefore, the nucleation and growth of AgCl take place differently, leading to a relatively uniform growth of Pt on the whole surface of Ag NCs to form nanoboxes.

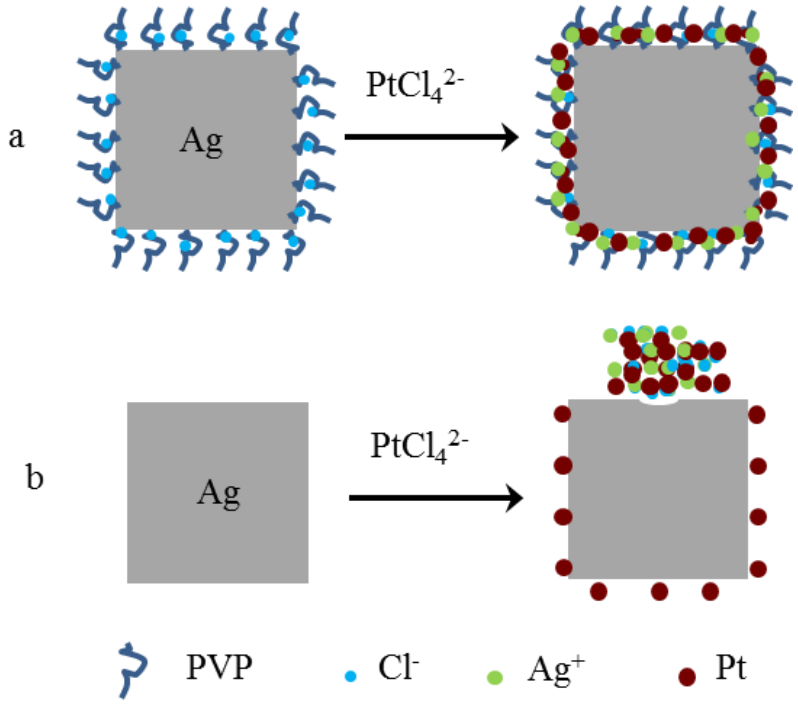

Figure 4.14 Scheme illustration for the initial stage of the formation of Pt/Ag (a) nanobox, (b) heterodimer.

The formation of Pt/Ag dimeric, multimeric and popcorn-shaped nanostructures in addition to simple nanoboxes is made possible by two reasons. First, we take the advantage of the undesirable by-product, AgCl, of the reaction to direct the deposition of Pt. The GRR between Ag and K_2PtCl_4 generates AgCl, which has a low solubility in water and may precipitate out from the solution[153,184]. In this work, HCl is used to purposely facilitate the precipitation of AgCl, which subsequently grows on the surface of Ag NCs to

form attached islands. With the progress of the reaction, the AgCl islands serve as *in situ* generated secondary templates for the deposition of Pt. Once the reaction completes, AgCl can be easily removed by washing with saturated NaCl solution to form void space. Second, the number of AgCl islands attached on each Ag NC is regulated by either adjusting the concentration of HCl or by adding PVP to the dispersion of Ag NCs. We found that while HCl at higher concentration leads to higher reaction kinetics and hence multiple attached islands on Ag NCs, the addition of PVP results in uniform coating of AgCl and thus smooth hollow nanoboxes. Together, these two mechanisms allow us to extend GRR to the preparation of more complex bimetallic nanostructures with tailored number of hollow domains.

4.2.7 Electrochemical measurements

It is expected that, for the Pt/Ag dimers and popcorns, the presence of multiple hollow interiors and highly porous walls possess high specific surface area favoring electrochemical catalysis. Therefore, we tested the hollow nanostructures for methanol oxidation reactions (MOR) and compared their catalytic activities with commercial Pt/C (20 wt%) catalyst with an average diameter of 3.2 nm (based on TEM shown in Figure 4.15). Figure 4.16a shows the cyclic voltammograms (CVs) of Pt/Ag popcorns, dimers, nanoboxes, and Pt/C recorded in 1 M $HClO_4$. Based on the charge of hydrogen adsorption, the electrochemically activated surface areas (ECSAs) were calculated using the following equations 4.1 and 4.2:

$$Q_H = \frac{S}{v} \qquad (4.1)$$

$$ECSA = \frac{Q_H}{[Pt] \text{ X } 0.21} \qquad (4.2)$$

Where Q_H is the charge for hydrogen desorption (mC), S is the integrated area of the hydrogen desorption (mA V), ν is the scan rate (mV s^{-1}) which is 50 mV s^{-1}, [Pt] represents the Pt loading (mg) on the electrode, and 0.21 (mC cm^{-2}) is the charge required to oxidize a monolayer of H on Pt. The Pt loading was 5 μg, which was confirmed by ICP-MS. The integrated area for H desorption, Q_H, and ECSA of each catalyst are listed in table 4.1.

Table 4.1 Integrated area for H desorption, Q_H, and ECSA of the catalysts.

	Pt/C	**Popcorns**	**Dimers**	**Nanoboxes**
Integrated Area (mAV)	0.0272	0.0477	0.0431	0.0274
Q_H (mC)	0.544	0.954	0.862	0.548
ECSA (m^2/g)	51.81	90.86	82.09	52.19

For Pt/Ag popcorns, dimers, hollow boxes, and Pt/C, their ECSAs are 90.86, 82.09, 52.19, and 51.81 m^2/g, respectively (Figure 4.16b). As expected, Pt/Ag dimers and popcorns have much higher ECSAs than that of Pt/C. MORs were performed at room temperature in a solution containing 1 M KOH and 1 M CH_3OH (Figure 4.16c). For the four samples, the peak current densities decrease in the following order: Pt/Ag popcorns [116.1 mA cm^{-2}] > dimers

[98.6 mA cm^{-2}] > nanoboxes [84.2 mA cm^{-2}] > Pt/C [76.9 mA cm^{-2}]. It is obvious that Pt/Ag popcorns and dimers exhibit improved MOR activities relative to commercial Pt/C (51% and 28% higher, respectively). Based on the loading of Pt on the electrode, the mass specific activities of the Pt/Ag nanostructures were calculated and plotted in Figure 4.16d. It is worth noting that the ECSA and MOR activity of our Pt/Ag nanostructures are competitive compared to existing Pt nanostructures (*e.g.*, ultrathin Pt nanowires with an ECSA of 71.34 m^2 g^{-1} and a MOR mass specific activity 18% higher than commercial Pt/C)[190]. To evaluate the stability of the Pt/Ag catalysts, we performed chronoamperometry (CA) measurements at a constant potential of -0.4 V *vs.* SCE. As shown in Figure 4.17, Pt/Ag dimers, nanopopcorns and nanoboxes exhibited better stability than Pt/C.

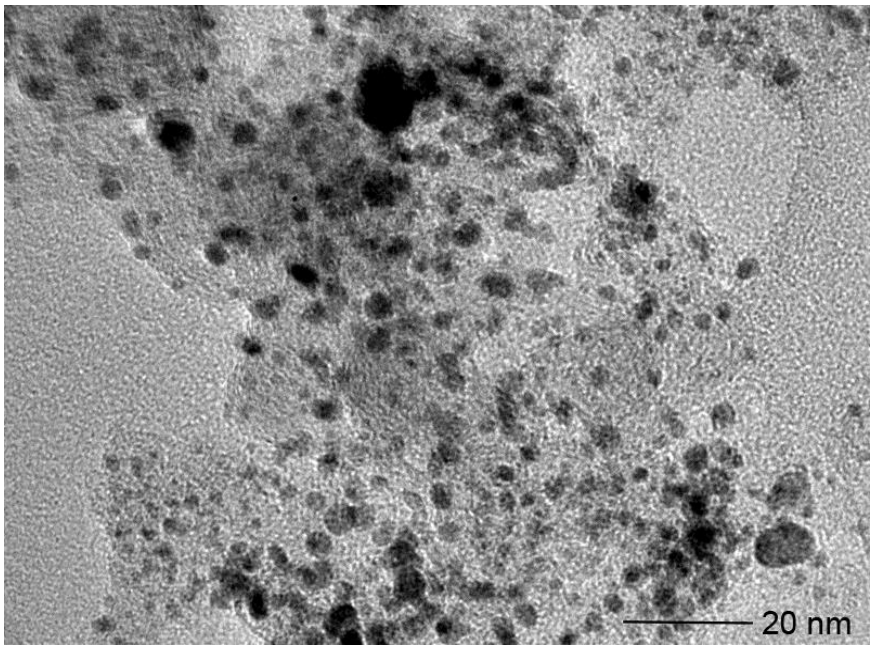

Figure 4.15 TEM image of commercial Pt/C catalyst.

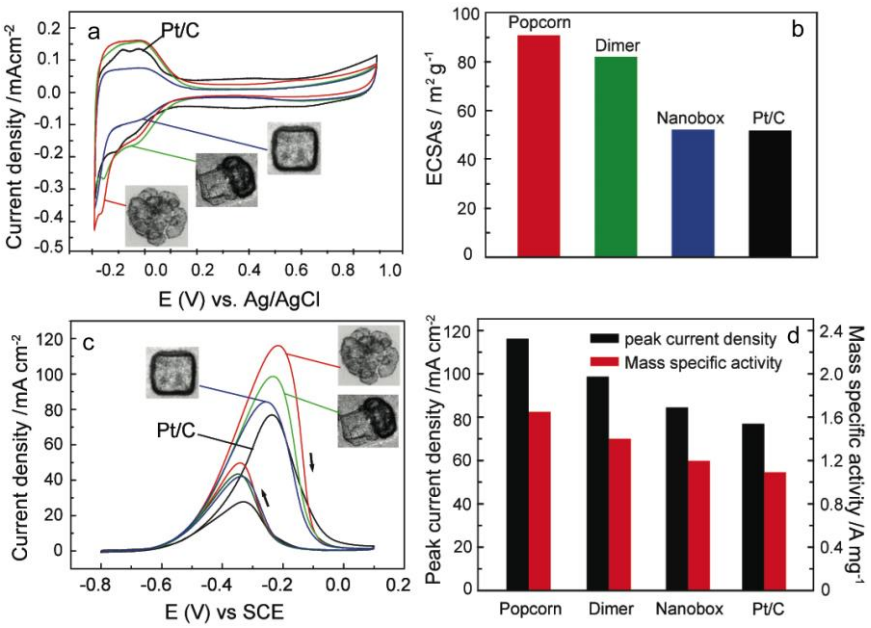

Figure 4.16 (a) Cyclic voltammograms (CVs) of Pt/C, Pt/Ag hollow nanoboxes, dimers, and popcorns in 1 M $HClO_4$. (b) ECSA of each catalyst. (c) CVs for MOR in a solution containing 1M CH_3OH and 1 M KOH. (d) Mass activity of each catalyst. The scan rate for all CVs is 50 mV s^{-1}.

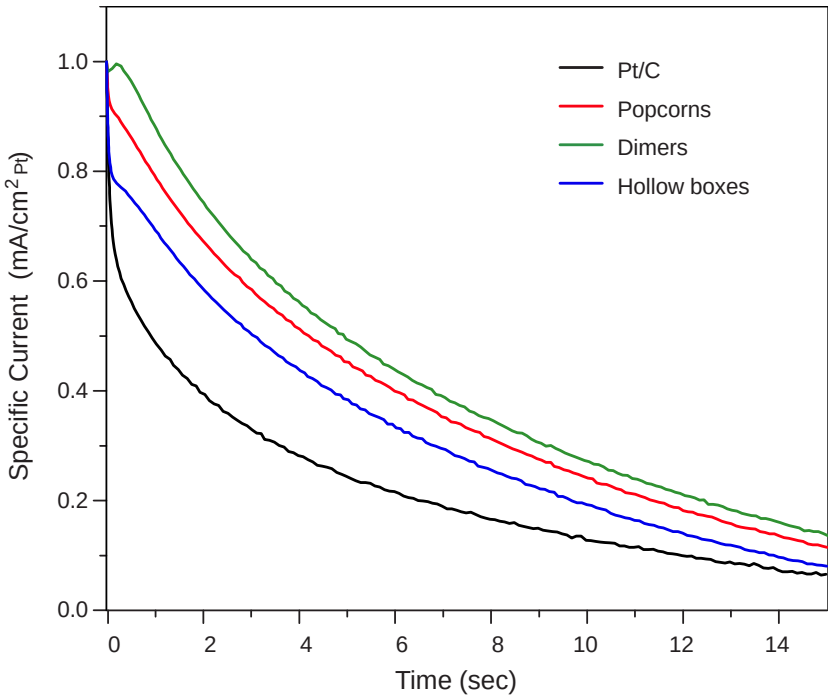

Figure 4.17 Chronoamperometry measurements of Pt/Ag hollow nanoboxes, dimers, nanopopcorns and Pt/C at a constant potential of -0.4 V versus SCE.

4.3 Conclusions

Distinct Pt/Ag hollow nanostructures with controlled number of voids have been synthesized *via* GRR between Ag NCs and K_2PtCl_4 in the presence of HCl. The use of HCl allows the deposition of AgCl on the surface of Ag NCs to regulate the growth of Pt. It is demonstrated that the number of deposition sites for AgCl can be effectively controlled by the amount of HCl. Based on this strategy, GRR has been successfully extended to the preparation of bimetallic dimers, multimers, and popcorn-shaped nanostructures. These novel nanostructures with high surface area should be promising for electrochemical catalysis.

Chapter 5. Synthesis of Au/Ag@ATP@Au/Ag Sandwich Structures with Controlled Interior Gap Sizes for Surface-Enhanced Raman Scattering (SERS)

5.1 Introduction

Research interest in surface-enhanced Raman scattering (SERS) has grown dramatically since it was discovered in 1974.[191] One of the hottest topics about SERS is the study of the enhancement mechanism. It has been generally accepted that the SERS is the outcome of both electromagnetic (EM) enhancement and chemical (CM) enhancement.[192-194] EM enhancement is caused by the collective excitation of surface electrons of a metal substrate.[192,195] It is the main contribution to SERS because the electromagnetic field of the incident light at the substrate surface can be enhanced in the form of $|E|^4$ (E-the electromagnetic fields).[196] Compared to EM enhancement, CM enhancement may be attributed to a few reasons such as: i) the change in chemical environment of SERS probe molecules; ii) the resonance effect between electronic states of the molecule and the excitation wavelength; and iii) the resonance effect between new electronic states of the metal and the molecule with the excitation wavelength.[196-198]

With the progress of further understanding of the SERS enhancement mechanism, researchers have paid a great deal of attention to plasmonic nanostructures with small gaps.[199-203] This is because the small gaps can serve

as hot spots that induce an intense localized electromagnetic field, favoring significantly enhanced Raman signals. For example, both random aggregations of plasmonic particles and metal-molecule-metal junctions obtained through self-assembly have shown hot spots at the junction of two plasmonic nanoparticles.[203-209] In most studies, 4-ATP is used as probe reporter for SERS mechanism studies. This is because 4-ATP molecule is a bifunctional linker molecule and shows a conjugated π system connected with both "electron-donating and electron accepting group.[206]

When 4-ATP molecules are located within the hot spots, their totally symmetric (a_1) and non-totally symmetric (b_2) vibrations are selectively enhanced in SERS spectrum. Singamaneni et al. obtained Au core-satellite nanostructures with 4-ATP molecules located in the gap and observed highly enhanced a_1-type modes of the 4-ATP Raman signal.[203] In addition to the enhanced a_1-type modes, Zheng and coworkers also demonstrated the b_2-type modes of 4-ATP can also be enhanced due to the charge transfer mechanism in the Au-Ag sandwich structure using off-surface Plasmon excitation to minimize the EM effect.[206] However, the nano-sized gap existing in either the aggregation of plasmonic metal particles or the metal-molecule-metal junction is usually unstable and irreproducible, so as the measured enhancement factor (EF).[210,211] Therefore, the fabrication of plasmonic nanostructures with stable and reproducible hot spots is still challenging. One alternative synthetic route to plasmonic structures with nano-sized gap is to form a sandwich structure with an interior gap which traps probe molecules. Recently Lim et al.

synthesized Au nano-bridged core-shell particles by using DNA-modified Au nanoparticles as the seeds.[199] The DAN-tailorable nanostructures with a 1-nm interior gap loaded with Raman dyes exhibited highly stable and reproducible SERS signals.

In this work, we studied the synthesis of a sandwich plasmonic structure with controlled interior gap size based on galvanic replacement reaction (GRR). The SERS enhancement effect was investigated with a SERS probe molecule, 4-aminothiophenol (4-ATP), trapped in the interior gap of the sandwich structure. The synthesis is illustrated in Figure 5.1. To prepare the sandwich structures, high quality Ag nanocubes was used as the sacrificial template to form Au/Ag alloy nanoboxes via GRR with $HAuCl_4$ solution (Figure 5.1 step A). The resulting Au/Ag nanoboxes were incubated in 4-ATP solution for overnight to form a monolayer of ATP adsorbed onto the surface of these nanoboxes due to the high affinity between the thiol group of 4-ATP and the surface Au or Ag atoms of the nanoparticles (Figure 5.1 step B). Once Au/Ag nanoboxes were coated with monolayer of 4-ATP, a conformal layer of Ag was grown on the surface of nanoboxes by the electroless plating. So the 4-ATP molecules were buried underneath the Ag coating (Figure 5.1 step C). The second round of GRR was then carried using the Ag layer of each nanoparticle as the template to form the second Au/Ag alloy nanoshell (Figure 5.1 step D). And a nanogap with embedded 4-ATP molecules between the two Au/Ag alloy shells for each particle was generated. The resulting sandwich structure is denoted as Au/Ag@ATP@Au/Ag. The gap size can be controlled

by the thickness of Ag shell formed in step C and the amount of $HAuCl_4$ solution used in the second round of GRR in step D.

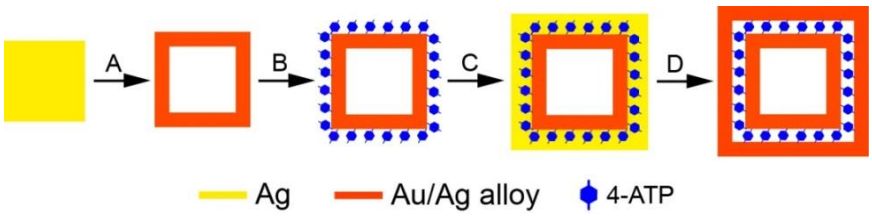

Figure 5.1 Schematic illustration of the synthetic process for the sandwich nanostructures, (A) first round of GRR using Ag nanocubes as template to form Au/Ag nanoboxes, (B) adsorption of 4-ATP on the surface of Au/Ag hollow boxes to form Au/Ag@ATP, (C) electroless plating of Ag layer on the surface of the hollow boxes to give Au/Ag@ATP@Ag, (D) the second round of GRR to form Au/Ag@ATP@Au/Ag sandwich structure.

5.2 Results and Discussion

5.2.1 Characterization of Ag nanocubes and Au/Ag single-walled hollow boxes

Ag NCs were preferred for this study because they can be routinely synthesized with a large amount and high quality using the polyol process.[54] As shown in Figure 5.2a, Ag NCs with an edge length of 70±4 nm exhibit smooth surfaces, sharp corners and edges. It is well known that GRR is a powerful and facile synthetic approach to synthesize hollow nanostructures.[24,39,115] In the GRR reaction with $HAuCl_4$, Ag NCs acted as template for formation of Au/Ag single-walled hollow boxes. Figure 5.2b shows the resultant Au/Ag single-walled hollow boxes with well-defined and uniform walls. The average edge length and wall thickness of the hollow boxes are 85 nm and 6 nm, respectively. The average length of these

nanoboxes is larger than that of Ag NCs because of the combined action of a net deposition of Au atoms on the surface and the lateral diffusion of atoms across the outer surface.[39,130,160]

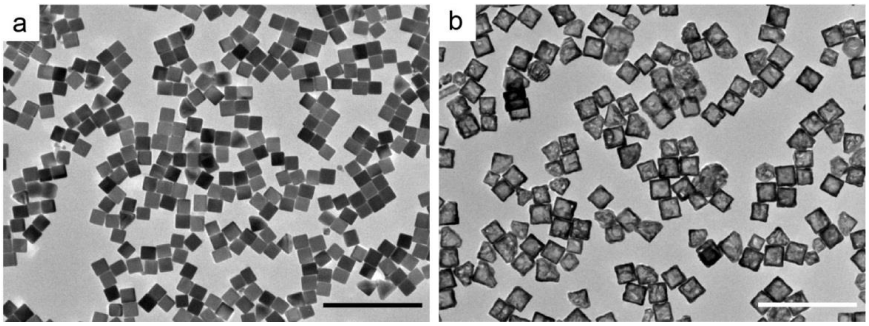

Figure 5.2 TEM images of Ag nanocubes and Au/Ag hollow boxes.

5.2.2 Characterization of Au/Ag@ATP@Ag

The resulted Au/Ag hollow boxes were incubated in a solution with 4-ATP for 12 hours at room temperature in order to obtain one monolayer of 4-ATP on the surface of Au/Ag hollow boxes. Since 4-ATP has strong affinity to Au and Ag, these molecules can be strongly adsorbed on the surface of hollow boxes through Au-S and Ag-S bonding. In addition, the amino function group in 4-ATP also has affinity to noble metal, which facilities the growth of Ag layer on the surface of hollow boxes.[212-214] It is reported that the area occupied by one 4-ATP molecule on Au (111) facet is around 0.2 nm^2.[215,216] Based on the calculation, the amount of 4-APT molecules in the incubation solution was 85 times as much as what was required to cover the surface of the Au/Ag hollow boxes. Hence, it is likely that a monolayer of 4-ATP molecules was formed on the surface of Au/Ag hollow boxes. This structure is named as Au/Ag@ATP.

Figure 5.3 shows the Au/Ag@ATP@Ag sandwich structures with four different thicknesses of Ag shell obtained by reducing different amounts of silver nitrate ($AgNO_3$) by ascorbic acid (AA) in the presence of sodium hydroxide (NaOH). According to the average sizes of Au/Ag hollow boxes and Au/Ag@ATP@Ag sandwich structures (Figure 5.4a), the four thicknesses of the Ag shells are 4.3, 6.0, 11.0, and 21.1 nm, respectively. TEM images reveal that the Au/Ag@ATP@Ag nanopaticles remained the cubic shape after the deposition of a thin layer of Ag (Figure 5.3a-c). However, when the thickness of the Ag layer was increased to 20 nm, the Au/Ag@ATP@Ag nanoparticles became cuboctahedra (Figure 5.3d). This is because the different growth rates of Ag along different crystallographic directions once a critical thickness of Ag layer is reached during the electroless plating.[24] After the coating of Ag shell, the 4-ATP molecules on the surface of Au/Ag hollow boxes were embedded under the Ag shell (Au/Ag@ATP@Ag). Recently, Chen at al. reported that 4-mercap-tobenzoic acid (MBA) as probe reporter can be planted at the interface of Au@Ag core-shell structures.[217] Even though the existence of probe molecules under the Ag shell cannot be directly characterized, their enhanced SERS results convincingly supported that the probe molecules were located underneath the Ag shell. UV-vis spectra show that the localized surface plasmon resonance (LSPR) peaks of the Au/Ag@ATP@Ag nanoparticles red-shifted compared with Au/Ag hollow boxes (Figure 5.4b).

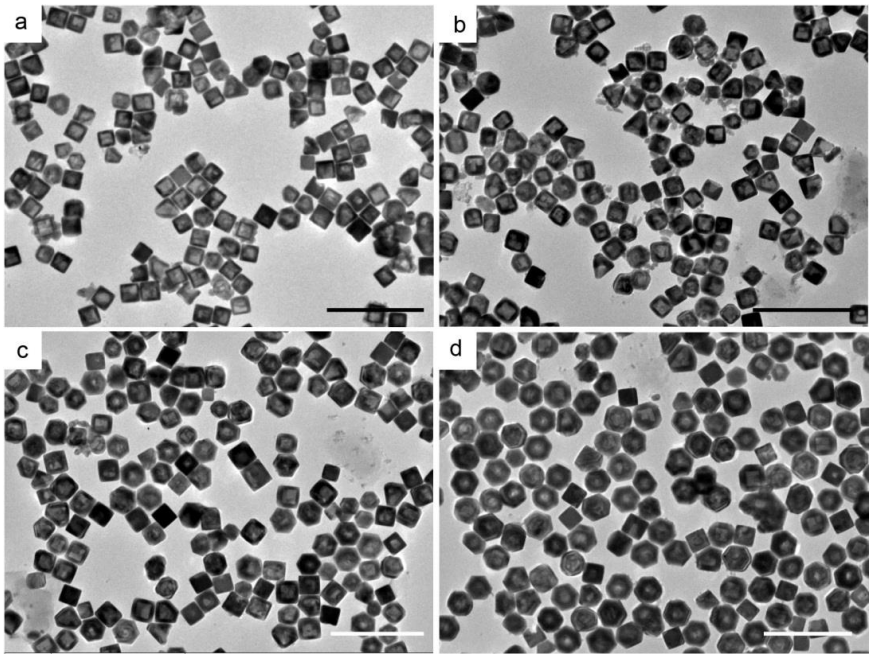

Figure 5.3 TEM images of Au/Ag@ATP@Ag with different thickness of Ag shell: (a) 4.3 nm; (b) 6.0 nm; (c) 11.0 nm; and (d) 21.1 nm.

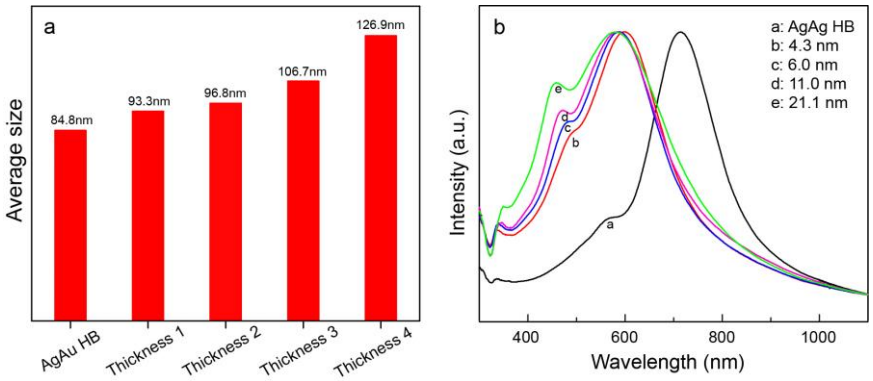

Figure 5.4 (a) The average particle sizes of the Au/Ag hollow boxes and the Au/Au@ATP@Ag sandwich structures, (b) UV-Vis adsorption spectra of Au/Ag hollow boxes (curve a) and Au/Ag@ATP@Ag sandwich nanostructures with different thickness of Ag shell (curves b-e).

5.2.3 Characterization of Au/Ag@ATP@Au/Ag sandwich structures

Figure 5.5 shows the Au/Ag@ATP@Au/Ag sandwich structures prepared via another round of GRR by using Au/Ag@ATP@Ag as template to react with $HAuCl_4$. TEM images clearly show that the sandwich structures have a cubic shape with two hollow boxes separated by an interior gap (Figure 5.5a-d). Four different gap sizes, 1.2, 2.5, 8.0 and 15.6 nm, respectively, were obtained as shown in Figure 5.5 i-l and Figure 5.7a. The gap size was tuned by controlling the thickness of the coated Ag layer and the extent of the second round GRR. The thickness of the Ag layer can be controlled by adjusting the amount of the $AgNO_3$ during the electroless plating process, while the extent of GRR can be controlled by varying the injected amount of $HAuCl_4$ during the reaction.[21] In the resulting sandwich structures, 4-ATP probe molecules remained in the interior gap between two Au/Ag shells after the second round of GRR. The low-magnification TEM images show that these sandwich structures are dispersed well (Figure 5.6). The LSPR peaks of the sandwich structures are located between 700nm and 800nm after two rounds of GRR (Figure 5.7b). To verify the composition of each structure, EDX line scan was performed on individual Au/Ag@ATP@Au/Ag sandwich structure (Figure 5.8). The results show that the compositions of two shells are Au/Ag alloy. According to atomic ratios of Ag to Au, the compositions of the structures with different gap size are slightly different. Since the same hollow boxes were used as the template, the composition of the inner hollow boxes should

be the same. Hence, the difference in composition should be due to the different extents of the second round of GRR.

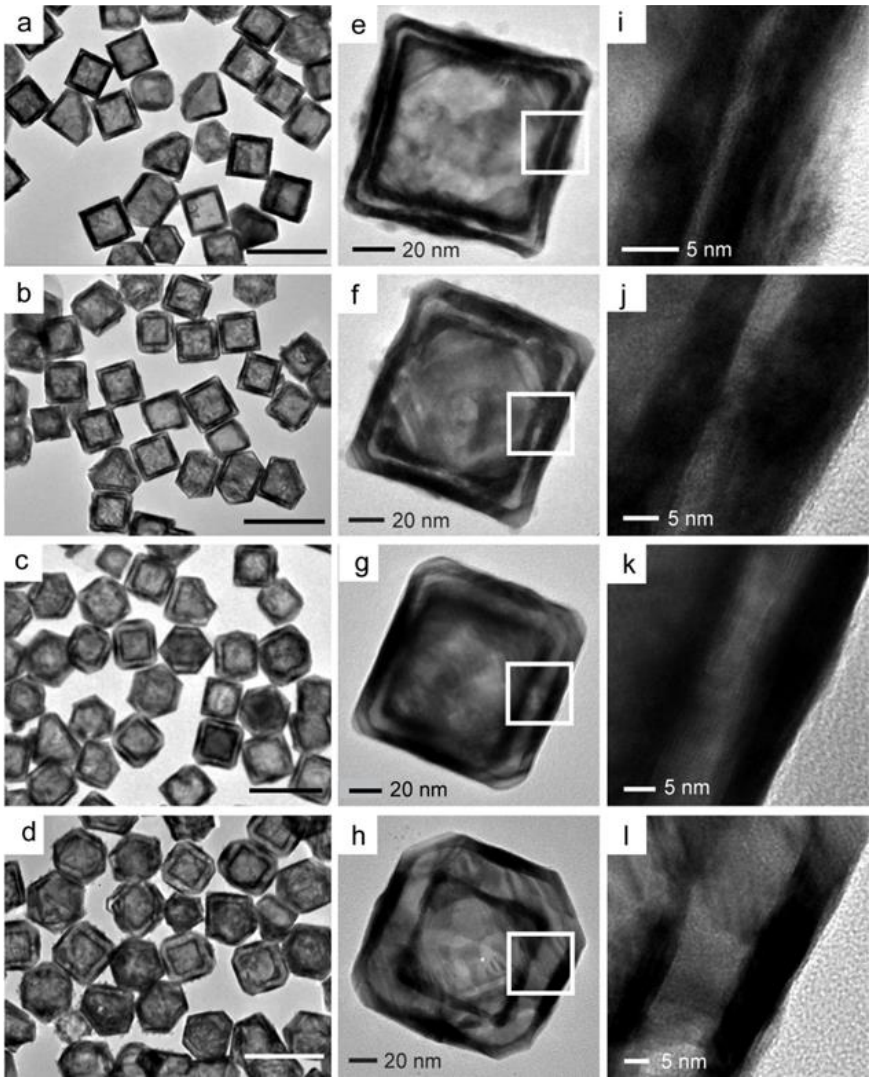

Figure 5.5 TEM images of sandwich structures with different gap sizes: (a) 1.2 nm, (b) 2.5 nm, (c) 8.0 nm, and (d) 15.6 nm.

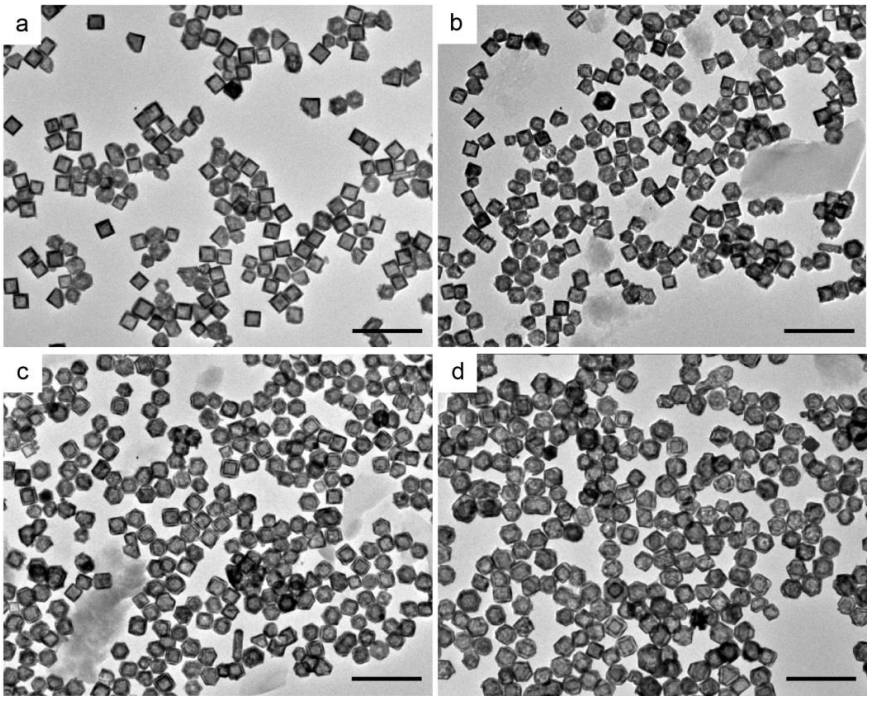

Figure 5.6 Low-magnification TEM images of the sandwich structures with different gap sizes: (a) 1.2 nm; (b) 2.5 nm; (c) 8.0 nm; and (d) 15.6 nm.

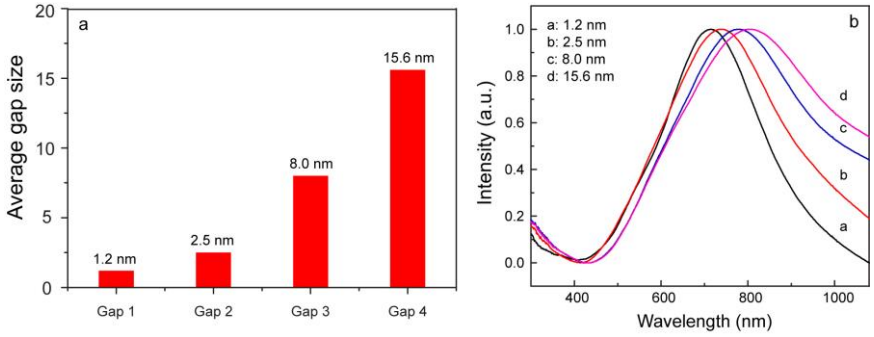

Figure 5.7 (a) Gap sizes of the Au/Au@ATP@Au/Ag sandwich structures and (b) UV-Vis extinction spectra of the Au/Au@ATP@Au/Ag sandwich structures with different gap sizes.

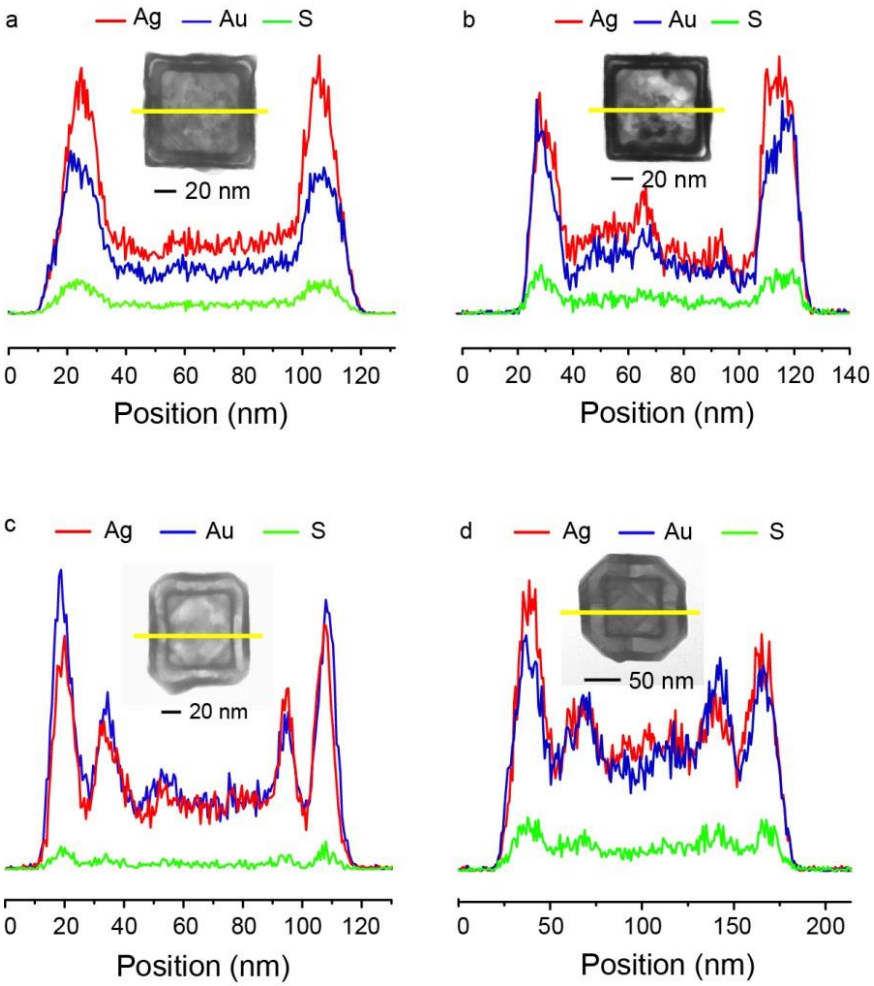

Figure 5.8 EDX line profiles of the sandwich structures with different gap sizes: (a) 1.2 nm; (b) 2.5 nm; (c) 8.0 nm; and (d) 15.6 nm.

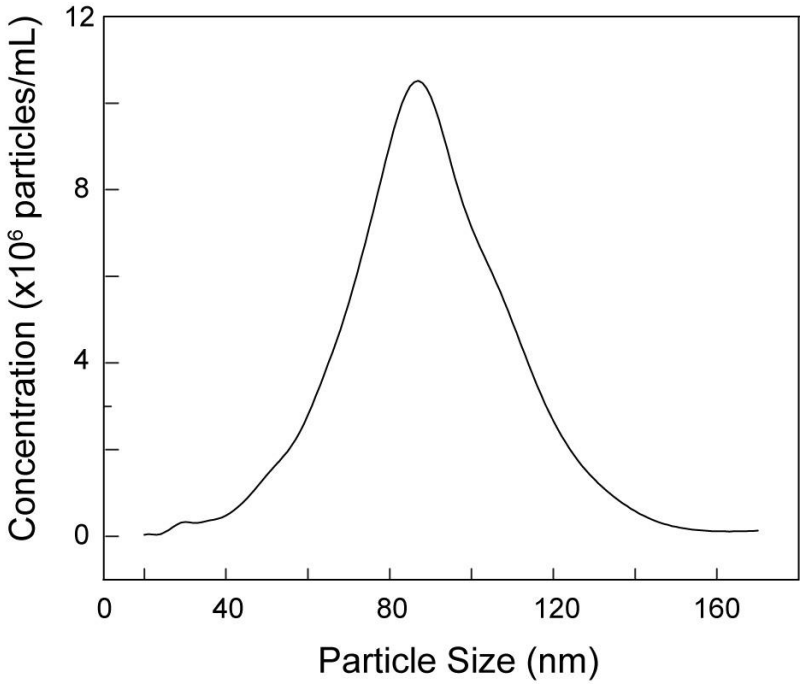

Figure 5.9 Particle concentration of Au/Ag@ATP@Au/Ag sandwich structure that shows interior gap of 1.2 nm.

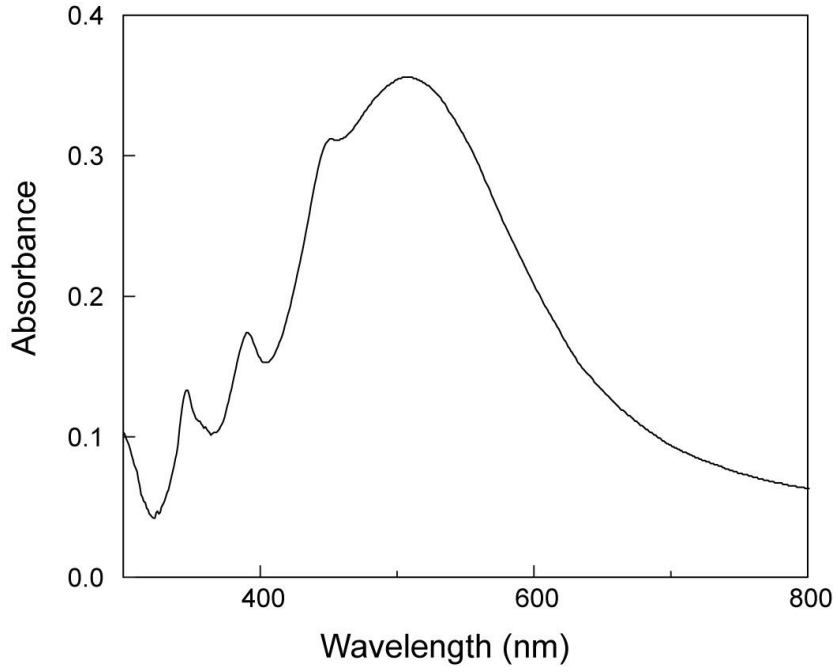

Figure 5.10 UV-Vis extinction spectrum of the Ag nanocubes.

5.2.4 Raman measurement

Au/Ag@ATP@Au/Ag sandwich structures with the presence of 4-ATP in the interior gaps should facilitate repeatable and stable SERS signal. We studied the SERS EFs of the Au/Ag@ATP@Au/Ag sandwich structures with 514.5- and 637-nm lasers as the excitation wavelengths, respectively. The SERS spectra were acquired from colloidal samples with the same concentration (4×10^{10} particles/mL), which was confirmed using nanosight (Figure 5.9). Therefore, similar amount of ATP molecules of each sample should be expected. Figure 5.11 shows the SERS spectra of 4-ATP molecules embedded in the interior gaps of the sandwich structures and adsorbed on the surface of Ag nanocubes, respectively, which are acquired with 514.5-nm laser. For the SERS spectra of the sandwich structures, there are six dominant bands of ATP: two a_1-type bands at 1075cm^{-1} (7a) and 1178 cm^{-1} (9a) and four b_2-type bands at 1142cm^{-1} (9b), 1391cm^{-1} (3), 1436cm^{-1} (19b) and 1579cm^{-1} (8b), which are the same as those obtained from metal-ATP-metal assembled sandwich structures.[206,213,203] When 4-ATP is adsorbed on the surface of the Ag nanocubes, except a_1 modes at 1075 cm^{-1} and 1182 cm^{-1}, there appear two more a_1 modes at 1005 cm^{-1} (18a), and 1591 cm^{-1} (8a). Figure 5.12a clearly shows the comparison of the intensities of a_1 and b_2 modes of 4-ATP located in the gaps of sandwich structures and adsorbed on the surface of Ag nanocubes. In the SERS spectra of sandwich structures, the intensities of b_2-type bands are higher than that of a_1-type bands. Furthermore, the intensities of both a_1-type and b_2-type bands decrease as the increase of gap size from

curve a to d. The intensities decrease of a_1-type bands is ascribed to the reducing of EM enhancement effect, which is strongly dependent on the gap size. The chemical environment of the 4-ATP and the new electronic states between 4-ATP and AuAg alloy may also be affected by the gap size of the sandwich nanostructures. Xu et al. reported that reducing separation between the inner core and outer shell can increase both the surface plasmon coupling and the coupling resonance between the two shells.[218] Conversely, large gap does not benefit either the EM or CM enhancement effects.[218] In the Ag-ATP SERS spectrum, the intensities of a_1 modes at 1075 cm^{-1} and 1182 cm^{-1} are much higher than those of b_2 modes. The strong intensity of a_1 modes of 4-ATP adsorbed on the surface of Ag nanocubes is because the LSPR of the Ag nanocubes is close to the 514.5-nm laser excitation wavelength (Figure 5.10). By contrast, the LSPR of the sandwich structures is far from the laser excitation wavelength (Figure 5.7b). Hence, the EM enhancement effect in the sandwich structures should be weaker, which results in weak a_1 modes.

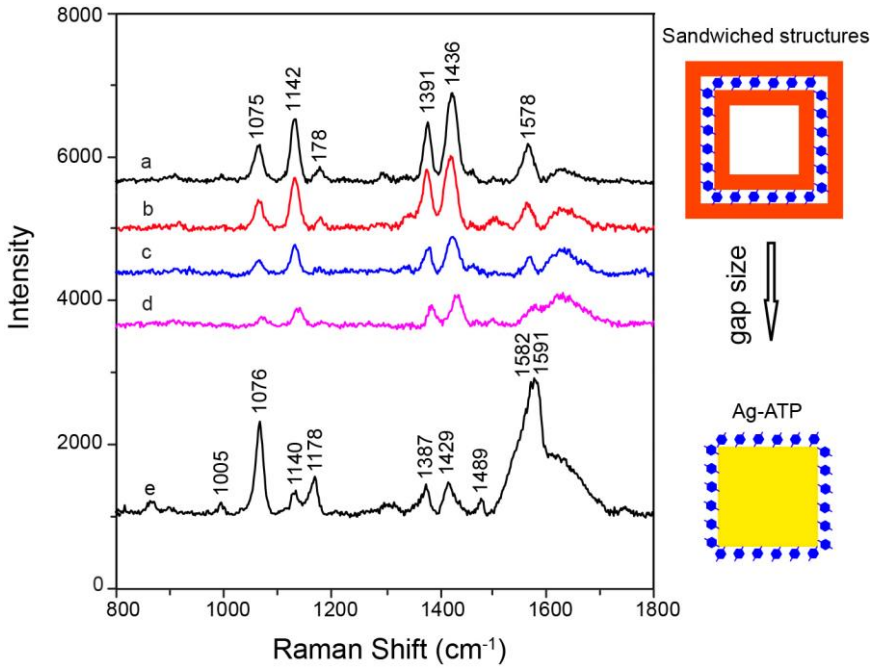

Figure 5.11 SERS spectra of 4-ATP located in the sandwich structures with different gap sizes (a) 1.2 nm, (b) 2.5 nm, (c) 8.0 nm, (d) 15.6 nm, and (e) adsorbed on the surface of Ag nanocubes. These SERS spectra were measured using 514.5 nm laser.

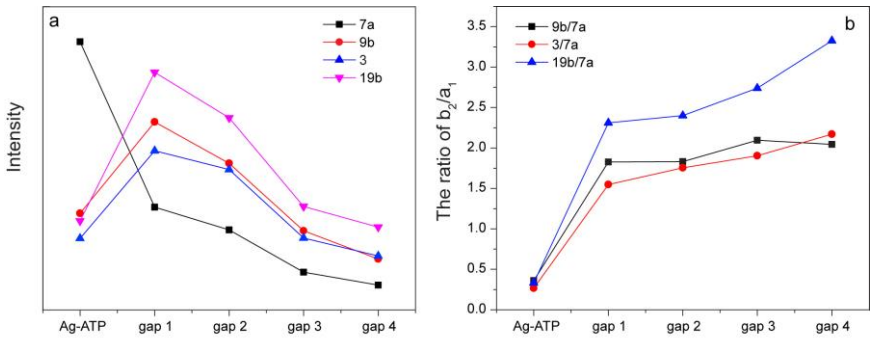

Figure 5.12 (a) Comparison of the intensities of a_1 and b_2 modes of 4-ATP adsorbed on Ag nanocubes and located in the sandwich structures with different gap sizes and (b) the ratio of b_2 modes to a_1 mode.

It is also found that the intensities of b_2 modes acquired from sandwich structures, especially from the sandwich structures with 1.2 nm, 2.5 nm gap sizes are higher than those obtained from Ag-ATP. It reflects that the b_2 modes

of 4-ATP are selectively enhanced when 4-ATP is located in sandwich structures relative to on the surface of Ag nanocubes. It was reported that the selective enhancement of b_2 vibrational modes of 4-ATP was caused by the CM effect.[198,206,208,219] As the EM effect cannot be isolated during the study of CM effect, one alternative way is to minimize the EM effect at the extreme.[206,208,213] Zhou et al. previously demonstrated that Au-PATP-Ag assembled sandwich structure provided much larger enhancement of b_2 modes than individual Au or Ag nanoparticles under 1064 nm excitation laser because of the tunnelling charge transfer effect.[206] The other alternative to exclude the EM effect is to use the intensity ratio of b_2/a_1 modes to value CM enhancement.[205] In order to clearly display the CM effect in the Au/Ag@ATP@Au/Ag sandwich structures, that the normalized intensities of b_2 modes by 7a mode are shown in Figure 5. 12b. It is found that the normalized intensities of b_2-type band from Au/Ag@ATP@Au/Ag sandwich structures are larger than those of Ag-ATP. This result may indicate that the CM enhancement effect from sandwich nanostructures is more obvious relative to that from Ag NCs.

To further evaluate the SERS enhancement effect of the sandwich structures, we also acquired the SERS spectra of these sandwich structures with 637-nm laser and compared their SERS activities with Ag nanocubes, Au/Ag hollow boxes, and Au/Ag@Ag nanoparticles. Figure 5.13 shows the SERS spectra of 4-ATP molecules embedded in the interior gaps of sandwich structures, adsorbed on the surface of Ag nanocubes and Au/Ag hollow boxes,

and embedded at the interface of Au/Ag@Ag nanoparticles, respectively. Compared with other nanostructures as SERS substrate, the sandwich structures with interior gaps gives largest SERS signals of 4-ATP including a_1 and b_2-type bands. Figure 5.14a shows, with 637-nm laser, the intensities of both a_1 and b_2-type bands of 4-ATP embedded in the interior gaps of sandwich structures decrease with the increase of gap size. It is also clearly shown that, for sandwich structures, the normalized intensity of b_2-type bands relative to a_1-type bands are larger than those of 4-ATP adsorbed on the surface of Ag NCs (Figure 5.14b). However, the selective enhancement of b_2-type bands obtained at 637 nm is less than that obtained at 514.5 nm. It may indicate that the shorter laser wavelength facilitates the CM effect. Shin et al. also reported that the CM enhancement coefficient was larger at shorter laser wavelength.[205]

The relative SERS EFs of 4-ATP embedded in the interior gaps of the sandwich structures is calculated based on the corresponding modes of 4-ATP adsorbed on the surface of Ag nanocubes (Figure 5.15). It shows a clear trend that the EFs of b_2-type bands are much larger than those of a_1-type bands when both 514.5-nm and 637-nm lasers are as excitation light source. Furthermore, the EFs of each b_2-type bands decrease when the increase of interior gap size. It also clearly shows that the EFs of each band obtained with 637-nm laser are much larger than those obtained with 514.5-nm laser, indicating that the excitation wavelength can affect both the EM and CM enhancement effects.

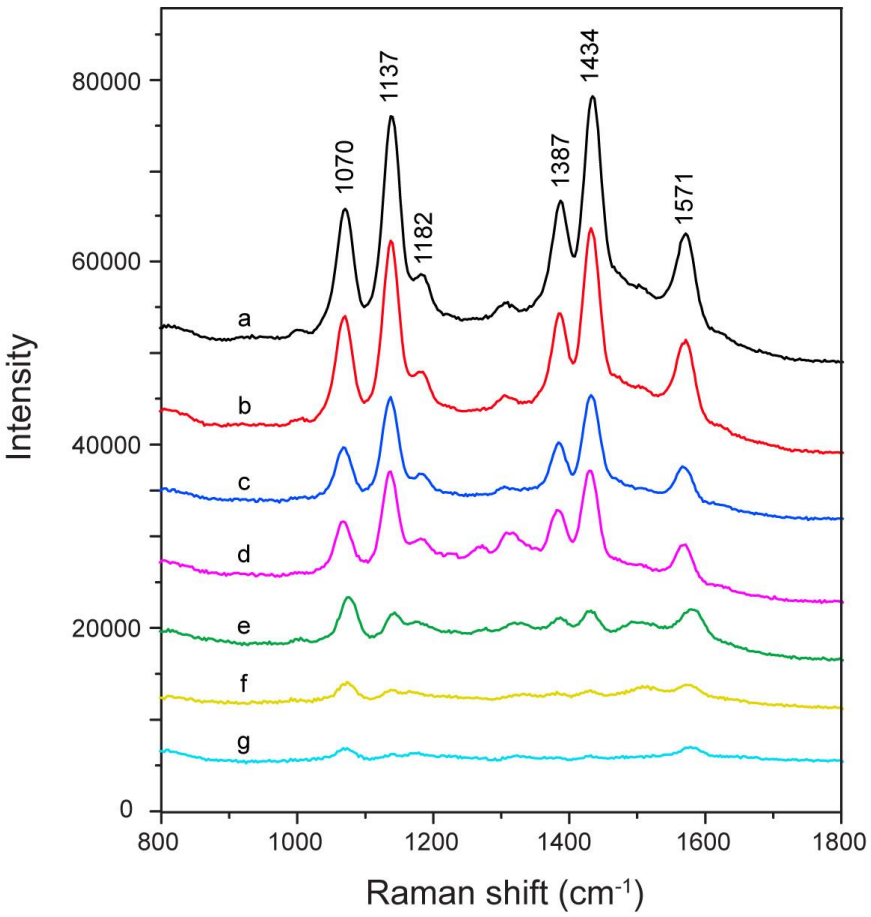

Figure 5.13 SERS spectra of 4-ATP embedded in the interior gaps of sandwich structures with gap sizes of (a) 1.2 nm, (b) 2.5 nm, (c) 8.0 nm, (d) 15.6 nm, (e) 4-ATP adsorbed on the surface of Ag nanocubes, (f) 4-ATP adsorbed on the surface of Au/Ag hollow boxes, (g) 4-ATP embedded at the interface of Au/Ag@Ag nanoparticles, respectively. These SERS spectra were acquired with 637-nm laser.

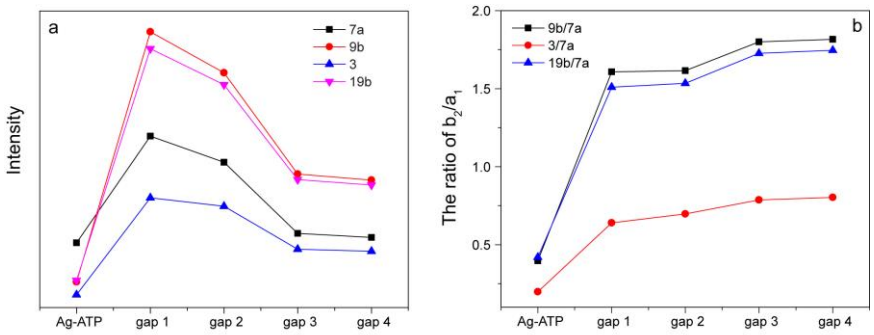

Figure 5.14 (a) Intensities of a_1 and b_2 modes of 4-ATP adsorbed on Ag nanocubes and located in that sandwich structures with different gap sizes; (b) the intensity ratios of b_2 modes to a_1 mode.

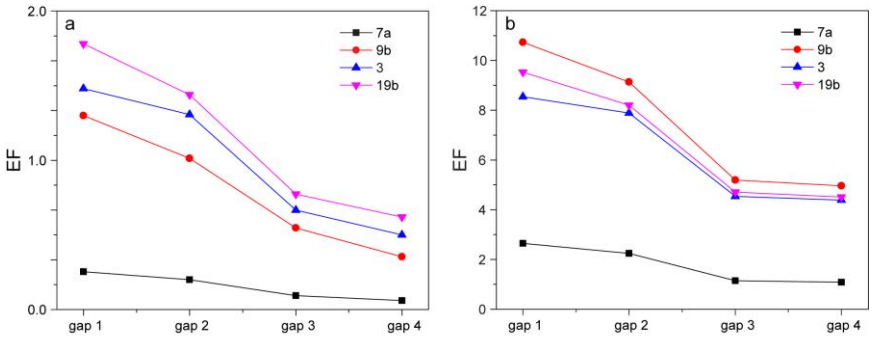

Figure 5.15 Relative enhancement factors (EFs) of sandwich structures with different gap sizes based on SERS spectra acquired (a) at 514.5 nm and (b) at 637 nm.

5.3 Conclusion

In conclusion, the sandwich structures with four different interior gap sizes and the presence of 4-ATP in these interior gaps have been obtained for SERS study. The SERS spectra acquired with 514.5- and 637-nm lasers show that the intensities of a_1 and b_2 modes decrease as the increase of interior gap size of the sandwich structures. Furthermore, the b_2 modes of 4-ATP in the sandwich structures are selectively enhanced relative to that of 4-ATP

adsorbed on the surface of Ag nanocubes. The results indicate that the CM effect of the sandwich structures is larger than that of Ag NCs.

Chapter 6. Tailoring the End Facets of Au@Ag Core-shell Penta-twinned Nanorods

6.1 Introduction

Bimetallic core-shell nanocrystals have attracted tremendous attention in recent years because these structures have shown unique electronic, catalytic and optical propertie.[134,220-225] Among all bimetallic nanostructures, those made of Au and Ag are of particular interest because of their superior plasmonic properties.[61,128,135,139,226-228] For instance, Sönnichsen and coworkers discovered a "plasmonic focusing" phenomenon of Au@Ag core-shell nanorods which show reduced ensemble plasmon line width relative to bare Au nanorods.[27] In a recent study, Wang *et al.* demonstrated that Au@Ag core-shell nanorods made of Au core and Ag shell can have four plasmon modes including longitudinal dipolar, transverse dipolar, and two octupolar modes.[26] These interesting plasmonic properties make Au@Ag nanostructures ideal candidates for applications such as enhancement of nonlinear effects,[229,230] sensing,[231] and light-guiding.[232]

To date, a few synthetic approaches based on co-reduction[233] or seed-mediated growth[234] have been developed for the preparation of Au@Ag core-shell nanostructures. Seed-mediated growth as a powerful synthetic method has been widely used to obtain bimetallic core-shells with various shapes.[234,235] In seed-mediated synthesis, shape-control can be achieved by

selecting different nanostructured templates as the seeds, using different capping ligands, or tuning the reaction kinetics. While the use of capping ligands can direct the growth mode of the second metal on the surface of the metal template *via* controlling the binding strength of the ligands on different facets,[235-238] tuning kinetic parameters can also achieve shape-selective effect since the nucleation and growth of metallic atoms on a core nanocrystal seed is susceptible to the rate at which the atoms are generated by reducing a precursor.[64,133,135,224,235]

Despite a few shapes of Au@Ag bimetallic nanorods having been synthesized *via* seed-mediated approach,[26,56,133-136,233,239-241] there is lack of systematic study on controlling the morphology of the tips. Typically, the tips of Au@Ag nanorods are bounded by low-energy {111} or {100} facets.[235] It should be noted that the morphology of the tips may substantially affect the plasmonic and catalytic properties of the nanorods. For example, sharp tips of Au/Ag nanostructures have strong implication on surface enhanced Raman scattering (SERS) due to much-enhanced electromagnetic field at sites with small curvature when the nanostructures are interacting with electromagnetic wave.[242] In addition, when plasmonic nanostructures are used as waveguide for optical-electronic devices, the transmission and reflection determined by the geometry of end facets can significantly affect the device performance.[243] In catalytic applications, tips with high-energy facets such as {110} may find improved activity due to higher density of dangling bonds compared to {111} and {100} facets[244]. Here, we present a systematic study of tuning the end

facets of Au@Ag nanorods by varying the capping agents and reaction kinetics using Au bipyramids (BPs) as the template. Unlike Au nanorods, only until recently have Au BPs been used as template to synthesize bimetallic core-shell nanostructures. In a work by Wang *et al*., they employed Au BPs to direct the growth of Ag and Pd to form core-shell nanorods with sharp tips.[134] Tréguer-Delapierre and coworkers also employed Au BPs as template to coat a thin layer of Ag and studied the morphology of the resulting core-shell nanorods via 3D reconstruction.[241] Multiple-twined Au BPs as templates in seeded-growth favor preferential deposition of the second metal on their various facets because they are enclosed by both high-index {*h*11} (*h*=5-7) side facets and low-index {111} end facets.[244,245] The high-index facets will be firstly occupied by the atoms of the second metal because they possess more active sites such as atomic steps, edges, and kinks.[246] In this work, using Au BPs as the growth seeds, Au@Ag bimetallic nanorods with three different morphologies have been obtained by reducing $AgNO_3$ with ascorbic acid (AA). As illustrated in Figure 6.1, at low pH with cetyl-trimethylammonium bromide (CTAB) as the capping agent, flat-tipped Au@Ag nanorods terminated with {110} end facets are obtained. It is worth noting that Au@Ag penta-twinned nanorods with flat {110} end facets have been rarely reported. In the second case, when CTAB is replaced with cetyl-trimethylammonium chloride (CTAC), Au@Ag nanorods with tips bounded by {111} facets are formed. When the reaction is conducted at high pH, dumbbell-shaped Au@Ag nanorods are generated with either CTAB or CTAC as the capping agent.

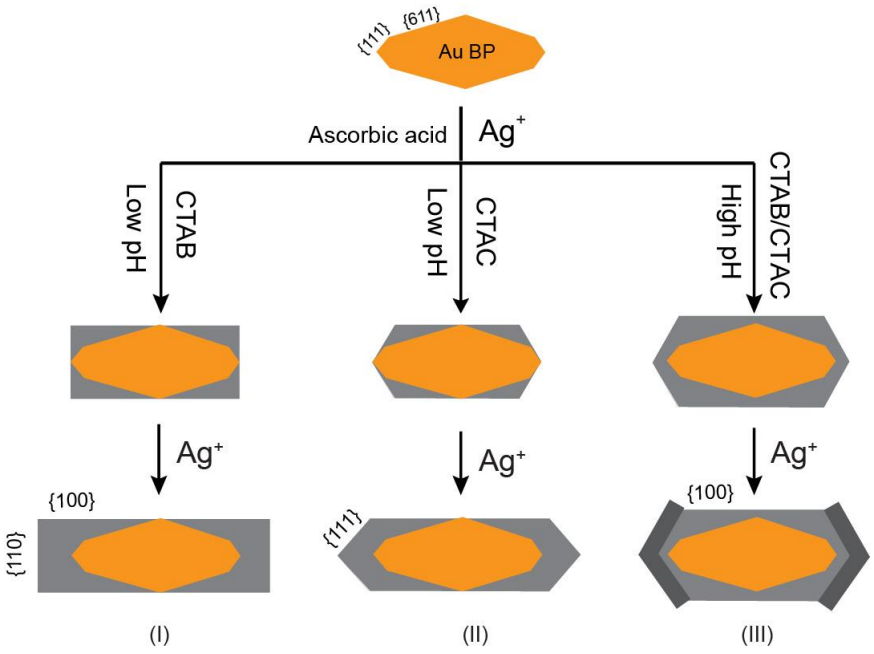

Figure 6.1 Au@Ag Bimetallic core-shell nanorods with tunable end facets obtained by selecting different capping agents and controlling the reduction rate of Ag at different pHs.

6.2 Results and Discussion

6.2.1 Synthesis of Au BPs

Au BPs were prepared according to a reported method.[148] The Au BPs were with good quality and its average length and diameter were 83 nm and 39 nm, respectively (as shown in Figure 6.2). In this work, the penta-twinned Au BPs instead of Au nanorods were used as seeds for the deposition of Ag because their side surfaces are bounded with high index facets. These high index facets will provide more active sites to facilitate the deposition of Ag atoms.

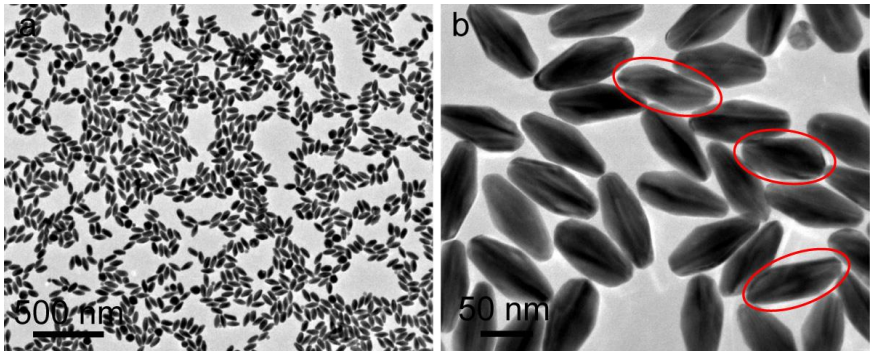

Figure 6.2 TEM images of Au BPs.

6.2.2 Au@Ag nanorods with flat tips

After coating with Ag at pH=4.9 in the presence of CTAB, the Au BPs were converted to Au@Ag core-shell penta-twinned nanorods terminated with flat end facets (Figure 6.3a-b, Figure 6.4). Transmission electron microscopy (TEM) images clearly show that within each nanorod a Au BP is located in the center. In some Au@Ag nanorods, Au BPs are not symmetrically located in the center of the nanorods. This may be because these Au BPs are truncated to form an asymmetric shape (as indicated in Figure 6.2b). This core-shell structure was also confirmed with energy dispersive X-ray spectroscopy (EDX) analysis, which revealed that each nanorod is composed of a Au core and a symmetrical Ag shell (Figure 6.3c-e). The width of the nanorods is 41 nm, which is the similar with the equatorial width of the Au BPs. The average length of the Au@Ag nanorods is 113 nm when 50 μL of 4 mM $AgNO_3$ was used for coating. This length is 30 nm longer than that of the Au BP templates. Longer nanorods can be obtained by adding more $AgNO_3$ to the growth

solution (Figure 6.5). The dimensions of the Au BPs and representative Au@Ag nanorods are shown in Table 6.1.

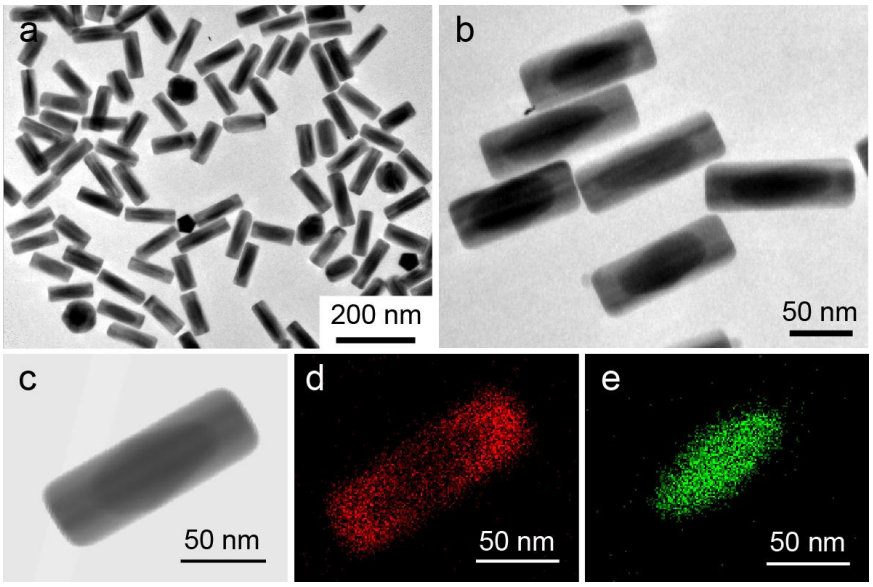

Figure 6.3 (a-b) TEM images of Au@Ag bimetallic nanorods with flat tips obtained using CTAB as the capping agent at pH=4.9 after adding 50 μL of 4 mM $AgNO_3$. (d-e) EDX elemental mapping of Ag (red) and Au (green) for the Au@Ag nanorod shown in (c).

Table 6.1 The size comparison between three types of Au@Ag nanorods and Au BPs template when 50 μL $AgNO_3$ was added.

	Length (nm)	Width (nm)
Au BPs	83	39
Au@Ag nanorods with flat tips	113	41
Au@Ag nanorods with sharp tips	135	40
Au@Ag nanorods with dumbbell-shape	103	61

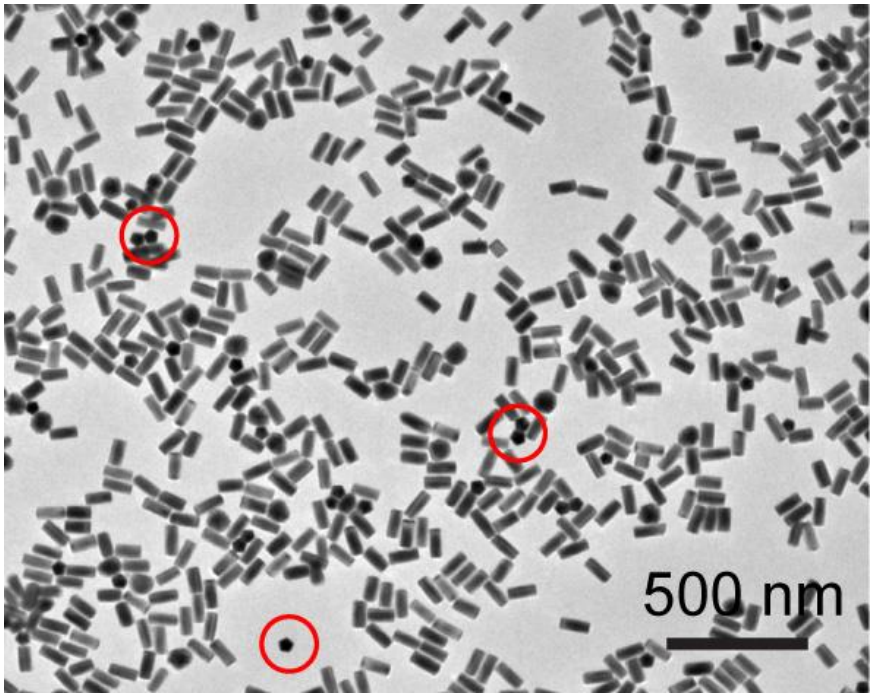

Figure 6.4 Low magnification TEM image of Au@Ag nanorods with flat end facets obtained at pH=4.9 after adding 25 µL of 4 mM $AgNO_3$ with CTAB as the capping agent. The circles indicate nanorods perpendicular to the TEM grid.

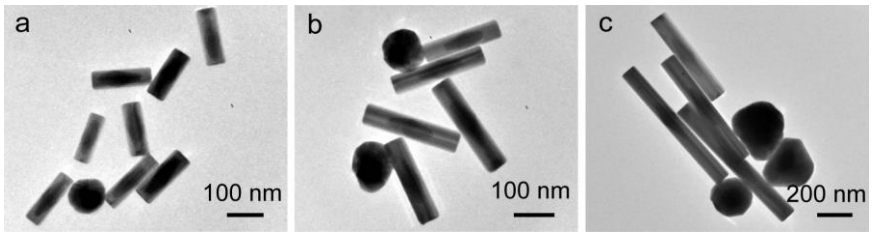

Figure 6.5 TEM images of Au@Ag nanorods with flat end facets obtained at pH=4.9 after adding (a) 50 µL, (b) 100 µL, and (c) 160 µL of 4 mM $AgNO_3$ with CTAB as the capping agent.

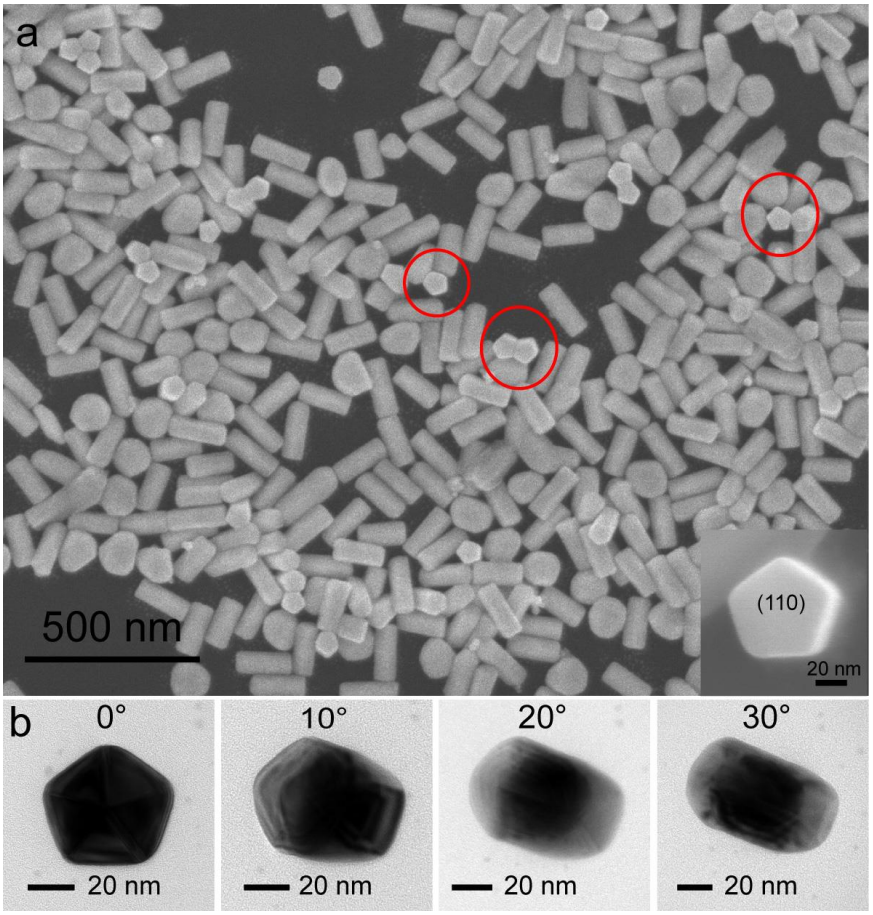

Figure 6.6 (a) FESEM image of Au@Ag bimetallic nanorods with flat tips. Inset shows an enlarged tip of a nanorod. (b) TEM images of a nanorod standing on copper grid at a series of tilting angles.

To confirm the crystal facets of the Au@Ag nanorods, further scanning electron microscopy (SEM) and TEM analyses were conducted. As shown in Figure 6.6a, SEM images of the nanorods indicate that most of the nanorods are terminated with flat end facets that are perpendicular to the growth direction of the Au BPs. As Au BPs should have a five-folder twined structure with a growth direction of <110>,[228,234,247-249] the flat end facets of the Au@Ag nanorods should be {110}. To further confirm the end facet of the flat-tipped nanorods, HRTEM image and selected area electron diffraction

pattern (SAED) were obtained. As shown in Figure 6.7b, the lattice planes along the growth direction of the nanorod show a d-spacing of 0.14 nm, matching well with the (220) plane of fcc Ag. The SAED recorded from one end of the nanorod also exhibits <110> growth direction (Figure 6.7c). Based on the results including SEM, HRTEM, and SAED, it can be concluded that the end facets of the flat-tipped nanorods are {110}. Although Ag nanowires with tips showing slight {110} truncation have been observed before,[250] Ag nanostructures with fully developed {110} facets have not been reported. This is because {110} facets are not thermodynamically favored due to the high surface energy relative to {111} and {100} facets.[251] The appearance of [7] end facets of the Au@Ag nanorods may be attributed to the strong affinity of CTAB to {110} facets.[235,236]

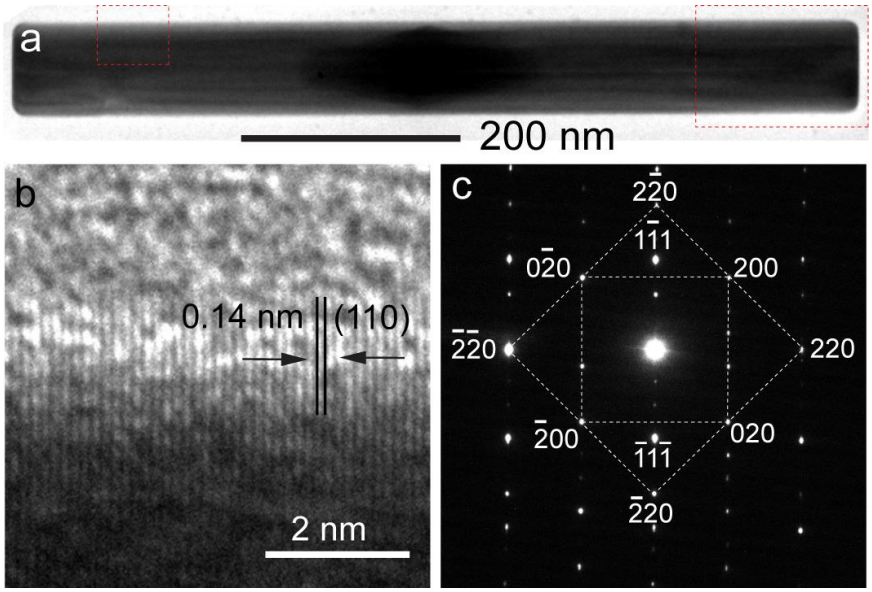

Figure 6.7 (a) TEM image of Au@Ag bimetallic nanorods with flat tips. (b) HRTEM images of (a). The measured d-spacing of 0.14 nm matches with that of (100) plane of Ag. (c) SAED of one end of nanorods, indicating its growth direction is <110>.

As indicated in Figure 6.6a and Figure 6.4 in, a few pentagon-shaped structures can also be found on the SEM and TEM images. This is because these nanorods were imaged along their longitudinal axis. Stand-alone nanorods with longitudinal axis perpendicular to TEM substrate have also been observed (Figure 6.6b). By tilting the TEM grid at different angles (0-30 degrees), it was found that the projection of the nanorod is elongated, indicating that the pentagonal shapes observed on the TEM and SEM images are indeed one-dimensional nanorods. The possibility for these nanorods to stand upright on the TEM grid further confirms their flat tips. In addition, the five-fold twinned cross-section can be clearly revealed for these nanorods (Figure 6.6a inset and Figure 6.6b). This phenomenon also indicates that the flat-tipped Au@Ag bimetallic nanorods are penta-twinned structure with {110} end facets.

The structural evolution of the Au@Ag nanorods was followed when different amounts of $AgNO_3$ were added to the growth solution. In the beginning, the growth of Ag mainly took place on the side surface of the Au BP template (Figure 6.8a-b). With the deposition of more Ag, the tapered side facets gradually became parallel to the growth axis of the rods (Figure 6.8c-d). The side facets of Au BPs should be high-index {*h*11}, where *h* typically ranges from 5~7;[241,244,247] while the end facets of the Au BPs are {111}.[148,244] The deposition of Ag atoms preferentially starts at the high-index side facets due to their high surface energy and low stability. With more Ag deposited on the sides, {100} facets parallel to the growth axis became the dominating side

surface until the disappearance of the high-index facets (Figure 6.8e-f). In the meantime, deposition of Ag on the low-index {111} facets at the tips of the BPs also occurred, but at a much lower rate. This resulted in the development of {110} facets. Once nascent {110} facets appeared, they could be stabilized by CTAB.[235] Eventually, the two ends of the nanorods were bounded entirely by {110} facets perpendicular to the growth axis; while the sides of the nanorods were enclosed by {100} facets parallel to the growth axis (Figure 6.8g-h). After this stage, if more Ag ions were added, the Ag atoms continued to deposit only on the {110} end facets -- the nanorods grew in length but maintained a constant width (Figure 6.5; Figure 6.8i-j).

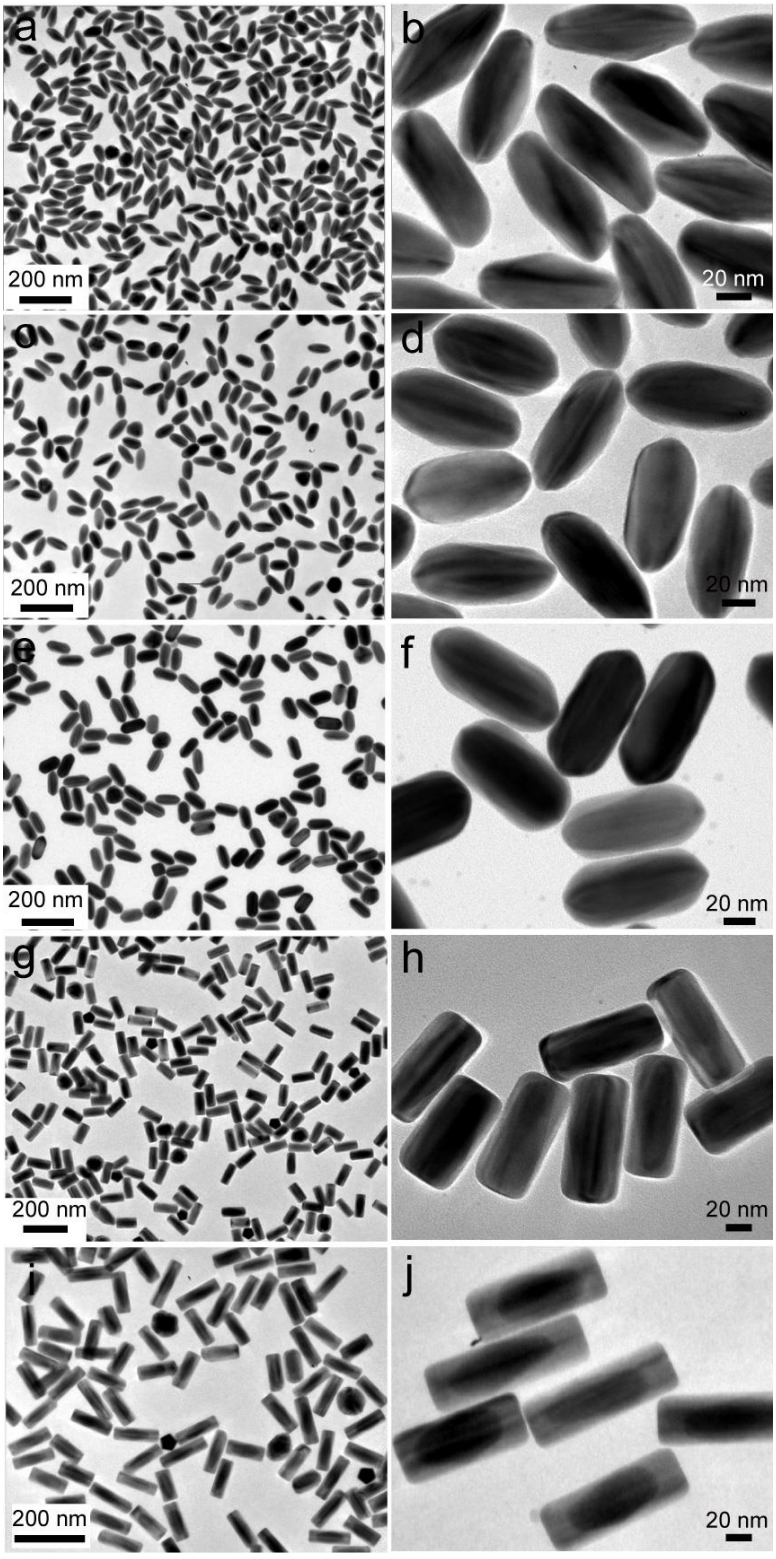

Figure 6.8 TEM images of Au@Ag bimetallic nanorods obtained by adding different volumes of 4 mM $AgNO_3$ with CTAB as the capping agent at pH = 4.9: (a, b) 5 µL, (c, d) 10 µL, (e, f) 15 µL, (g, h) 25 µL and (i, j) 50 µL.

6.2.3 Au@Ag nanorods with sharp tips

We further investigated the effect of capping agent on the deposition of Ag on Au BPs. When CTAB was replaced with CTAC while other reaction conditions were kept the same, a different morphology of the nanorods was observed. In this case, the resulting Au@Ag bimetallic nanorods were not terminated with flat {110} end facets. Instead, they showed truncated tips mainly bounded by {111} facets (Figure 6.9; Figure 6.10), a morphology more commonly found for five-fold twined Ag nanorods.[56] The Au@Ag nanorods obtained by adding different amounts of $AgNO_3$ with CTAC as the capping ligand are shown in Figure 6.11. In the beginning, when 5-10 μL of 4 mM $AgNO_3$ solution was added, a similar deposition process of Ag was observed in comparison with the case when CATB was used as the capping ligand. At these stages, Ag atoms preferentially deposited on the high-index side surfaces; while the {111} end facets were further developed (Figure 6.11a-d). After adding 20 μL of Ag precursor, penta-twinned Au@Ag nanorods with sharp tips were formed. These nanorods are terminated with {111} end facets and {100} side facets (Figure 6.11e-f). The presence of {111} end faces and the <110> growth direction of the nanorods can be confirmed from the HRTEM images and SAED as shown in Figure 6.12. When 25-50 μL of $AgNO_3$ was injected to the growth solution, the nanorods started to grow along the longitudinal direction while the width remained the same, indicating that at this stage the deposition of Ag took place on the {111} end facets

(Figure 6.11g-j). In the meantime, the tips of the nanorods became truncated, possibly due to the appearance of {110} facets.[250]

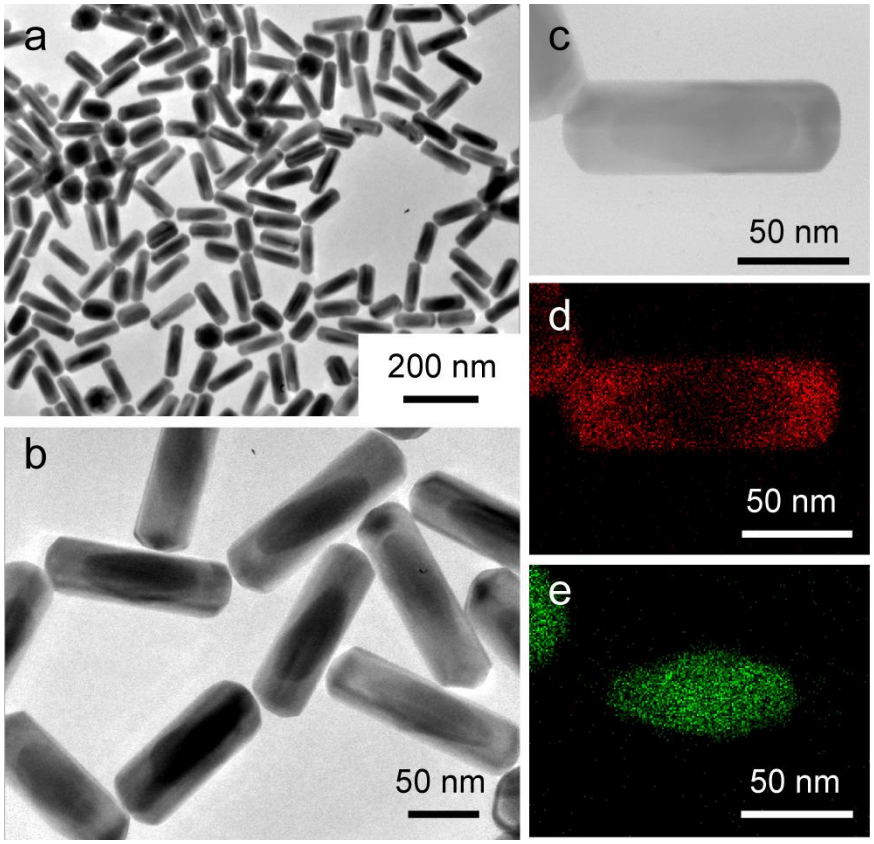

Figure 6.9 (a-b) TEM images of Au@Ag bimetallic nanorods with truncated {111} end facets obtained at pH=4.9 with CTAC as the capping agent after adding 50 μL 4 mM $AgNO_3$; (d-e) EDX elemental mapping of Ag (red) and Au (green) for the Au@Ag nanorod shown in (c).

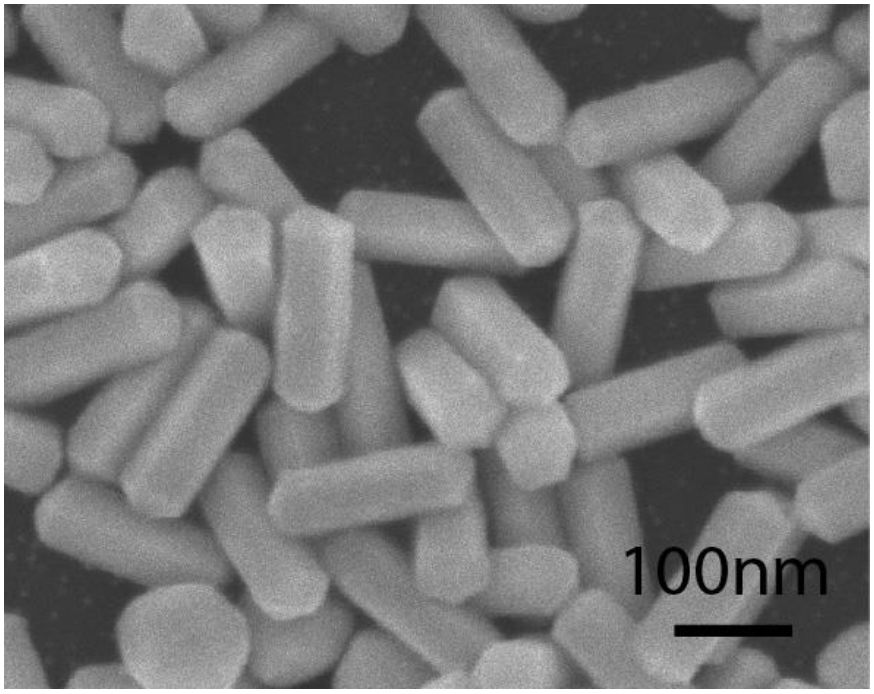

Figure 6.10 SEM image of Au@Ag nanorods with {111} end facets obtained at pH=4.9 after adding 50 μL of 4 mM $AgNO_3$ with CTAC as the capping agent.

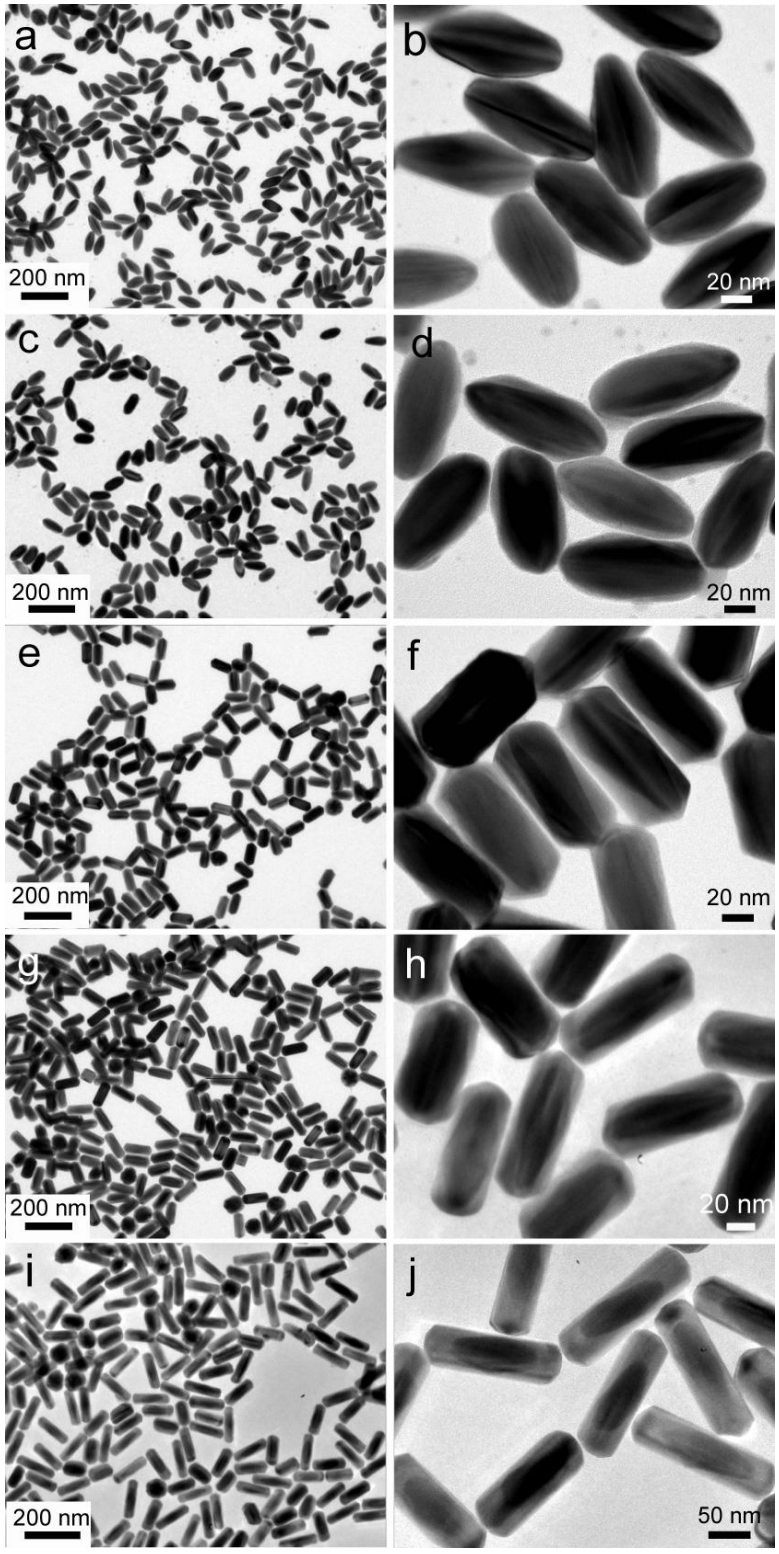

Figure 6.11 TEM images of Au@Ag bimetallic nanorods obtained at pH = 4.9 by adding different volumes of 4 mM $AgNO_3$ with CTAC as the capping agent: (a, b) 5 µL, (c, d) 10 µL, (e, f) 20 µL, (g, h) 25 µL and (i, j) 50 µL.

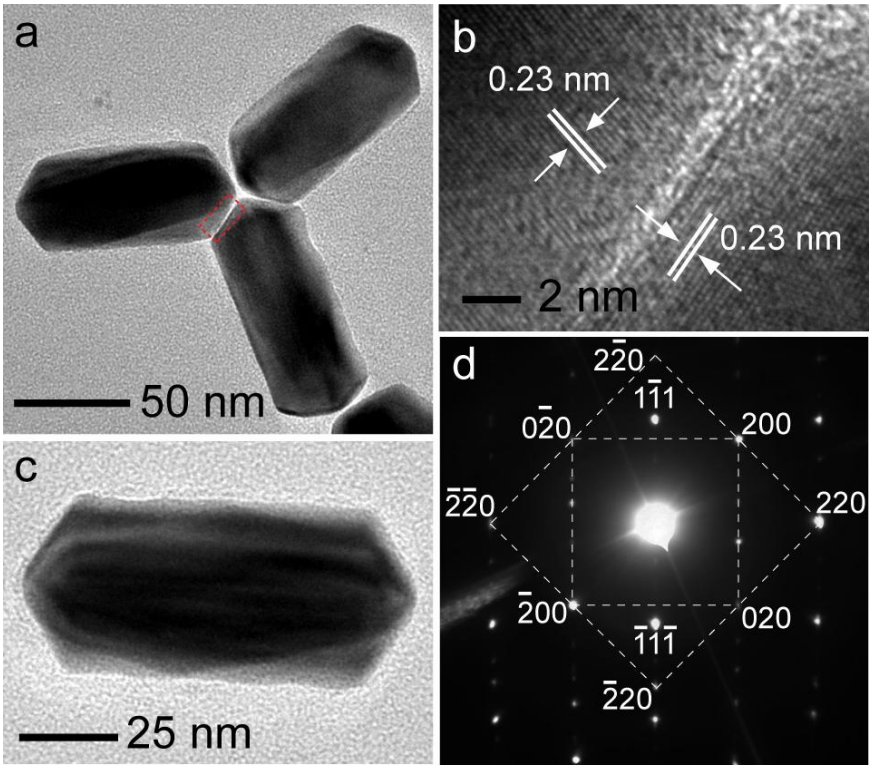

Figure 6.12 Au@Ag nanorods with {111} end facets obtained at pH=4.9 after adding 20 μL of 4 mM $AgNO_3$ with CTAC as the capping agent. (a) TEM of three adjacent nanorods. (b) HRTEM for the area indicated in (a). The measured *d*-spacing of 0.23 nm can be indexed as (111) plane of Ag. (c-d) TEM of a nanorod and its corresponding selected area electron diffraction pattern (SAED), which indicates the <110> growth direction of the nanorod.

6.2.4 Au@Ag nanorods with dumbbell-shape

The shape of the Au@Ag nanorods can also be tuned by controlling the pH of the growth solution. When the molar ratio of AA and NaOH was increased from 1:1 to 1:2.1, the pH of the growth solution changed from 4.9 to 10.0. At this pH, when 50 μL of $AgNO_3$ solution was used to coat the Au BPs with CTAB as the capping agent, the resulting Au@Ag nanorods showed a width of 61 nm, 19 nm larger than that of the Au BPs (Figure 6.14e-f). With more $AgNO_3$ introduced to the growth solution, the nanorods continued to

grow in width. This is in stark contrast with the nanorods obtained at low pH, in which case the width of the rods was maintained at a constant. In addition, overgrowth of Ag on the tips of the nanorods was also observed. This growth mode led to the formation of dumbbell-shaped Au@Ag nanorods (Figure 6.13, Figure 6.14). The same morphological evolution was also found when CTAB was replaced with CTAC at pH=10 (Figure 6.15), indicating that at high pH, Ag deposition occurred on both the end and the side facets no matter CTAC or CTAB was used as the capping agent. It is worth noting the Chang *et al.* also obtained dumbbell-shaped Au@Ag nanorods when the coating of Ag on Au templates was performed at high pH, although in their work, Au nanorods instead of BPs were used as the seeds.[66]

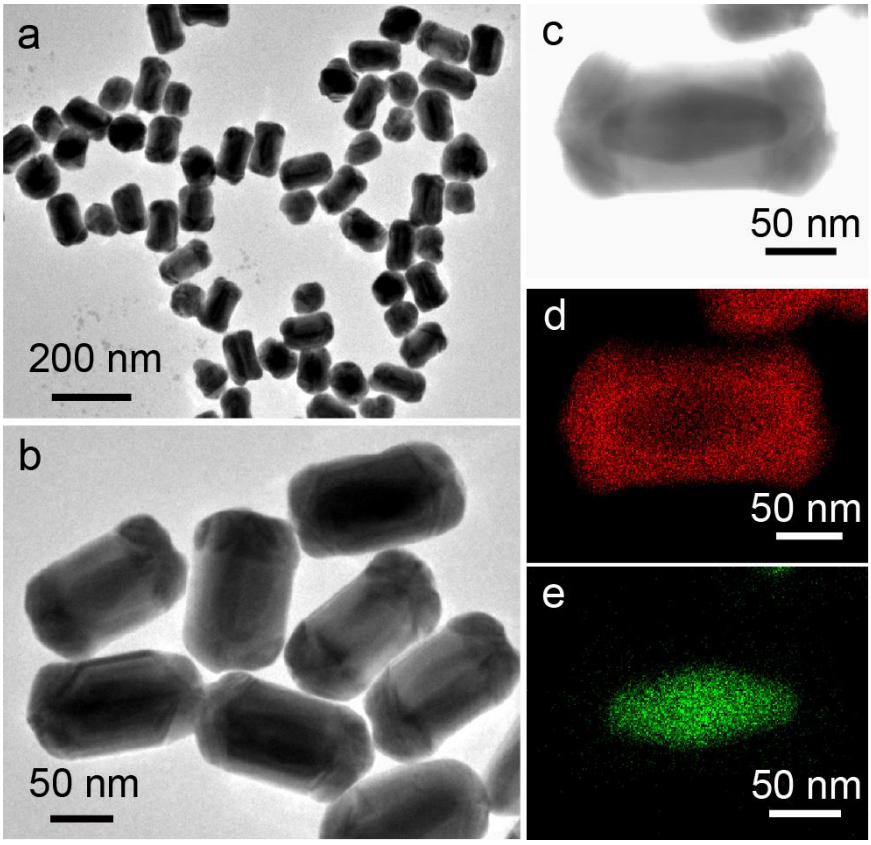

Figure 6.13 (a-b) TEM images of Au@Ag bimetallic nanorods with dumbbell shape obtained at pH=10 with CTAB as the capping agent after adding 200 μL 4 mM $AgNO_3$. (d-e) EDX elemental mapping of Ag (red) and Au (green) for the Au@Ag nanorods shown in (c).

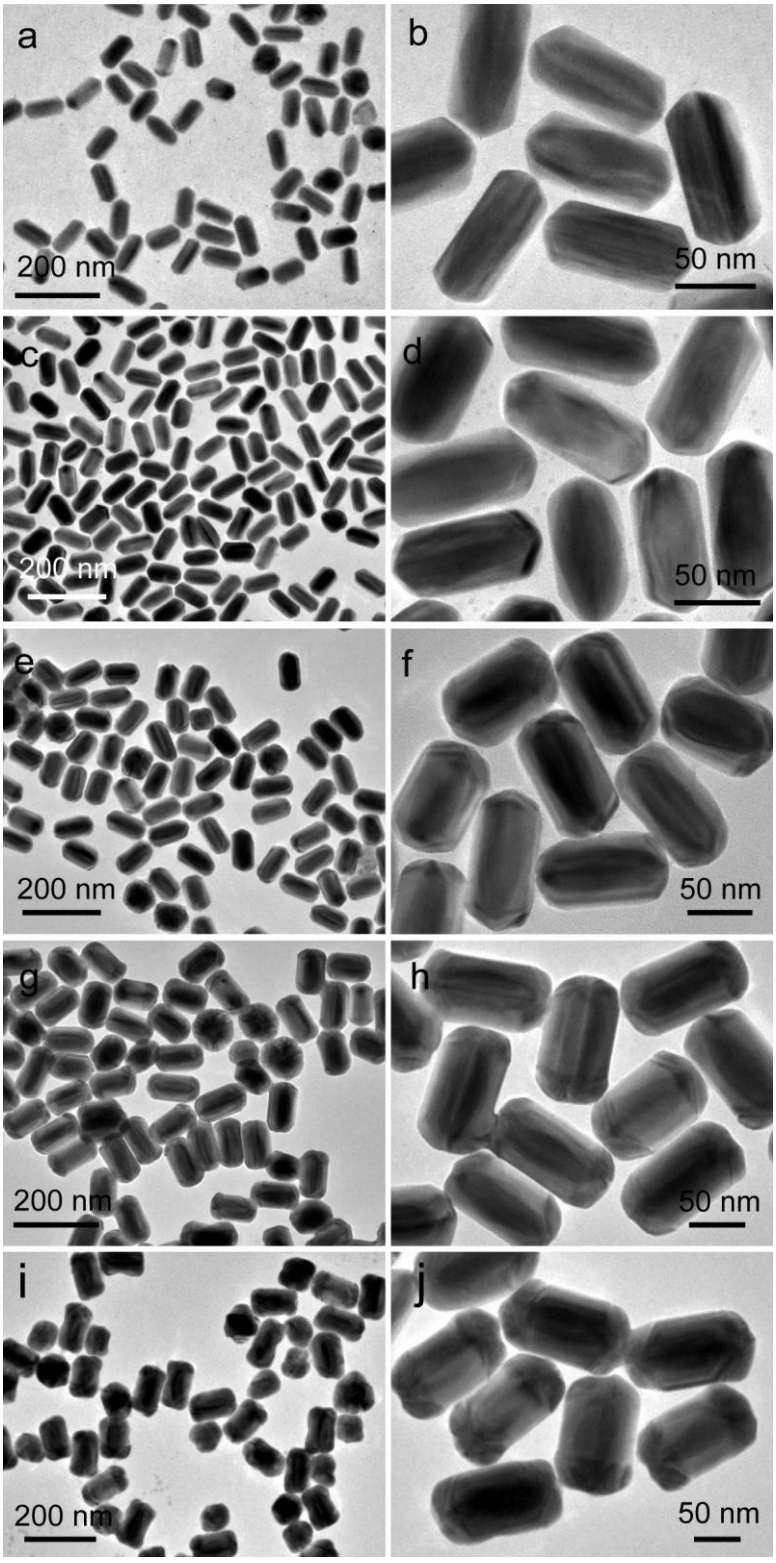

Figure 6.14 TEM images of Au@Ag bimetallic nanorods obtained at pH = 10 by adding different volumes of 4 mM $AgNO_3$ with CTAB as the capping agent: (a, b) 15 µL, (c, d) 25 µL, (e, f) 50 µL, (g, h) 100 µL, and (i,j) 200 µL.

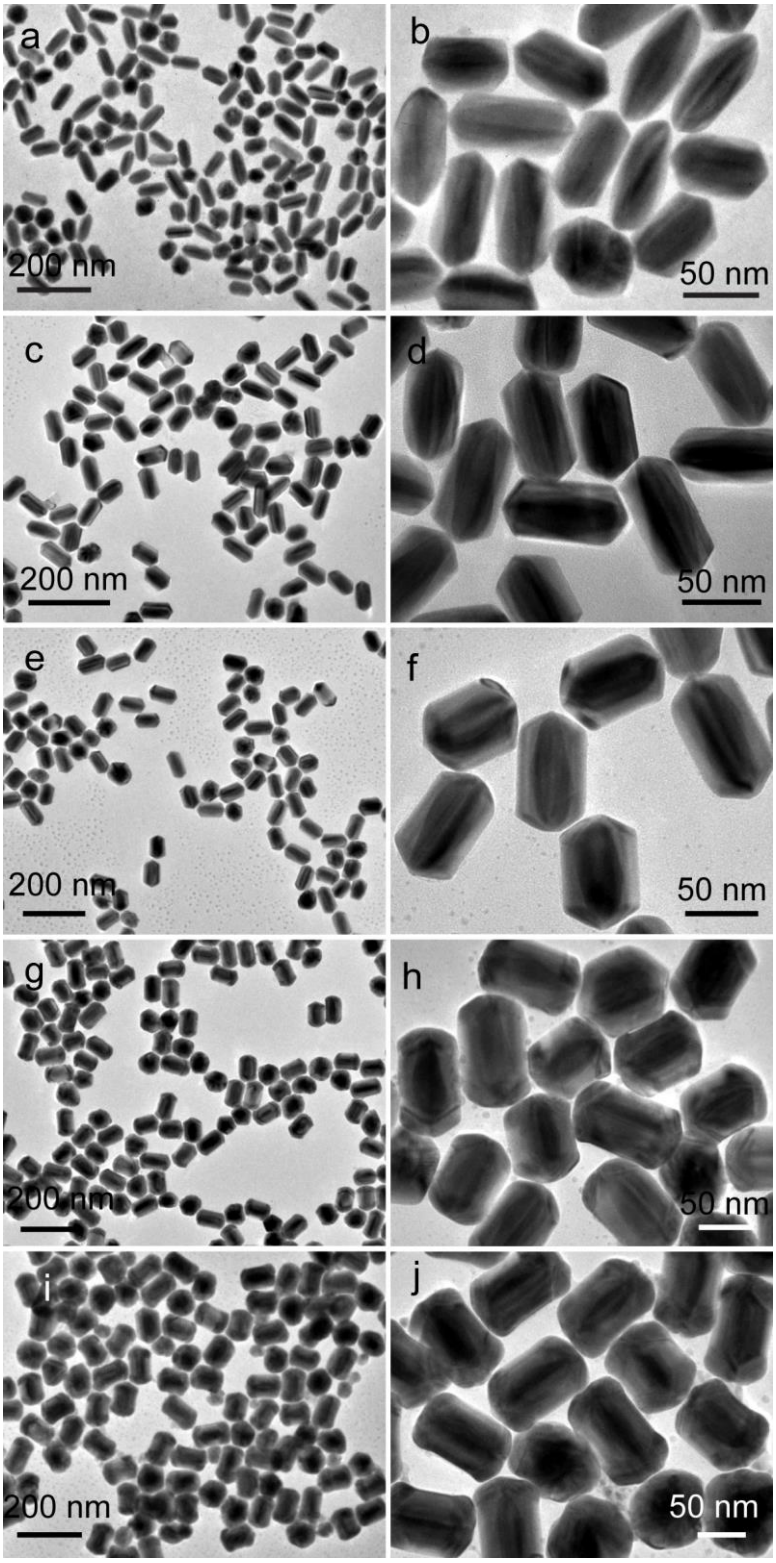

Figure 6.15 TEM images of Au@Ag bimetallic nanorods obtained at pH = 10 by adding different volumes of 4 mM $AgNO_3$ with CTAC as the capping agent: (a, b) 15 µL, (c, d) 25 µL, (e, f) 50 µL, (g, h) 100µL, (i, j) 200 µL.

6.2.5 Growth mechanism

It is well known that capping agents can affect the growth rate of different facets via surface-selective binding.[252] In addition to capping agent, pH value also plays an important role in controlling the shape of the nanorods since it changes the reduction rate of Ag^{+}.[65,135] Together, the combined effects of capping agents and reaction kinetics offer a powerful means to control the shape of the resulting Au@Ag core-shell nanorods. Based on the above observations, the following growth mechanism for the Au@Ag nanorods is proposed.

Firstly, at low pH with CTAB as the capping agent, the deposition of Ag takes place on both the high-index side facets and the {111} end facets. The lateral growth of Ag on the sides leads to the formation of {100} side facets, which are typically found for penta-twinned nanorods (Figure 6.16a, stage I). Once the {100} facets are fully developed, the deposition of Ag on the sides stops due to the formation of an effective surfactant barrier *via* the adsorption of the hydrophobic ends of the CTAB molecules.[253] On the other hand, the deposition of Ag on the {111} end facets causes the disappearance of the {111} facets (Figure 6.16a, stage II). It should be noted that at the early stage, the deposition of Ag on the sharp tips of the Au BPs is largely hindered. This is possibly attributed to the exposed {110} facets at the tips that bind more strongly with CTAB than {111} facets. This growth mode results in the appearance of {110} facets at the ends. Once the nanorods are terminated with flat {110} end facets, further addition of Ag only leads to the deposition on the

{110} end facets, but not on the {100} side faces (Figure 6.16a, stage III). This result indicates that the {110} end facets may have weaker binding with CTAB compared to the {100} side facets.

Secondly, at low pH with CTAC instead of CTAB as the capping agent, the deposition of Ag at early stage takes place only on high-index side facets, leading to the formation of {100} side surfaces. However, no apparent deposition on the {111} end facets occurs. This lateral deposition causes the development of the {111} end facets until the whole nanorod tip is terminated completely with {111} facets (Figure 6.16b stage II, Figure 6.10e-f). This is different from the case when CTAB is used as the capping agent that leads to the formation of {110} end facets. The different growth modes may be ascribed to the binding strength of Br and Cl species on Ag surface. In a study by Illas *et al.*, they performed density functional theory (DFT) calculations on the interactions between halogens and metal low-index facets.[254] They found that the adsorption energies E_{ads} of Br on Ag {111}, {110}, and {100} facets are -2.83, -2.93, and -3.00 eV, respectively, meaning that the adsorption of Br on Ag surface follows the sequence of {100}>{110}>{111}. That explains the preferential stabilization of {100} and {110} facets over {111} when CTAB is used as the capping agent. For Cl, the adsorption energies on Ag {111}, {110}, and {100} facets are -3.09, -3.12, and -3.24 eV, respectively. Although the adsorption energies of Cl follow the same order as Br on the three facets, the difference in E_{ads} between {111} and {110} facets is very small. Therefore, similar surface stabilization of Ag {110} and {111} by Cl should be expected.

In addition halide ions, CTA+ cationic head groups can also adsorb on the negative layer of halide counterions due to electrostatic attraction. Therefore, the adsorption of both CTA+ cations and halide anions may have synergistic effect on controlling the shape of the Au@Ag nanorods.[255] Meanwhile, when the higher surface energy of {110} than {111} is also considered, one would expect that the {111} facets should be more stable in this case. This explains why sharp tips of Au@Ag nanorods terminated with {111} facets dominate when CTAC is used as the capping agent. After this stage, further addition of $AgNO_3$ causes the growth of Au@Ag nanorods only along the longitudinal direction due to stronger affinity of CTAC with {100} than {111} facets (Figure 6.16b, stage III). When large quantity of $AgNO_3$ is added, truncation of the nanorod tips starts to appear.

Thirdly, at high pH, the reducing power of ascorbic acid is significantly increased, causing much faster reduction of Ag^+ ions.[68] In this case, the preferential growth of Ag on different facets is largely cancelled out. Therefore, the deposition of Ag occurs on both the side and end facets simultaneously when sufficient $AgNO_3$ is added to the growth solution (Figure 6.16c, stage II). In the end, due to the enhanced deposition rate of Ag and less protected surface of the nanorods, the overgrowth of Ag gives rise to the dumbbell-shaped nanorods (Figure 6.16c, stage III).

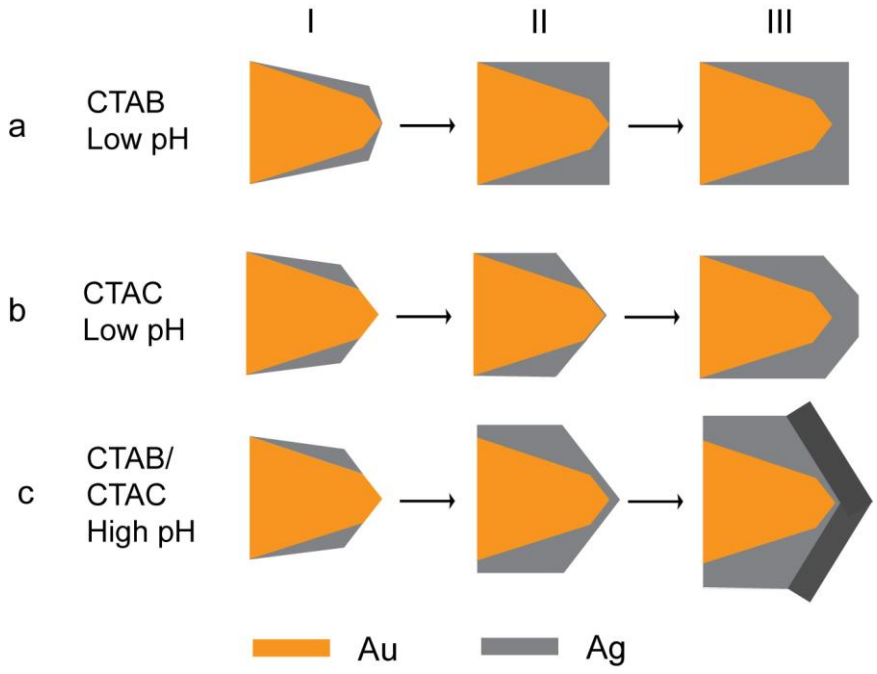

Figure 6.16 The schematic morphological evolution of the tips for the Au@Ag nanorods with increasing amount of $AgNO_3$ at different reaction conditions: (a) at pH=4.9 and with CTAB as capping agent, (b) at pH=4.9 and with CTAC as capping agent, (c) at pH=10 and with CTAB or CTAC as the capping agent.

6.2.6 SPR spectra of the Au@Ag bimetallic nanorods

The UV-vis extinction spectra of the Au BPs and the derived Au@Ag bimetallic nanorods are shown in Figure 6.17. The spectrum of Au BPs (black line) shows two localized surface plasmon resonance (LSPR) peaks: a strong peak at 680 nm (peak 1) and a weak one at 515 nm (peak 2), corresponding to the longitudinal and transverse plasmon bands of the Au BPs, respectively.[26,134] For Au@Ag nanorods obtained at low pH with CTAB as the capping agent (Figure 6.17a), peak 1 blue-shifted when the volume of $AgNO_3$ was increased from 5 μL to 15 μL, corresponding to the Au@Ag nanostructures shown in Figure 4a-f. This is caused by the decrease of

effective aspect ratio due to the preferential deposition of Ag atoms on the lateral sides at the initial stage.[241,256] After this stage, when more $AgNO_3$ was added to the reaction, peak 1 shifted to longer wavelengths (850 nm corresponding to 50 μL of $AgNO_3$). This is because Au@Ag nanorods grew in length once the lateral facets became flat. During this process, the transverse SPR peak slightly shifted from 515 nm to the blue end and eventually overlapped with a new and strong peak at shorter wavelength of 430 nm. This new peak is ascribed to the transverse plasmon band of the Ag shell.[235] Figure 6.17b shows the spectra of Au@Ag nanorods terminated with sharp tips obtained with CTAC as the capping agent - these spectra are similar to those in Figure 6.17a, confirming the similar morphological evolution processes of the Au@Ag structures in these two cases. At high pH with CTAB as the capping agent, the UV-vis spectra (Figure 6.17c) show that the SPR peak corresponding to the longitudinal mode blue-shifted at the beginning stages up to 50 μL $AgNO_3$ was added into solution. This blue shift is due to the decreased aspect ratio caused by growth in width of the nanorods. Afterwards, when more $AgNO_3$ solution (100 and 200 μL) were added into the growth solution, this peak red-shifted slightly. However, the peak was still located at shorter wavelength compared to that of Au BPs. This is due to the growth of Ag shell on both the side and end facets, leading to smaller aspect ratios of the Au@Ag nanorods than that of the Au BPs.

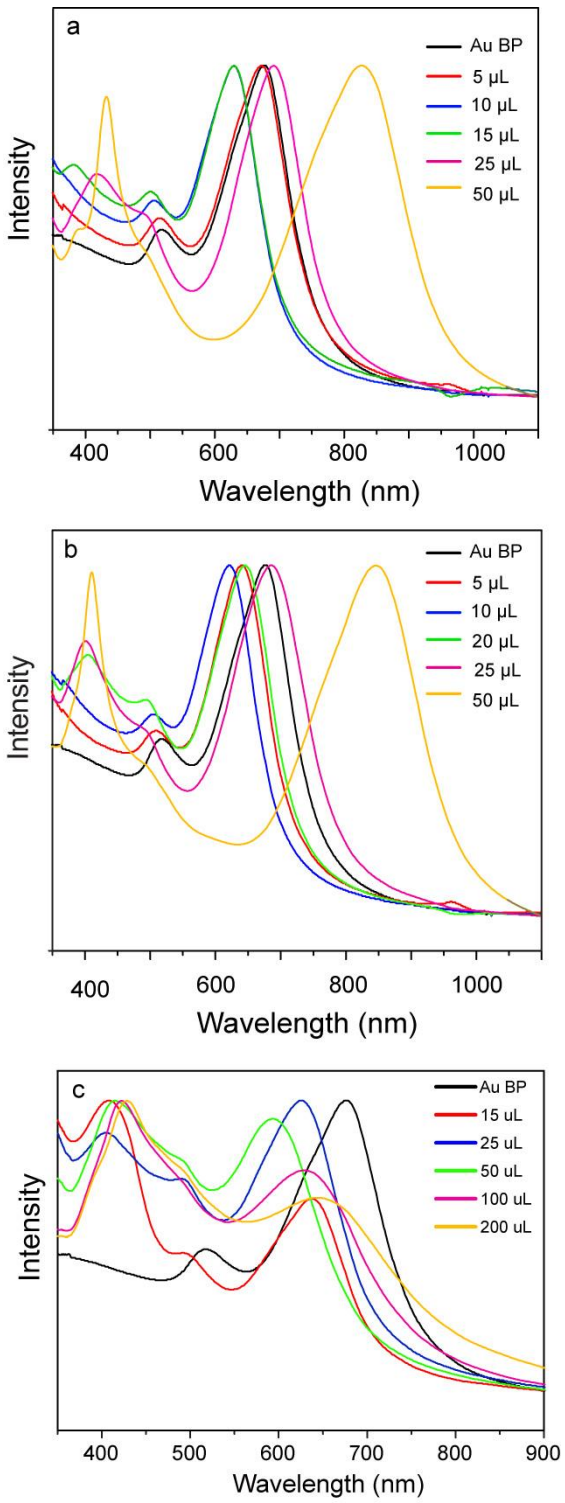

Figure 6.17 UV-Vis extinction spectra of Au@Ag nanorods obtained by adding different amounts of $AgNO_3$ (a) at pH=4.9 with CTAB as the capping agent; (b) at pH=4.9 with CTAC as the capping agent; and (c) at pH=10 with CTAB as the capping agents.

6.3 Conclusion

In conclusion, bimetallic Au@Ag nanorods terminated with different facets at the tips have been synthesized using Au BPs as the template by reducing $AgNO_3$ with AA. Tuning the end facets was achieved *via* changing the capping agents and pH of the reaction solution. It is worth noting that Au@Ag penta-twinned nanorods fully terminated with {110} end facets are firstly reported. These results demonstrate that the selection of capping agent and tuning kinetic parameters are powerful means to control the shape of Au@Ag bimetallic nanorods.

Chapter 7. Conclusions and Future Work

7.1 Conclusions

In conclusion, bimetallic nanocrystals with controllable shapes, including Pt/Ag porous and hollow structures, Au/Ag sandwich structures with probe molecules trapped in their interior gaps, and Au@Ag core-shell nanorod with thermodynamic unstable facets, have been synthesized with different growth methods including modified galvanic replacement reaction (GRR) and seeded growth. The shape-controlled synthesis of Pt/Ag and Au/Ag bimetallic nanostructures advances our current understanding on the growth mechanism of bimetallic nanostructures. Among these bimetallic nanostructures, Pt/Ag porous and hollow nanostructures and Au/Ag sandwich structures exhibit enhanced electrochemical performance and enhanced SERS EFs, respectively. The key results and findings of this thesis are summarized as follows:

1. Pt/Ag bimetallic hollow and porous nanostructures including nanoboxes, dimers, multimers, and popcorn-shaped nanoparticles were synthesized via tailored GRR. Ag NCs were employed as template to reaction with K_2PtCl_4 in the presence of HCl. When HCl and PVP were introduced into the dispersion of Ag NCs, Pt/Ag nanoboxes with smooth and continuous walls are obtained. However, if only HCl was added, the reaction gave Pt/Ag heterodimers or multimers depending on the amount of HCl added to the Ag NCs. If the mixture of HCl and

K_2PtCl_4 solution was injected into the solution of Ag NCs, Pt/Ag popcorn-shaped particles were formed. The results suggested that HCl was a crucial factor for shape-controlled synthesis of these Pt-Ag bimetallic nanostructures. The effect of HCl may be for twofold: (i) to facilitate the precipitation of AgCl, (ii) to regulate the reaction kinetic and thus the number of deposition sites. The AgCl precipitation grew on the surface of Ag NCs and acted as a removable secondary template for the deposition of Pt. The number of deposition sites for AgCl can be effectively tailored by controlling the amount of HCl added to the Ag NCs or by introducing PVP to the reaction. Once HCl was added to the reaction gradually, a different morphology of the resulting Pt/Ag structures was observed because of a different deposition pattern of AgCl. In the tailed GRR, the precipitation of AgCl was purposely facilitated with the help of HCl, and consequently the AgCl islands served as in situ generated secondary templates for the deposition of Pt. This finding is contrary to previous study since byproduct AgCl was always regarded as obstacle for the GRR reaction.[257] As expected, these Pt/Ag nanostructures exhibited large surface area and enhanced electrocatalytic performance for methanol oxidation reaction due to the presence of large void space and porous walls. It was found that both Pt/Ag popcorns and dimers exhibited higher MOR activities and better stability than commercial Pt/C. The first contribution of this study may provide promising electrocatalytic catalysts for the fuel cell industry. The second contribution of this study is that the GRR method has been

successfully extended to the preparation of bimetallic dimers, multimers, and popcorn-shaped nanostructures based on this strategy. This is because that the shape of the hollow nanostructures obtained via GRR usually resembles that of the sacrificial templates.

2. Au/Ag@ATP@Au/Ag sandwich structures were synthesized via modified GRR. Firstly, Au/Ag single-walled hollow boxes were synthesized by using Ag NCs as templates to react with $HAuCl_4$. These hollow boxes were then attached with a monolayer of 4-ATP. The resulting Au/Ag@ATP nanoparticles were used as seeds for the deposition of Ag shell. Interior gap within the sandwich structure was generated in the second-round GRR. The 4-ATP molecules trapped in the interior gaps were employed as probe molecules for SERS study. Four gap sizes, 1.2, 2.5, 8.0 and 15.6 nm, were obtained by using four thicknesses of Ag shells as the template to react with different amounts of $HAuCl_4$ in the second-round GRR. These sandwich structures with controlled gap sizes were used for SERS investigation. The SERS spectra acquired with 514.5-nm laser show that the intensities of a_1-type bands of 4-ATP are much lower than that of 4-ATP adsorbed on the Ag surface. This is because the 514.5-nm excitation wavelength is closer to the LSPR of Ag nanocubes than those of the sandwich structures. At this laser wavelength, a_1- and b_2-type bands of 4-ATP located in sandwich structures increased with the decrease of the interior gap size. Furthermore, the b_2-type bands of 4-

ATP embedded in the sandwich structures were selectively enhanced relative to those of 4-ATP adsorbed on the Ag nanocubes. For SERS spectra obtained with 637-nm laser, the intensities of a_1 and b_2 modes of sandwich structures are much higher than those in the spectra of other nanostructures, including Ag nanocubes, Au/Ag hollow boxes, and Au/Ag@ATP@Ag particles. Meanwhile, the intensities of a_1 and b_2 modes in the SERS spectra of the sandwich structures also decrease when the increase of the interior gap size. Furthermore, the intensities ratios of b_2/a_1 modes obtained at 514.5-nm and 637-nm laser wavelength indicate that the CM effect of the sandwich structures is larger than that of Ag nanocubes.

3. Au@Ag core-shell nanorods with tunable end facets were obtained by coating Au bipyramids (BPs) with Ag. The resultant nanorods exhibit a penta-twinned crystal structure with tips terminated with either {110} or {111} facets. The control over the end facets was achieved by varying the capping agents and tuning the reduction rate of Ag. Specifically, at slow reduction of Ag, Au@Ag nanorods with flat {110} ends facets were formed with cetyl-trimethylammonium bromide (CTAB) as the capping agent. If CTAB was replaced with cetyl-trimethylammonium chloride (CTAC), Au@Ag nanorods with tips terminated with {111} facets were obtained. However, at high reduction rate of Ag, with either CTAB or CTAC as the capping agent, dumbbell-shaped Au@Ag nanorods were formed. The morphological

evolution of the nanorods in each case was closely followed and a growth mechanism was proposed. It was found that the types of capping agents and pH value played paramount role to affect the deposition of Ag atoms and control the final shapes of the nanocrystals. It is worth pointing out that Au@Ag pentagonal nanords fully bounded with {110} facets are different with the previous results, in which the pentagonal nanorods are bounded with {111} end tips.[128,136]

7.2 Future work

It has been confirmed that bimetallic nanocrystals possess distinct and advantageous properties in various applications, such as electrochemical catalysis and sensing. Due to their excellent properties, the shape-selective synthesis of bimetallic nanocatalysts is developing rapidly. Based on the experiment results obtained, the discussion presented and conclusion drawn from this thesis, some potential areas for future investigation related to the shape control of bimetallic nanostructures are highlighted below.

1. For the development of proton exchange membrane fuel cells (PEMFCs), the sluggish kinetics of ORR can be improved by using Pt-based bimetallic catalysts. Recently, a tremendous interest has been developed on the synthesis of Pt-based bimetallic electrocatalysts with well-defined morphologies (see examples in section 2.3 of Chapter 2). Our preliminary results showed that Pt/Ag porous and hollow

nanostructures obtained in Chapter 4 exhibited an enhanced electrocatalytic performance on MOR. These bimetallic nanostructures may also be a good candidate for the ORR due to their hollow interiors, porous and thin walls. Therefore, the electrocatalytic performance of resultant Pt/Ag bimetallic nanostructures towards ORR should be investigated in order to fully understand the electrocatalytic performance of these Pt/Ag porous and hollow bimetallic nanostructures.

2. GRR is a simple and facile approach to generate noble metal nanostructures with hollow interiors using different active metal templates and less active metal salts. So far, few studies were reported on manipulating the reaction kinetics of GRR to control the shapes of bimetallic hollow nanostructures. In Chapter 4, the modified GRR was used to obtain Pt/Ag hollow boxes, dimers, multiple dimers and popcorns through tuning the kinetic reaction parameters. This strategy may also be applicable to other bimetallic systems such as Au/Ag, Pd/Ag, and Pd/Pt.

3. Size-tunable interior gap formed within a single plasmonic nanostructure may offer reliable EF and facilitate the understanding of enhancement mechanism of SERS. Sandwich nanostructures Au/Ag@ATP@Au/Ag with controlled interior gaps obtained in Chapters 5 are promising SERS-active substrates for the SERS application. To further investigate the SERS enhancement mechanism,

a single particle of SERS study on Au/Ag@ATP@Au/Ag sandwich structures is needed.

4. As very few works were reported on the colloidal synthesis of nanostructures with interior gaps. The synthetic strategy reported in Chapter 5 may also be applied to prepare Au/Ag@molecule@Au/Ag sandwich structures with other probing molecules instead of 4-ATP. The amount of probing molecules embedded in sandwich structures can be detected via UV-Vis spectrophotometer. During the UV-Vis measurement, the adsorption intensity of probe molecules should not be disturbed by the change of reaction factors, such as pH. The known amount of probing molecules should lead to more reliable calculation of SERS EFs.

5. Metal materials and shapes may influence the EF of SERS. The core effect on the SERS EFs is rarely studied. To better understand the enhancement mechanism of SERS, the synthetic strategy in chapter 5 may also be applied to the preparation of other sandwich structures with the forms of metal@molecule@Au/Ag with interior gap and metal@molecule@metal in order to study the effect of cores with different materials and shapes on the SERS enhancement. The systematic studies of these sandwich structures are desirable for the fundamental study of SERS.

6. Au@Ag nanorods terminated with {110} facets, which are thermodynamic unstable facets, were prepared via a combination of

seed-mediated growth and kinetic control in Chapters 6. For further investigation of the growth mechanism proposed in Chapter 6, Au seeds with different facets can be used to synthesize Au@Ag core-shell nanostructures that exhibit thermodynamically unfavorable morphologies. In addition, this strategy may also be used to the preparation of other bimetallic core-shell structures such as Au@Pd.

Reference

(1) Rao, C. N. R.; Kulkarni, G. U.; Thomas, P. J.; Edwards, P. P. *Chemical Society Reviews* **2000**, *29*, 27.

(2) Rao, C. N.; Ramakrishna Matte, H. S.; Voggu, R.; Govindaraj, A. *Dalton transactions* **2012**, *41*, 5089.

(3) Chen, H.; Shao, L.; Li, Q.; Wang, J. *Chem Soc Rev* **2013**, *42*, 2679.

(4) Guo, S.; Wang, E. *Nano Today* **2011**, *6*, 240.

(5) Li, C.; Shuford, K. L.; Chen, M.; Lee, E. J.; Cho, S. O. *ACS Nano* **2008**, *2*, 1760.

(6) Li, L.; Larsen, A. H.; Romero, N. A.; Morozov, V. A.; Glinsvad, C.; Abild-Pedersen, F.; Greeley, J.; Jacobsen, K. W.; Nørskov, J. K. *The Journal of Physical Chemistry Letters* **2012**, *4*, 222.

(7) Burda, C.; Chen, X.; Narayanan, R.; El-Sayed, M. A. *Chemical reviews* **2005**, *105*, 1025.

(8) Narayanan, R.; El-Sayed, M. A. *Nano Letters* **2004**, *4*, 1343.

(9) Tian, N.; Zhou, Z.-Y.; Sun, S.-G.; Ding, Y.; Wang, Z. L. *Science* **2007**, *316*, 732.

(10) Xia, Y.; Xiong, Y.; Lim, B.; Skrabalak, S. E. *Angewandte Chemie International Edition* **2009**, *48*, 60.

(11) Xu, D.; Bliznakov, S.; Liu, Z.; Fang, J.; Dimitrov, N. *Angewandte Chemie International Edition* **2010**, *49*, 1282.

(12) Choi, S. I.; Lee, S. U.; Kim, W. Y.; Choi, R.; Hong, K.; Nam, K. M.; Han, S. W.; Park, J. T. *ACS applied materials & interfaces* **2012**, *4*, 6228.

(13) Yang, L.; Hu, C.; Wang, J.; Yang, Z.; Guo, Y.; Bai, Z.; Wang, K. *Chemical Communications* **2011**, *47*, 8581.

(14) Sun, Y.; Xia, Y. *Science* **2002**, *298*, 2176.

(15) Peng, Z.; Yang, H. *Nano Today* **2009**, *4*, 143.

(16) Grzelczak, M.; Perez-Juste, J.; Mulvaney, P.; Liz-Marzan, L. M. *Chem Soc Rev* **2008**, *37*, 1783.

(17) Cortie, M. B.; McDonagh, A. M. *Chemical reviews* **2011**, *111*, 3713.

(18) Gu, J.; Zhang, Y. W.; Tao, F. F. *Chem Soc Rev* **2012**, *41*, 8050.

(19) Wu, J.; Li, P.; Pan, Y. T.; Warren, S.; Yin, X.; Yang, H. *Chem Soc Rev* **2012**, *41*, 8066.

(20) Stamenkovic, V. R.; Fowler, B.; Mun, B. S.; Wang, G.; Ross, P. N.; Lucas, C. A.; Marković, N. M. *Science* **2007**, *315*, 493.

(21) Wu, J.; Qi, L.; You, H.; Gross, A.; Li, J.; Yang, H. *J Am Chem Soc* **2012**, *134*, 11880.

(22) Orendorff, C. J.; Sau, T. K.; Murphy, C. J. *Small* **2006**, *2*, 636.

(23) Jin, R.; Cao, Y.; Mirkin, C. A.; Kelly, K. L.; Schatz, G. C.; Zheng, J. G. *Science* **2001**, *294*, 1901.

(24) Sun, Y.; Wiley, B.; Li, Z.-Y.; Xia, Y. *Journal of the American Chemical Society* **2004**, *126*, 9399.

(25) Skrabalak, S. E.; Au, L.; Li, X.; Xia, Y. *Nat Protoc* **2007**, *2*, 2182.

(26) Jiang, R.; Chen, H.; Shao, L.; Li, Q.; Wang, J. *Adv Mater* **2012**, *24*, OP200.

(27) Becker, J.; Zins, I.; Jakab, A.; Khalavka, Y.; Schubert, O.; Sönnichsen, C. *Nano Letters* **2008**, *8*, 1719.

(28) Zhang, J.; Fang, J. *Journal of the American Chemical Society* **2009**, *131*, 18543.

(29) DeSantis, C. J.; Peverly, A. A.; Peters, D. G.; Skrabalak, S. E. *Nano Letters* **2011**, *11*, 2164.

(30) Zeng, J.; Zhu, C.; Tao, J.; Jin, M.; Zhang, H.; Li, Z. Y.; Zhu, Y.; Xia, Y. *Angew Chem Int Ed Engl* **2012**, *51*, 2354.

(31) Wang, C.; Hou, Y.; Kim, J.; Sun, S. *Angew Chem Int Ed Engl* **2007**, *46*, 6333.

(32) Wang, D.; Zhao, P.; Li, Y. *Sci Rep* **2011**, *1*, 37.

(33) Lim, B.; Yu, T.; Xia, Y. *Angew Chem Int Ed Engl* **2010**, *49*, 9819.

(34) Zeng, J.; Zhu, C.; Tao, J.; Jin, M.; Zhang, H.; Li, Z.-Y.; Zhu, Y.; Xia, Y. *Angewandte Chemie International Edition* **2012**, *51*, 2354.

(35) Yang, H. *Angew Chem Int Ed Engl* **2011**, *50*, 2674.

(36) Gu, J.; Zhang, Y.-W.; Tao, F. *Chemical Society Reviews* **2012**, *41*, 8050.

(37) Zhang, H.; Jin, M.; Xia, Y. *Chemical Society Reviews* **2012**, *41*, 8035.

(38) Jiang, H.-L.; Xu, Q. *Journal of Materials Chemistry* **2011**, *21*, 13705.

(39) Sun, Y.; Mayers, B. T.; Xia, Y. *Nano Letters* **2002**, *2*, 481.

(40) Hermans, S.; Raja, R.; Thomas, J. M.; Johnson, B. F. G.; Sankar, G.; Gleeson, D. *Angewandte Chemie International Edition* **2001**, *40*, 1211.

(41) Thomas, J. M.; Johnson, B. F. G.; Raja, R.; Sankar, G.; Midgley, P. A. *Accounts of Chemical Research* **2002**, *36*, 20.

(42) Sun, S.; Murray, C. B.; Weller, D.; Folks, L.; Moser, A. *Science* **2000**, *287*, 1989.

(43) Sun, S. *Advanced Materials* **2006**, *18*, 393.

(44) Zhu, C.; Zeng, J.; Tao, J.; Johnson, M. C.; Schmidt-Krey, I.; Blubaugh, L.; Zhu, Y.; Gu, Z.; Xia, Y. *Journal of the American Chemical Society* **2012**, *134*, 15822.

(45) Treguer, M.; de Cointet, C.; Remita, H.; Khatouri, J.; Mostafavi, M.; Amblard, J.; Belloni, J.; de Keyzer, R. *The Journal of Physical Chemistry B* **1998**, *102*, 4310.

(46) Mizukoshi, Y.; Okitsu, K.; Maeda, Y.; Yamamoto, T. A.; Oshima, R.; Nagata, Y. *The Journal of Physical Chemistry B* **1997**, *101*, 7033.

(47) Anandan, S.; Ashokkumar, M. In *Theoretical and Experimental Sonochemistry Involving Inorganic Systems*; Ashokkumar, M., Ed.; Springer Netherlands: 2011, p 151.

(48) Kan, C.; Cai, W.; Li, C.; Zhang, L.; Hofmeister, H. *Journal of Physics D: Applied Physics* **2003**, *36*, 1609.

(49) Anandan, S.; Grieser, F.; Ashokkumar, M. *The Journal of Physical Chemistry C* **2008**, *112*, 15102.

(50) Pan, H.-B.; Wai, C. M. *New Journal of Chemistry* **2011**, *35*, 1649.

(51) Srivastava, S.; Samanta, B.; Arumugam, P.; Han, G.; Rotello, V. M. *Journal of Materials Chemistry* **2007**, *17*, 52.

(52) Liu, H. B.; Canizal, G.; Schabes-Retchkiman, P. S.; Ascencio, J. A. *The Journal of Physical Chemistry B* **2006**, *110*, 12333.

(53) Zhang, H.; Jin, M.; Wang, J.; Li, W.; Camargo, P. H.; Kim, M. J.; Yang, D.; Xie, Z.; Xia, Y. *J Am Chem Soc* **2011**, *133*, 6078.

(54) Im, S. H.; Lee, Y. T.; Wiley, B.; Xia, Y. *Angewandte Chemie International Edition* **2005**, *44*, 2154.

(55) Im, S. H.; Lee, Y. T.; Wiley, B.; Xia, Y. N. *Angewandte Chemie-International Edition* **2005**, *44*, 2154.

(56) Sun, Y.; Mayers, B.; Herricks, T.; Xia, Y. *Nano Letters* **2003**, *3*, 955.

(57) Hong, J. W.; Lee, S. U.; Lee, Y. W.; Han, S. W. *J Am Chem Soc* **2012**, *134*, 4565.

(58) Jin, M.; Zhang, H.; Xie, Z.; Xia, Y. *Angew Chem Int Ed Engl* **2011**, *50*, 7850.

(59) Johnson, C. J.; Dujardin, E.; Davis, S. A.; Murphy, C. J.; Mann, S. *Journal of Materials Chemistry* **2002**, *12*, 1765.

(60) Ye, J.; Hutchison, J. A.; Uji-i, H.; Hofkens, J.; Lagae, L.; Maes, G.; Borghs, G.; Van Dorpe, P. *Nanoscale* **2012**, *4*, 1606.

(61) Liu; Guyot-Sionnest, P. *The Journal of Physical Chemistry B* **2004**, *108*, 5882.

(62) Kim, K.; Yoon, J. K.; Lee, H. B.; Shin, D.; Shin, K. S. *Langmuir* **2011**, *27*, 4526.

(63) Kim, K.; Yoon, J. K. *The Journal of Physical Chemistry B* **2005**, *109*, 20731.

(64) Desantis, C. J.; Peverly, A. A.; Peters, D. G.; Skrabalak, S. E. *Nano Lett* **2011**, *11*, 2164.

(65) DeSantis, C. J.; Sue, A. C.; Bower, M. M.; Skrabalak, S. E. *ACS Nano* **2012**, *6*, 2617.

(66) Huang, C.-C.; Yang, Z.; Chang, H.-T. *Langmuir* **2004**, *20*, 6089.

(67) Langille, M. R.; Zhang, J.; Mirkin, C. A. *Angew Chem Int Ed Engl* **2011**, *50*, 3543.

(68) Nikoobakht, B.; El-Sayed, M. A. *Chemistry of Materials* **2003**, *15*, 1957.

(69) Moskovits, M.; Srnová-Šloufová, I.; Vlčková, B. *The Journal of Chemical Physics* **2002**, *116*, 10435.

(70) Theiss, J.; Pavaskar, P.; Echternach, P. M.; Muller, R. E.; Cronin, S. B. *Nano Letters* **2010**, *10*, 2749.

(71) Fang, Y.; Seong, N.-H.; Dlott, D. D. *Science* **2008**, *321*, 388.

(72) Li, J. F.; Huang, Y. F.; Ding, Y.; Yang, Z. L.; Li, S. B.; Zhou, X. S.; Fan, F. R.; Zhang, W.; Zhou, Z. Y.; Wu de, Y.; Ren, B.; Wang, Z. L.; Tian, Z. Q. *Nature* **2010**, *464*, 392.

(73) Camden, J. P.; Dieringer, J. A.; Wang, Y.; Masiello, D. J.; Marks, L. D.; Schatz, G. C.; Van Duyne, R. P. *Journal of the American Chemical Society* **2008**, *130*, 12616.

(74) Xiong, Y.; Xia, Y. *Advanced Materials* **2007**, *19*, 3385.

(75) Xiong, Y.; McLellan, J. M.; Yin, Y.; Xia, Y. *Angewandte Chemie International Edition* **2007**, *46*, 790.

(76) Lim, B.; Xiong, Y.; Xia, Y. *Angewandte Chemie International Edition* **2007**, *46*, 9279.

(77) Aouani, H.; Navarro-Cia, M.; Rahmani, M.; Sidiropoulos, T. P. H.; Hong, M.; Oulton, R. F.; Maier, S. A. *Nano Letters* **2012**, *12*, 4997.

(78) Rahmani, M.; Lei, D. Y.; Giannini, V.; Lukiyanchuk, B.; Ranjbar, M.; Liew, T. Y. F.; Hong, M.; Maier, S. A. *Nano Letters* **2012**, *12*, 2101.

(79) Kinkhabwala, A.; Yu, Z.; Fan, S.; Avlasevich, Y.; Müllen, K.; Moerner, W. E. *Nature Photonics* **2009**, *3*, 654.

(80) Zou, S.; Schatz, G. C. *Chemical Physics Letters* **2005**, *403*, 62.

(81) Jiang; Bosnick, K.; Maillard, M.; Brus, L. *The Journal of Physical Chemistry B* **2003**, *107*, 9964.

(82) Fromm, D. P.; Sundaramurthy, A.; Schuck, P. J.; Kino, G.; Moerner, W. E. *Nano Letters* **2004**, *4*, 957.

(83) Tan, Y.; Fan, J.; Chen, G.; Zheng, N.; Xie, Q. *Chem Commun (Camb)* **2011**, *47*, 11624.

(84) Kim, Y.; Hong, J. W.; Lee, Y. W.; Kim, M.; Kim, D.; Yun, W. S.; Han, S. W. *Angew Chem Int Ed Engl* **2010**, *49*, 10197.

(85) Ataee-Esfahani, H.; Wang, L.; Yamauchi, Y. *Chemical Communications* **2010**, *46*, 3684.

(86) Ataee-Esfahani, H.; Wang, L.; Nemoto, Y.; Yamauchi, Y. *Chemistry of Materials* **2010**, *22*, 6310.

(87) Guo, S.; Li, J.; Dong, S.; Wang, E. *The Journal of Physical Chemistry C* **2010**, *114*, 15337.

(88) Lim, B.; Jiang, M.; Camargo, P. H.; Cho, E. C.; Tao, J.; Lu, X.; Zhu, Y.; Xia, Y. *Science* **2009**, *324*, 1302.

(89) Lim, B.; Jiang, M.; Yu, T.; Camargo, P. C.; Xia, Y. *Nano Research* **2010**, *3*, 69.

(90) Peng, Z.; Yang, H. *Journal of the American Chemical Society* **2009**, *131*, 7542.

(91) Wang, L.; Nemoto, Y.; Yamauchi, Y. *J Am Chem Soc* **2011**, *133*, 9674.

(92) Niu, Z.; Wang, D.; Yu, R.; Peng, Q.; Li, Y. *Chemical Science* **2012**, *3*, 1925.

(93) Wang, H.; Yuan, X.; Li, D.; Gu, X. *Journal of Colloid and Interface Science* **2012**, *384*, 105.

(94) Zhang, J. T.; Ma, J. Z.; Wan, Y.; Jiang, J. W.; Zhao, X. S. *Materials Chemistry and Physics* **2012**, *132*, 244.

(95) Zhang, J.; Sasaki, K.; Sutter, E.; Adzic, R. R. *Science* **2007**, *315*, 220.

(96) Zhang, J.; Yang, H.; Yang, K.; Fang, J.; Zou, S.; Luo, Z.; Wang, H.; Bae, I.-T.; Jung, D. Y. *Advanced Functional Materials* **2010**, *20*, 3727.

(97) Yang, H.; Zhang, J.; Sun, K.; Zou, S.; Fang, J. *Angew Chem Int Ed Engl* **2010**, *49*, 6848.

(98) Zhang, J.; Yang, H.; Fang, J.; Zou, S. *Nano Lett* **2010**, *10*, 638.

(99) Xu, D.; Liu, Z.; Yang, H.; Liu, Q.; Zhang, J.; Fang, J.; Zou, S.; Sun, K. *Angew Chem Int Ed Engl* **2009**, *48*, 4217.

(100) Xu, D.; Bliznakov, S.; Liu, Z.; Fang, J.; Dimitrov, N. *Angew Chem Int Ed Engl* **2010**, *49*, 1282.

(101) Yin, A. X.; Min, X. Q.; Zhu, W.; Liu, W. C.; Zhang, Y. W.; Yan, C. H. *Chemistry* **2012**, *18*, 777.

(102) Kang, Y.; Murray, C. B. *Journal of the American Chemical Society* **2010**, *132*, 7568.

(103) Yuan, Q.; Zhou, Z.; Zhuang, J.; Wang, X. *Chem Commun (Camb)* **2010**, *46*, 1491.

(104) Yin, A. X.; Min, X. Q.; Zhang, Y. W.; Yan, C. H. *J Am Chem Soc* **2011**, *133*, 3816.

(105) Kang, Y.; Pyo, J. B.; Ye, X.; Gordon, T. R.; Murray, C. B. *ACS Nano* **2012**, *6*, 5642.

(106) Huang, X.; Li, Y.; Li, Y.; Zhou, H.; Duan, X.; Huang, Y. *Nano Lett* **2012**, *12*, 4265.

(107) Wu, J.; Zhang, J.; Peng, Z.; Yang, S.; Wagner, F. T.; Yang, H. *Journal of the American Chemical Society* **2010**, *132*, 4984.

(108) Wu, J.; Yang, H. *Nano Research* **2010**, *4*, 72.

(109) Cui, C.; Gan, L.; Li, H.-H.; Yu, S.-H.; Heggen, M.; Strasser, P. *Nano Letters* **2012**, *12*, 5885.

(110) Lee, Y. W.; Ko, A. R.; Han, S. B.; Kim, H. S.; Park, K. W. *Physical chemistry chemical physics : PCCP* **2011**, *13*, 5569.

(111) Lee, Y.-W.; Ko, A. R.; Kim, D.-Y.; Han, S.-B.; Park, K.-W. *RSC Advances* **2012**, *2*, 1119.

(112) Liu, X.; Wang, W.; Li, H.; Li, L.; Zhou, G.; Yu, R.; Wang, D.; Li, Y. *Sci Rep* **2013**, *3*, 1404.

(113) Guo, S.; Dong, S.; Wang, E. *Chem Commun (Camb)* **2010**, *46*, 1869.

(114) Hong, J. W.; Kang, S. W.; Choi, B.-S.; Kim, D.; Lee, S. B.; Han, S. W. *ACS Nano* **2012**, *6*, 2410.

(115) Zhang, W.; Yang, J.; Lu, X. *ACS Nano* **2012**, *6*, 7397.

(116) Zhang, L.; Zhang, J.; Jiang, Z.; Xie, S.; Jin, M.; Han, X.; Kuang, Q.; Xie, Z.; Zheng, L. *Journal of Materials Chemistry* **2011**, *21*, 9620.

(117) Zhang, H.; Jin, M.; Liu, H.; Wang, J.; Kim, M. J.; Yang, D.; Xie, Z.; Liu, J.; Xia, Y. *ACS Nano* **2011**, *5*, 8212.

(118) Han, J.; Zhou, Z.; Yin, Y.; Luo, X.; Li, J.; Zhang, H.; Yang, B. *CrystEngComm* **2012**, *14*, 7036.

(119) Dutta, I.; Carpenter, M. K.; Balogh, M. P.; Ziegelbauer, J. M.; Moylan, T. E.; Atwan, M. H.; Irish, N. P. *The Journal of Physical Chemistry C* **2010**, *114*, 16309.

(120) Mohl, M.; Dobo, D.; Kukovecz, A.; Konya, Z.; Kordas, K.; Wei, J.; Vajtai, R.; Ajayan, P. M. *The Journal of Physical Chemistry C* **2011**, *115*, 9403.

(121) Yang, S.; Hong, F.; Wang, L.; Guo, S.; Song, X.; Ding, B.; Yang, Z. *The Journal of Physical Chemistry C* **2009**, *114*, 203.

(122) Liu, Q.; Yan, Z.; Henderson, N. L.; Bauer, J. C.; Goodman, D. W.; Batteas, J. D.; Schaak, R. E. *Journal of the American Chemical Society* **2009**, *131*, 5720.

(123) Peng, Z.; You, H.; Yang, H. *ACS Nano* **2010**, *4*, 1501.

(124) Zhu, C.; Guo, S.; Dong, S. *Adv Mater* **2012**, *24*, 2326.

(125) Sun, Y.; Xia, Y. *Advanced Materials* **2003**, *15*, 695.

(126) Chen, J.; McLellan, J. M.; Siekkinen, A.; Xiong, Y.; Li, Z.-Y.; Xia, Y. *Journal of the American Chemical Society* **2006**, *128*, 14776.

(127) Sun, Y.; Xia, Y. *Advanced Materials* **2004**, *16*, 264.

(128) Seo, D.; Yoo, C. I.; Jung, J.; Song, H. *Journal of the American Chemical Society* **2008**, *130*, 2940.

(129) Gonzalez, E.; Arbiol, J.; Puntes, V. F. *Science* **2011**, *334*, 1377.

(130) Sun, Y.; Xia, Y. *Journal of the American Chemical Society* **2004**, *126*, 3892.

(131) Choi, Y.; Hong, S.; Liu, L.; Kim, S. K.; Park, S. *Langmuir* **2012**, *28*, 6670.

(132) Hong, X.; Wang, D.; Cai, S.; Rong, H.; Li, Y. *Journal of the American Chemical Society* **2012**, *134*, 18165.

(133) Okuno, Y.; Nishioka, K.; Kiya, A.; Nakashima, N.; Ishibashi, A.; Niidome, Y. *Nanoscale* **2010**, *2*, 1489.

(134) Li, Q.; Jiang, R.; Ming, T.; Fang, C.; Wang, J. *Nanoscale* **2012**, *4*, 7070.

(135) Park, K.; Drummy, L. F.; Vaia, R. A. *Journal of Materials Chemistry* **2011**, *21*, 15608.

(136) Yang, Y.; Wang, W.; Li, X.; Chen, W.; Fan, N.; Zou, C.; Chen, X.; Xu, X.; Zhang, L.; Huang, S. *Chemistry of Materials* **2013**, *25*, 34.

(137) Li, C.; Sun, L.; Sun, Y.; Teranishi, T. *Chemistry of Materials* **2013**.

(138) Park, G.; Seo, D.; Jung, J.; Ryu, S.; Song, H. *The Journal of Physical Chemistry C* **2011**, *115*, 9417.

(139) Ma, Y.; Li, W.; Cho, E. C.; Li, Z.; Yu, T.; Zeng, J.; Xie, Z.; Xia, Y. *ACS Nano* **2010**, *4*, 6725.

(140) Gong, J.; Zhou, F.; Li, Z.; Tang, Z. *Langmuir* **2012**, *28*, 8959.

(141) Xue, C.; Millstone, J. E.; Li, S.; Mirkin, C. A. *Angewandte Chemie International Edition* **2007**, *46*, 8436.

(142) Yoo, H.; Millstone, J. E.; Li, S.; Jang, J.-W.; Wei, W.; Wu, J.; Schatz, G. C.; Mirkin, C. A. *Nano Letters* **2009**, *9*, 3038.

(143) Hong, S.; Choi, Y.; Park, S. *Chemistry of Materials* **2011**, *23*, 5375.

(144) Tsuji, M.; Matsuo, R.; Jiang, P.; Miyamae, N.; Ueyama, D.; Nishio, M.; Hikino, S.; Kumagae, H.; Kamarudin, K. S. N.; Tang, X.-L. *Crystal Growth & Design* **2008**, *8*, 2528.

(145) Tsuji, M.; Ogino, M.; Matsunaga, M.; Miyamae, N.; Matsuo, R.; Nishio, M.; Alam, M. J. *Crystal Growth & Design* **2010**, *10*, 4085.

(146) Gu, H.; Yang, Z.; Gao, J.; Chang, C. K.; Xu, B. *Journal of the American Chemical Society* **2004**, *127*, 34.

(147) Feng, Y.; He, J.; Wang, H.; Tay, Y. Y.; Sun, H.; Zhu, L.; Chen, H. *Journal of the American Chemical Society* **2012**, *134*, 2004.

(148) Tran, T. T.; Lu, X. *The Journal of Physical Chemistry C* **2011**, *115*, 3638.

(149) Sun, Y. G.; Xia, Y. N. *Science* **2002**, *298*, 2176.

(150) Skrabalak, S. E.; Au, L.; Lu, X.; Li, X.; Xia, Y. *Nanomedicine* **2007**, *2*, 657.

(151) Skrabalak, S. E.; Chen, J.; Sun, Y.; Lu, X.; Au, L.; Cobley, C. M.; Xia, Y. *Accounts of Chemical Research* **2008**, *41*, 1587.

(152) Cobley, C. M.; Xia, Y. *Materials Science & Engineering R-Reports* **2010**, *70*, 44.

(153) Sun, Y. G.; Xia, Y. N. *Journal of the American Chemical Society* **2004**, *126*, 3892.

(154) Seo, D.; Song, H. *Journal of the American Chemical Society* **2009**, *131*, 18210.

(155) Xu, C.; Li, Y.; Tian, F.; Ding, Y. *Chemphyschem* **2010**, *11*, 3320.

(156) Lu, X.; Tuan, H.-Y.; Chen, J.; Li, Z.-Y.; Korgel, B. A.; Xia, Y. *Journal of the American Chemical Society* **2007**, *129*, 1733.

(157) Tan, Y.-N.; Yang, J.; Lee, J. Y.; Wang, D. I. C. *Journal of Physical Chemistry C* **2007**, *111*, 14084.

(158) Huang, X.; Zhang, H.; Guo, C.; Zhou, Z.; Zheng, N. *Angewandte Chemie-International Edition* **2009**, *48*, 4808.

(159) Skrabalak, S. E.; Au, L.; Li, X.; Xia, Y. *Nature Protocols* **2007**, *2*, 2182.

(160) Sun, Y. G.; Mayers, B.; Xia, Y. N. *Advanced Materials* **2003**, *15*, 641.

(161) Sun, Y. G.; Wiley, B.; Li, Z. Y.; Xia, Y. N. *Journal of the American Chemical Society* **2004**, *126*, 9399.

(162) Lu, X.; Au, L.; McLellan, J.; Li, Z.-Y.; Marquez, M.; Xia, Y. *Nano Letters* **2007**, *7*, 1764.

(163) Huang, J.; Vongehr, S.; Tang, S.; Meng, X. *Journal of Physical Chemistry C* **2010**, *114*, 15005.

(164) Chen, X.; Cui, C.-H.; Guo, Z.; Liu, J.-H.; Huang, X.-J.; Yu, S.-H. *Small* **2011**, *7*, 858.

(165) Yin, Y.; Erdonmez, C.; Aloni, S.; Alivisatos, A. P. *Journal of the American Chemical Society* **2006**, *128*, 12671.

(166) Chen, J. Y.; Wiley, B.; McLellan, J.; Xiong, Y. J.; Li, Z. Y.; Xia, Y. N. *Nano Letters* **2005**, *5*, 2058.

(167) Lu, X.; McKiernan, M.; Peng, Z.; Lee, E. P.; Yang, H.; Xia, Y. *Science of Advanced Materials* **2010**, *2*, 413.

(168) Yin, A.-X.; Min, X.-Q.; Zhu, W.; Liu, W.-C.; Zhang, Y.-W.; Yan, C.-H. *Chemistry – A European Journal* **2012**, *18*, 777.

(169) Zhang, G.; Sun, S.; Li, R.; Sun, X. *Chemistry – A European Journal* **2010**, *16*, 10630.

(170) Niu, K.-Y.; Kulinich, S. A.; Yang, J.; Zhu, A. L.; Du, X.-W. *Chemistry-a European Journal* **2012**, *18*, 4234.

(171) Chen, J.; Saeki, F.; Wiley, B. J.; Cang, H.; Cobb, M. J.; Li, Z. Y.; Au, L.; Zhang, H.; Kimmey, M. B.; Li, X. D.; Xia, Y. N. *Nano Letters* **2005**, *5*, 473.

(172) Chen, J.; Wang, D.; Xi, J.; Au, L.; Siekkinen, A.; Warsen, A.; Li, Z.-Y.; Zhang, H.; Xia, Y.; Li, X. *Nano Letters* **2007**, *7*, 1318.

(173) Yavuz, M. S.; Cheng, Y.; Chen, J.; Cobley, C. M.; Zhang, Q.; Rycenga, M.; Xie, J.; Kim, C.; Song, K. H.; Schwartz, A. G.; Wang, L. V.; Xia, Y. *Nature materials* **2009**, *8*, 935.

(174) Olson, T. Y.; Schwartzberg, A. M.; Orme, C. A.; Talley, C. E.; O'Connell, B.; Zhang, J. Z. *The Journal of Physical Chemistry C* **2008**, *112*, 6319.

(175) Rycenga, M.; Hou, K. K.; Cobley, C. M.; Schwartz, A. G.; Camargo, P. H. C.; Xia, Y. *Physical Chemistry Chemical Physics* **2009**, *11*, 5903.

(176) Alia, S. M.; Zhang, G.; Kisailus, D.; Li, D.; Gu, S.; Jensen, K.; Yan, Y. *Advanced Functional Materials* **2010**, *20*, 3742.

(177) Feng, Y.-Y.; Zhang, G.-R.; Ma, J.-H.; Liu, G.; Xu, B.-Q. *Physical Chemistry Chemical Physics* **2011**, *13*, 3863.

(178) Ye, F.; Liu, H.; Hu, W.; Zhong, J.; Chen, Y.; Cao, H.; Yang, J. *Dalton transactions* **2012**, *41*, 2898.

(179) Ridelman, Y.; Singh, G.; Popovitz-Biro, R.; Wolf, S. G.; Das, S.; Klajn, R. *Small* **2012**, *8*, 654.

(180) Lee, C.-L.; Tseng, C.-M. *Journal of Physical Chemistry C* **2008**, *112*, 13342.

(181) He, W.; Wu, X.; Liu, J.; Zhang, K.; Chu, W.; Feng, L.; Hu, X.; Zhou, W.; Xie, S. *Langmuir* **2010**, *26*, 4443.

(182) Xu, C.; Liu, Y.; Su, F.; Liu, A.; Qiu, H. *Biosensors & Bioelectronics* **2011**, *27*, 160.

(183) Mahmoud, M. A.; El-Sayed, M. A. *Langmuir* **2012**, *28*, 4051.

(184) Zelyanskii, A. V.; Zhukova, L. V.; Kitaev, G. A. *Inorganic Materials* **2001**, *37*, 523.

(185) Bi, Y.; Ye, J. *Chemical Communications* **2010**, *46*, 1532.

(186) Chen, M.; Wu, B.; Yang, J.; Zheng, N. *Advanced Materials* **2012**, *24*, 862.

(187) Zhang, J.; Sasaki, K.; Sutter, E.; Adzic, R. R. *Science* **2007**, *315*, 220.

(188) Sugimoto, T.; Miyake, K. *Journal of Colloid and Interface Science* **1990**, *140*, 335.

(189) Hsu, S.-W.; On, K.; Gao, B.; Tao, A. R. *Langmuir* **2011**, *27*, 8494.

(190) Zhang, L.; Li, N.; Gao, F.; Hou, L.; Xu, Z. *Journal of the American Chemical Society* **2012**, *134*, 11326.

(191) Fleischmann, M.; Hendra, P. J.; McQuillan, A. J. *Chemical Physics Letters* **1974**, *26*, 163.

(192) Campion, A.; Kambhampati, P. *Chemical Society Reviews* **1998**, *27*, 241.

(193) Zhao; Jensen, L.; Schatz, G. C. *Journal of the American Chemical Society* **2006**, *128*, 2911.

(194) Zhao, L. L.; Jensen, L.; Schatz, G. C. *Nano Letters* **2006**, *6*, 1229.

(195) Sharma, B.; Frontiera, R. R.; Henry, A.-I.; Ringe, E.; Van Duyne, R. P. *Materials Today* **2012**, *15*, 16.

(196) Liu, S.; Zhao, X.; Li, Y.; Chen, M. *Journal of Chemical Physics* **2009**, *130*.

(197) Sun, M.; Xu, H. *ChemPhysChem* **2009**, *10*, 392.

(198) Zhao, L. B.; Huang, R.; Huang, Y. F.; Wu, D. Y.; Ren, B.; Tian, Z. Q. *Journal of Chemical Physics* **2011**, *135*.

(199) Lim, D. K.; Jeon, K. S.; Hwang, J. H.; Kim, H.; Kwon, S.; Suh, Y. D.; Nam, J. M. *Nature Nanotechnology* **2011**, *6*, 452.

(200) Grillet, N.; Manchon, D.; Bertorelle, F.; Bonnet, C.; Broyer, M.; Cottancin, E.; Lermé, J.; Hillenkamp, M.; Pellarin, M. *ACS Nano* **2011**, *5*, 9450.

(201) Marinica, D. C.; Kazansky, A. K.; Nordlander, P.; Aizpurua, J.; Borisov, A. G. *Nano Letters* **2012**, *12*, 1333.

(202) Osberg, K. D.; Rycenga, M.; Harris, N.; Schmucker, A. L.; Langille, M. R.; Schatz, G. C.; Mirkin, C. A. *Nano Letters* **2012**, *12*, 3828.

(203) Gandra, N.; Abbas, A.; Tian, L.; Singamaneni, S. *Nano Letters* **2012**, *12*, 2645.

(204) McMahon, J. M.; Li, S.; Ausman, L. K.; Schatz, G. C. *The Journal of Physical Chemistry C* **2012**, *116*, 1627.

(205) McMahon, J. M.; Gray, S. K.; Schatz, G. C. *Physical Review B* **2011**, *83*.

(206) Zhou, Q.; Li, X.; Fan, Q.; Zhang, X.; Zheng, J. *Angewandte Chemie International Edition* **2006**, *45*, 3970.

(207) Kim, K.; Lee, H. B.; Choi, J. Y.; Shin, K. S. *Journal of Physical Chemistry C* **2011**, *115*, 21047.

(208) Hu, X.; Wang, T.; Wang, L.; Dong, S. *The Journal of Physical Chemistry C* **2007**, *111*, 6962.

(209) Kim, K.; Lee, H. B.; Yoon, J. K.; Shin, D.; Shin, K. S. *The Journal of Physical Chemistry C* **2010**, *114*, 13589.

(210) Im, H.; Bantz, K. C.; Lindquist, N. C.; Haynes, C. L.; Oh, S.-H. *Nano Letters* **2010**, *10*, 2231.

(211) Fang, Y. *Science* **2008**, *322*, 1790.

(212) Sun, L.; Johnson, B.; Wade, T.; Crooks, R. M. *The Journal of Physical Chemistry* **1990**, *94*, 8869.

(213) Uetsuki, K.; Verma, P.; Yano, T.-a.; Saito, Y.; Ichimura, T.; Kawata, S. *The Journal of Physical Chemistry C* **2010**, *114*, 7515.

(214) Zhu, T.; Fu, X.; Mu, T.; Wang, J.; Liu, Z. *Langmuir* **1999**, *15*, 5197.

(215) Kim, Y. T.; McCarley, R. L.; Bard, A. J. *The Journal of Physical Chemistry* **1992**, *96*, 7416.

(216) Gole, A.; Sainkar, S. R.; Sastry, M. *Chemistry of Materials* **2000**, *12*, 1234.

(217) Feng, Y.; Wang, Y.; Wang, H.; Chen, T.; Tay, Y. Y.; Yao, L.; Yan, Q.; Li, S.; Chen, H. *Small* **2012**, *8*, 246.

(218) Xu, H. *Physical Review B* **2005**, *72*, 073405.

(219) Zhou, Q.; Fan, Q.; Zhuang, Y.; Li, Y.; Zhao, G.; Zheng, J. *The Journal of Physical Chemistry B* **2006**, *110*, 12029.

(220) Habas, S. E.; Lee, H.; Radmilovic, V.; Somorjai, G. A.; Yang, P. *Nature materials* **2007**, *6*, 692.

(221) Lu, C.-L.; Prasad, K. S.; Wu, H.-L.; Ho, J.-a. A.; Huang, M. H. *Journal of the American Chemical Society* **2010**, *132*, 14546.

(222) Zhang, L.; Niu, W.; Li, Z.; Xu, G. *Chemical Communications* **2011**, *47*, 10353.

(223) Annan, W.; Qing, P.; Yadong, L. *Chemistry of Materials* **2011**, *23*, 3217.

(224) Li, J.; Zheng, Y.; Zeng, J.; Xia, Y. *Chemistry* **2012**, *18*, 8150.

(225) Yu, Y.; Zhang, Q.; Xie, J.; Lee, J. Y. *Nature communications* **2013**, *4*, 1454.

(226) Shankar, S. S.; Rai, A.; Ahmad, A.; Sastry, M. *Journal of Colloid and Interface Science* **2004**, *275*, 496.

(227) Rodriguez-Gonzalez, B.; Burrows, A.; Watanabe, M.; Kiely, C. J.; Liz Marzan, L. M. *Journal of Materials Chemistry* **2005**, *15*, 1755.

(228) Zhang, X.; Tsuji, M.; Lim, S.; Miyamae, N.; Nishio, M.; Hikino, S.; Umezu, M. *Langmuir* **2007**, *23*, 6372.

(229) Bruzzone, S.; Arrighini, G. P.; Guidotti, C. *Materials Science and Engineering: C* **2003**, *23*, 965.

(230) Zhu, J. *Physica E: Low-dimensional Systems and Nanostructures* **2005**, *27*, 296.

(231) Yang, Y.; Shi, J.; Kawamura, G.; Nogami, M. *Scripta Materialia* **2008**, *58*, 862.

(232) Maier, S. A.; Brongersma, M. L.; Kik, P. G.; Meltzer, S.; Requicha, A. A. G.; Atwater, H. A. *Advanced Materials* **2001**, *13*, 1501.

(233) Park, K.; Vaia, R. A. *Advanced Materials* **2008**, *20*, 3882.

(234) Wu, H.-L.; Chen, C.-H.; Huang, M. H. *Chemistry of Materials* **2008**, *21*, 110.

(235) Xiang, Y.; Wu, X.; Liu, D.; Li, Z.; Chu, W.; Feng, L.; Zhang, K.; Zhou, W.; Xie, S. *Langmuir* **2008**, *24*, 3465.

(236) Nikoobakht, B.; El-Sayed, M. A. *Langmuir* **2001**, *17*, 6368.

(237) Lofton, C.; Sigmund, W. *Advanced Functional Materials* **2005**, *15*, 1197.

(238) Hubert, F.; Testard, F.; Spalla, O. *Langmuir* **2008**, *24*, 9219.

(239) Pérez-Juste, J.; Pastoriza-Santos, I.; Liz-Marzán, L. M.; Mulvaney, P. *Coordination Chemistry Reviews* **2005**, *249*, 1870.

(240) Sun, Y.; Gates, B.; Mayers, B.; Xia, Y. *Nano Letters* **2002**, *2*, 165.

(241) Burgin, J.; Florea, I.; Majimel, J.; Dobri, A.; Ersen, O.; Treguer-Delapierre, M. *Nanoscale* **2012**, *4*, 1299.

(242) Wiley, B. J.; Chen, Y.; McLellan, J. M.; Xiong, Y.; Li, Z.-Y.; Ginger, D.; Xia, Y. *Nano Letters* **2007**, *7*, 1032.

(243) Svendsen, G. K.; Weman, H.; Skaar, J. *Journal of Applied Physics* **2011**, *109*.

(244) Zheng, Y.; Tao, J.; Liu, H.; Zeng, J.; Yu, T.; Ma, Y.; Moran, C.; Wu, L.; Zhu, Y.; Liu, J.; Xia, Y. *Small* **2011**.

(245) Niu, W.; Xu, G. *Nano Today* **2011**, *6*, 265.

(246) Quan, Z.; Wang, Y.; Fang, J. *Accounts of Chemical Research* **2012**, *46*, 191.

(247) Liu; Guyot-Sionnest, P. *The Journal of Physical Chemistry B* **2005**, *109*, 22192.

(248) Kou, X.; Zhang, S.; Tsung, C.-K.; Yeung, M. H.; Shi, Q.; Stucky, G. D.; Sun, L.; Wang, J.; Yan, C. *The Journal of Physical Chemistry B* **2006**, *110*, 16377.

(249) Kou, X.; Ni, W.; Tsung, C.-K.; Chan, K.; Lin, H.-Q.; Stucky, G. D.; Wang, J. *Small* **2007**, *3*, 2103.

(250) Zhang, S.-H.; Jiang, Z.-Y.; Xie, Z.-X.; Xu, X.; Huang, R.-B.; Zheng, L.-S. *The Journal of Physical Chemistry B* **2005**, *109*, 9416.

(251) Wang, Z. L. *The Journal of Physical Chemistry B* **2000**, *104*, 1153.

(252) Saidi, W. A.; Feng, H.; Fichthorn, K. A. *The Journal of Physical Chemistry C* **2013**, *117*, 1163.

(253) Ni, C.; Hassan, P. A.; Kaler, E. W. *Langmuir* **2005**, *21*, 3334.

(254) Migani, A.; Illas, F. *The Journal of Physical Chemistry B* **2006**, *110*, 11894.

(255) Ha, T. H.; Koo, H.-J.; Chung, B. H. *The Journal of Physical Chemistry C* **2006**, *111*, 1123.

(256) Duan, J.; Park, K.; MacCuspie, R. I.; Vaia, R. A.; Pachter, R. *The Journal of Physical Chemistry C* **2009**, *113*, 15524.

(257) Sun, Y.; Xia, Y. *J. Am. Chem. Soc.* **2004**, *126*, 3892.

Appendix

List of Publications

Weiqing Zhang, Goh Hao Ying Johnny, Xianmao Lu, "Growth of Au@Ag Core-shell Penta-twinned Nanorods: Tuning the End Facets", **Chem. Eur. J., 2013**, 19, 12732–12738.

Weiqing Zhang, Xianmao Lu, "Morphology Control of Bimetallic Nanostructures for Electrochemical Catalysts", **Nanotechnology Reviews,** accepted.

Weiqing Zhang, Jizheng Yang, Xianmao Lu, "Tailoring Galvanic Replacement Reaction for the Preparation of Pt/Ag Bimetallic Hollow Nanostructures with Controlled Number of Voids", **ACS Nano, 2012**, 6, 7397–7405.

Wenxin Niu, **Weiqing Zhang,** Shaik Firdoz, Xianmao Lu, "Dodecahedral Gold Nanocrystals: The Missing Platonic Shape" J. Am. Chem. Soc., 2014, 136, 3010-3012.

Wenxin Niu, **Weiqing Zhang,** Shaik Firdoz, Xianmao Lu, "Controlled Synthesis of Palladium Concave Nanocubes with Sub-10-nm Edges and Corners for Tunable Plasmonic Property" Chemistry of Materials, 2014, 26, 2180–2186

Mustafa Eginligil, **Weiqing Zhang**, Alan Kalitsov, Xianmao Lu, Hyunsoo Yang, "Tunneling behavior of bismuth telluride nanoplates in electrical transport", **Chemical Physics Letters, 2012**, 546, 125-128.

Zhipeng Sun, **Weiqing Zhang**, Xianmao Lu, "Reduced graphene oxide nanosheets functionalized with bile salts as support for electrochemical catalysts", **Adv. Mater. Res., 2012**, 535-537, 1467-1477.

Yong Wang, Qingxiao Wang, Hang Sun, **Weiqing Zhang**, Gang Chen, Yawen Wang, Xiaoshuang Shen, Yu Han, Xianmao Lu, Hongyu Chen, "Chiral transformation: from single nanowire to double helix", **J. Am. Chem. Soc., 2011**, 133, 20060-20063.

J Y Sun, Z. K. Wang, H. S. Lim, V. L. Zhang, S. C. Ng, M. H. Kuok, **W. Zhang,** S. Firdoz, X. M. Lu, "Brillouin study of confined eigenvibrations of silver nanocubes", **Solid State Commun., 2012,** 152, 501-503.